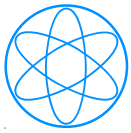

Technische Universität München

Discovery of the shape coexisting 0^+ state in ^{32}Mg

Dissertation
von

Kathrin Wimmer

Lehrstuhl E12 für
Experimentalphysik

Technische Universität München
Physik-Department E12

Discovery of the shape coexisting 0^+ state in ^{32}Mg

Kathrin Wimmer

Vollständiger Abdruck der von der Fakultät für Physik der Technischen Universität München zur Erlangung des akademischen Grades eines

Doktors der Naturwissenschaften (Dr. rer. nat.)

genehmigten Dissertation.

Vorsitzender:	Univ.-Prof. Dr. H. Friedrich
Prüfer der Dissertation:	
	1. Univ.-Prof. Dr. R. Krücken
	2. Univ.-Prof. Dr. St. Paul

Die Dissertation wurde am 22.07.2010 bei der Technischen Universität München eingereicht und durch die Fakultät für Physik am 16.08.2010 angenommen.

Summary

The evolution of shell structure in exotic nuclei as a function of proton (Z) and neutron (N) number is currently at the center of many theoretical and experimental investigations. It has been realized that the interaction of the last valence protons and neutrons, in particular the monopole component of the residual interaction between those nucleons, can lead to significant shifts in the single-particle energies, leading to the collapse of classic shell closures and the appearance of new shell gaps. The "Island of Inversion" around ^{32}Mg, which is one of the most studied phenomena in the nuclear chart, is a well known example for such changes in nuclear structure. In this region of neutron-rich nuclei around the magic number $N = 20$ strongly deformed ground states in Ne, Na, and Mg isotopes have been observed. Due to the reduction of the $N = 20$ shell gap quadrupole correlations can enable low-lying deformed $2p - 2h$ intruder states from the fp-shell to compete with spherical normal neutron $0p - 0h$ states of the sd-shell. In this situation the promotion of a neutron pair across the $N = 20$ gap can result in deformed intruder ground states. Consequentially the two competing configurations can lead to the coexistence of spherical and deformed 0^+ states in the neutron rich nuclei ^{30,32}Mg.

In this work the shape coexistence in ^{32}Mg was studied by a two neutron transfer reaction at the REX-ISOLDE facility (CERN). The two neutron transfer reaction with a ^{30}Mg beam involved for the first time the use of a radioactive tritium target in combination with a radioactive heavy ion beam. Light charged particles emitted from the target were detected and identified by the T-REX particle detector while γ-rays were detected by the MINIBALL Germanium detector array. The shape of the angular distribution of the protons allows to unambiguously determine the angular momentum transfer ΔL of the reaction and thus to identify the 0^+ states. The analysis of excitation energies and angular distributions led to the first observation of the excited shape coexisting 0^+ state in ^{32}Mg. From the cross section the spectroscopic amplitudes can be deduced and compared with shell model calculations. This allows to draw conclusions on the configuration of the populated state.

Zusammenfassung

Die Veränderung der Schalenstruktur exotischer Atomkerne mit der Protonen- (Z) oder Neutronenzahl (N) ist ein aktuelles Gebiet zahlreicher theoretischer und experimenteller Studien. Die Wechselwirkung der letzten Valenznukleonen, insbesondere die Monopolkomponente der Restwechselwirkung, kann die Einteilchenenergien verschieben. Das kann dazu führen, dass die bekannten magischen Schalenabschlüsse für exotische Kerne nicht mehr gelten, sondern vielmehr neue magische Zahlen auftreten. Ein seit langem bekanntes Beispiel für diese Veränderung der Schalenstruktur ist die Insel der Inversion ("Island of Inversion") um ^{32}Mg. Dort wurden in den neutronenreichen Isotopen in Ne, Na und Mg stark deformierte Grundzustände entdeckt, was im Widerspruch zur Erwartung von sphärischen Zuständen für die magische Neutronenzahl $N = 20$ ist. Durch die energetische Reduktion des $N = 20$ Schalenabschlusses können durch Quadrupolkorrelationen deformierte Neutronen Zweiteilchen-Zweiloch ($2p-2h$) Konfigurationen in der fp Schale abgesenkt werden und so ähnliche Energien erreichen wie die sphärischen $0p-0h$ Zustände der sd Schale. Wird ein Neutronenpaar über die $N = 20$ Energielücke angehoben, kann dies zu deformierten Grundzuständen führen. Dies resultiert in energetisch nah beieinanderliegenden sphärischen und deformierten 0^+ Zuständen, zur sogenannten Formkoexistenz, in den neutronenreichen Isotopen ^{30,32}Mg.

Das Thema dieser Arbeit ist die Untersuchung der Formkoexistenz in ^{32}Mg durch eine zwei Neutronen Transferreaktion an der Beschleunigeranlage REX-ISOLDE (CERN). Für diese Reaktion mit einem ^{30}Mg Strahl wurde erstmals ein radioaktives Tritiumtarget in Verbindung mit dem radioaktiven Schwerionenstrahl eingesetzt. Zur Detektion und Identifikation von leichten geladenen Teilchen wurde der T-REX Silizium Detektoraufbau verwendet. Die γ Strahlung wurde mit dem MINIBALL Germanium Detektor gemessen. Aus der Form der Winkelverteilung der Protonen lässt sich der Drehimpulsübertrag der Reaktion ΔL bestimmen und so können 0^+ Zustände identifiziert werden. Durch die Bestimmung der Anregungsenergie sowie der Winkelverteilung konnte der angeregte sphärische 0^+ Zustand in ^{32}Mg erstmals beobachtet werden. Aus dem Wirkungsquerschnitt für den bevölkerten Zustand können spektroskopische Amplituden bestimmt und mit Schalenmodellrechnungen verglichen werden. Daraus kann man Rückschlüsse auf die Konfiguration des Zustandes ziehen.

Contents

1 Introduction **1**
1.1 The "Island of Inversion" 4

2 Theoretical calculation of the transfer cross section **9**
2.1 Scattering theory 9
2.1.1 Elastic scattering for Coulomb and nuclear potentials 10
2.1.2 Multi-channel scattering 11
2.1.3 Coupled equations 11
2.2 Integral equations 12
2.2.1 Two potential formula 13
2.3 Born approximations 14
2.3.1 Distorted wave Born approximation 14
2.4 The optical model 15
2.4.1 Global optical model parameters 16
2.5 Transfer reactions 17
2.5.1 Angular distributions 18
2.5.2 Energy dependence 19
2.5.3 Q-value matching 19
2.5.4 Spectroscopic factors 21
2.6 Predictions for t(^{30}Mg,p)^{32}Mg 22
2.6.1 Sequential and simultaneous transfer of two neutrons 22
2.6.2 Expected cross section 23

3 The experimental setup at REX-ISOLDE **27**
3.1 Production of radioactive ion beams at ISOLDE 27
3.2 The post-accelerator REX 28
3.3 Beam composition 29
3.4 The setup for transfer reactions 31
3.5 The MINIBALL detector array 33
3.6 Tritium loaded Titanium target 34
3.7 Simulation of the setup and the reaction 36
3.8 Electronics and data acquisition 38

4 Data analysis **41**
4.1 Calibration procedure 41
4.1.1 Calibration of the MINIBALL array 41

4.1.2 Calibration for the particle detectors . . . 44
4.1.3 Calibration of the timing signals . . . 46
4.2 Identification and reconstruction of particles . . . 47
4.2.1 Determination of the target position . . . 49
4.2.2 Excitation energies . . . 50
4.3 Particle detection efficiency and solid angle correction . . . 51
4.3.1 Calculation of the solid angle of T-REX . . . 51
4.3.2 T-REX particle detection efficiency . . . 52

5 Experimental results and discussion 55
5.1 Results from the test measurement d(^{22}Ne,p)^{23}Ne . . . 55
5.1.1 Excitation energy . . . 56
5.1.2 Fitting optical potentials . . . 58
5.1.3 Angular distribution . . . 60
5.1.4 Discussion . . . 60
5.2 The t(^{30}Mg,p) reaction . . . 62
5.2.1 Excitation energy of the 0_2^+ state in ^{32}Mg . . . 64
5.2.2 γ decay and lifetime of the 0_2^+ state in ^{32}Mg . . . 65
5.2.3 Angular distributions . . . 67
5.3 Discussion . . . 70
5.3.1 The ground state of ^{32}Mg . . . 71
5.3.2 The excited 0^+ state in ^{32}Mg . . . 74

6 Studies for future T-REX experiments 77
6.1 T-REX for Coulomb excitation . . . 77
6.2 Measuring the E0 decay in ^{32}Mg . . . 80
6.3 The onset of deformation and shape coexistence in ^{46}Ar . . . 83

7 Summary and Outlook 89

Bibliography 91

List of Figures

1.1 Effects of the tensor force on the single particle energies 2
1.2 Effective single-particle energies around $N = 20$ 3
1.3 Nuclear chart from oxygen to sulfur. 4
1.4 Calculated potential energy surfaces for ^{30,32}Mg 5
1.5 Shape coexistence of 0^+ states in ^{30,32}Mg 6

2.1 Real and imaginary parts of the optical potential 16
2.2 Coordinate system for a transfer reaction 17
2.3 Angular distributions for different values of ΔL 19
2.4 Energy dependence of the transfer cross section 20
2.5 Angular distributions for different Q-values 20
2.6 One- and two-step contributions to the transfer cross section 23
2.7 Simultaneous and sequential transfer of two neutrons 24
2.8 Expected differential cross sections for the t(^{30}Mg,p) reaction 25

3.1 Layout of the ISOLDE hall 28
3.2 Beam identification in the Bragg chamber 30
3.3 Release curve of the ISOLDE beam 31
3.4 Experimental T-REX setup at REX-ISOLDE 32
3.5 Angular resolution of the T-REX detector array 33
3.6 Tritium loaded Titanium target 34
3.7 Fusion cross section for ^{30}Mg and ^{44}Ar beams on ^{48}Ti 35
3.8 Simulation of the t(^{30}Mg,p) reaction 37
3.9 Foil system for the suppression of elastic scattering 37
3.10 Suppression of elastic scattering on Ti with foils 38
3.11 Simulation of electron suppression 39
3.12 Electronics setup for T-REX 40
3.13 Time structure of REX-ISOLDE beams 40

4.1 Efficiency calibration of the MINIBALL γ-ray spectrometer 42
4.2 Doppler correction of the 1017 keV line in ^{23}Ne 44
4.3 Calibration procedure for barrel ΔE detectors 45
4.4 Calibration for the E detectors 46
4.5 Walk correction and time calibration 47
4.6 $\Delta E - E$ particle identification 48
4.7 Identification cuts for stopped particles 49
4.8 Determination of the target position 50

4.9 Effective solid angle covered by the T-REX setup 52
4.10 Particle detection efficiency correction 52

5.1 Level scheme of ^{23}Ne 55
5.2 γ-ray energy spectrum of the d(^{22}Ne,p) reaction 56
5.3 Energy versus ϑ_{lab} spectrum for the d(^{22}Ne,p) reaction 57
5.4 Excitation energy spectrum of ^{23}Ne 57
5.5 Fitting of optical potentials for the d(^{22}Ne,p) reaction 59
5.6 Angular distribution for the d(^{22}Ne,p)^{23}Ne reaction 61
5.7 Energy versus ϑ_{lab} spectrum for ^{30}Mg on the tritium target 63
5.8 Particle identification for the t(^{30}Mg,p) reaction 63
5.9 Excitation energy spectrum of ^{32}Mg 64
5.10 γ-rays in coincidence with transfer to the excited state 65
5.11 Estimate of the lifetime of the excited 0^+ state 66
5.12 Dependence of $\tau(0_2^+)$ on the $B(\mathrm{E2}; 0_2^+ \rightarrow 2_1^+)$ value 66
5.13 Angular distribution of elastic scattering of ^{30}Mg 68
5.14 Angular distribution for the reaction to the ground state of ^{32}Mg 69
5.15 Angular distribution for the reaction to the excited state of ^{32}Mg . . . 70
5.16 Level scheme of ^{30,32}Mg in comparison with theoretical predictions . . . 71
5.17 Neutron occupation numbers calculated in the MCSM 72
5.18 Ground state transfer cross section 73
5.19 Wave functions and single particle energies in a Wood-Saxon potential . 73
5.20 Two neutron transfer cross section for the excited state 74

6.1 Experimental setup for Coulomb excitation 77
6.2 Angular coverage for Coulomb excitation experiments 78
6.3 Dependance of the cross section with the quadrupole moment 80
6.4 Setup for a conversion electron measurement in ^{32}Mg 81
6.5 Distribution of fusion protons for ^{30}Mg on ^{48}Ti 82
6.6 Simulated electron spectrum for ^{32}Mg 82
6.7 Level scheme of ^{46}Ar 85
6.8 DWBA calculation and Simulation for the t(^{44}Ar,p) reaction 86
6.9 Angular distributions for the t(^{44}Ar,p)^{46}Ar reaction 88

List of Tables

2.1 Lippmann-Schwinger equations for the two potential formula 13
2.2 Configurations of states in ^{32}Mg 24

3.1 RILIS ionization scheme for Mg 27
3.2 Beam composition determined by different methods 30

5.1 Optical model parameter for the d(^{22}Ne,p) reaction 59
5.2 Cross section scaling factors for the d(^{22}Ne,p) reaction 60
5.3 Angle integrated cross section for the d(^{22}Ne,p) reaction 62
5.4 Results for the d(^{22}Ne,p) reaction 62
5.5 Optical model parameter for the t(^{30}Mg,p) reaction 68
5.6 Two neutron spectroscopic amplitudes for ^{32}Mg 75

6.1 Expected count rates for the t(^{44}Ar,p)^{46}Ar and t(^{44}Ar,d)^{45}Ar reactions 87

1 Introduction

The nuclear shell model is one of the major successes in the description of atomic nuclei. Nuclei with a certain number of protons or neutrons are more tightly bound than the neighboring nuclei. These numbers are called magic numbers. This observation led to the assumption of the existence of a shell structure of nucleons within the nucleus, in analogy to that of electrons within atoms. The basic concept of the nuclear shell model is that the nucleons are almost free within a central potential. This potential is created by the interaction with all other nucleons. It is usually approximated by a harmonic oscillator with an additional L^2 term or a Woods-Saxon shape. With the inclusion of a strong spin-orbit potential the experimentally observed magic numbers could be reproduced. Also other experimental observables like separation energies, excitation energies, spins, and transition probabilities can be explained for nuclei with only few particles or holes outside a magic core. For a more realistic calculation the interaction of the valence nucleons outside a magic core has to be taken into account. For such an interacting shell model the single-particle energies (SPE) of the orbits in the valence nucleon configuration space are needed as well as the interaction between two nucleons in the configuration space in terms of two-body matrix elements (TBME).

With the technical possibility to study nuclei far away from stability at large N/Z ratios, it turned out that the shell structure changes in exotic nuclei. Such changes in nuclear structure were first observed for the $N = 20$ shell, where in contrast to the expected spherical shape, strongly deformed ground states have been observed for the very neutron rich $N = 20$ isotones. This is discussed in the next section.

There are several mechanisms that may change the shell structure. The spin-orbit interaction is usually proportional to the derivative of the density $V_{LS} \propto 1/r \mathrm{d}\rho/\mathrm{d}r$. It is peaked at the nuclear surface. For neutron rich nuclei the surface is more diffuse and thus the spin-orbit interaction is reduced and the splitting of $l + 1/2$ and $l - 1/2$ orbits is smaller [DOB94]. Alternatively, a change in shell structure may be caused by the monopole component of the residual interaction. The monopole interaction shifts the single particle energies, leading to effective single particle energies (ESPE) depending on the occupation number of the involved orbitals. The effective single particle energy is the separation energy of an orbit including all effects of the monopole interaction with the other orbits in the model space. This can lead to the collapse of classic shell closures and the appearance of new shell gaps [OTS01a]. A prominent example is the collapse of the $N = 20$ shell gap in the neutron-rich oxygen isotopes where instead a new magic shell gap appears for ^{24}O at $N = 16$ [HOF08, KAN09].

Recent work by Otsuka and collaborators showed that many changes in the nuclear shell structure can be attributed to the monopole effect of the tensor force [OTS01a,

OTS05, OTS10]. The tensor force arises from the exchange of ρ and π mesons. As a component of the residual interaction it had not been explicitly considered in shell model calculations before. It can be written as

$$V_{\tau\sigma} = (\tau \cdot \tau)(\sigma \cdot \sigma) f_{\tau\sigma}(r) \tag{1.1}$$

where τ is the isospin and σ the spin operator and $f_{\tau\sigma}$ is a function of the distance of the two nucleons. The σ operator couples the spin orbit partners $j_< = l - s$ and $j_> = l + s$ much more strongly than the other combinations $j_<$ and $j_<$ or $j_>$ and $j_>$. On the other hand, the τ operator favors charge exchange processes. The process shown on the left side of Fig. 1.1 favors thus spin and isospin flip. So $V_{\tau\sigma}$ produces large

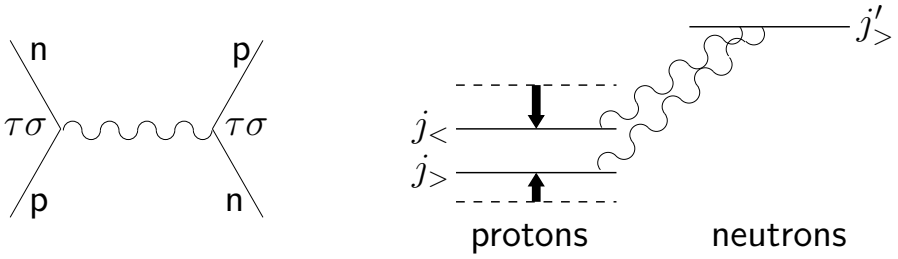

Figure 1.1: Left: Tensor force interaction between neutrons and protons. Right: Effects of the monopole component of the tensor force on the single particle energies. Adopted from [OTS05]

attractive matrix elements for neutrons in $j_<$ and protons in $j_>$ or vice versa. The interaction is repulsive if both nucleons are in $j_>$ or $j_<$ orbitals. This results in a shift in the single particle energies as shown on the right side of Fig. 1.1.

In case of stable nuclei with $N \gtrsim Z$ the proton $\pi j_>$ orbit is fully occupied when the neutron $\nu j_<$ orbit is filled, this lowers the $\nu j_<$ single particle level. For neutron rich nuclei with the same number of neutrons N, however, the $\nu j_<$ orbital can already be occupied, while the proton $\pi j_>$ orbit is not fully occupied. This changes the effect on the neutron orbit compared to the stable case. The effect on the single particle energies for the region around ^{32}Mg is shown in Fig. 1.2. In Panel a) the effective single particle energies for the $N = 20$ isotones are shown. For the stable nucleus ^{40}Ca the spin orbit partner of the last neutron orbit, the $\pi d_{5/2}$ is fully occupied, this lowers the $\nu d_{3/2}$ orbital and creates the well known $N = 20$ shell closure. As, starting from ^{34}Si ($Z = 14$), protons are removed from the $\pi d_{5/2}$ orbit, the interaction with the neutron $\nu d_{3/2}$ is reduced. This changes the slope of the ESPE. The neutron $\nu d_{3/2}$ orbital rises in energy and comes closer to the $\nu f_{7/2}$ orbital. The $N = 20$ shell gap is closed and a new one at $N = 16$ appears. For ^{28}O the $\nu d_{3/2}$ orbital is not bound anymore, this nucleus, which would be doubly magic in the classic picture and thus strongly bound, is not stable against neutron emission. On the right side of Fig. 1.2 the neutron ESPE for oxygen isotopes are shown as a function of neutron number. The nucleus ^{24}O is doubly magic due to the large gap between the $\nu s_{1/2}$ and $\nu d_{3/2}$ orbitals, while the more

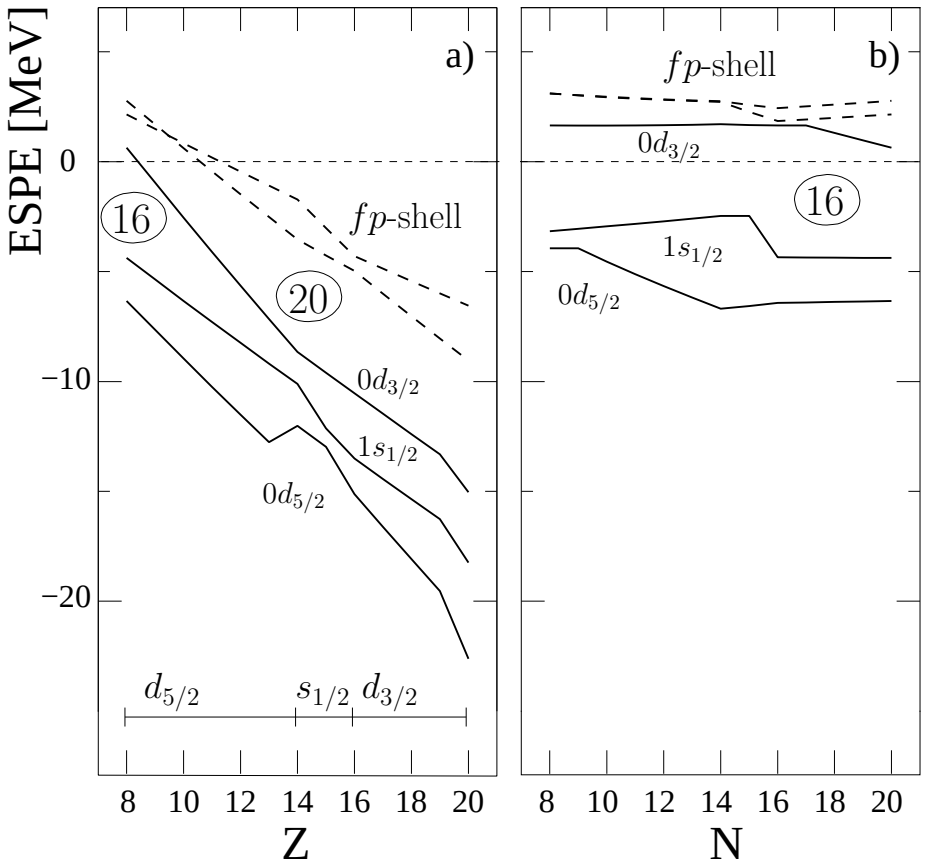

Figure 1.2: Effective single-particle energies of neutrons. a) for $N = 20$ isotones with $Z = 8$ to 20, b) for O isotopes with $N = 8$ to 20. Adopted from [OTS02].

neutron rich isotopes ^{26,28}O are unbound. If, however, one proton is added six more neutrons can be bound. The additional proton in the $\pi d_{5/2}$ orbital lowers the energy of the $\nu d_{3/2}$ and makes it bound again. For the fluorine isotopes ($Z = 9$) the heaviest isotope known is ^{31}F with $N = 22$.

For the $N = 20$ isotones ^{32}Mg and ^{30}Ne neither $N = 20$ nor $N = 16$ are good shell closures. In regions without pronounced shell closures correlations between the valence nucleons may become as large as the spacing of the single particle energies and thus may lead particle-hole excitations to higher-lying single-particle states and may enable deformed configurations to be lowered in energy. This may result in low-lying collective excitations, the coexistence of different shapes at low energies or even the deformation of the ground state.

1.1 The "Island of Inversion"

The "Island of Inversion", which is one of the most studied phenomena in the nuclear chart, is a well known example for changes in nuclear structure. It was found already 30 years ago that the $N = 20$ isotones ^{31}Na and ^{32}Mg show anomalies in their binding energies [THI75] and spectra [DÉT79, GUI84]. This was attributed to their deformation. This deformation was associated with particle-hole excitation across the $N = 20$ shell gap [WAR90]. Fig.1.3 shows the nuclear chart around the "Island of Inversion". Nuclei which belong to the "Island of Inversion" are marked in green. It should be

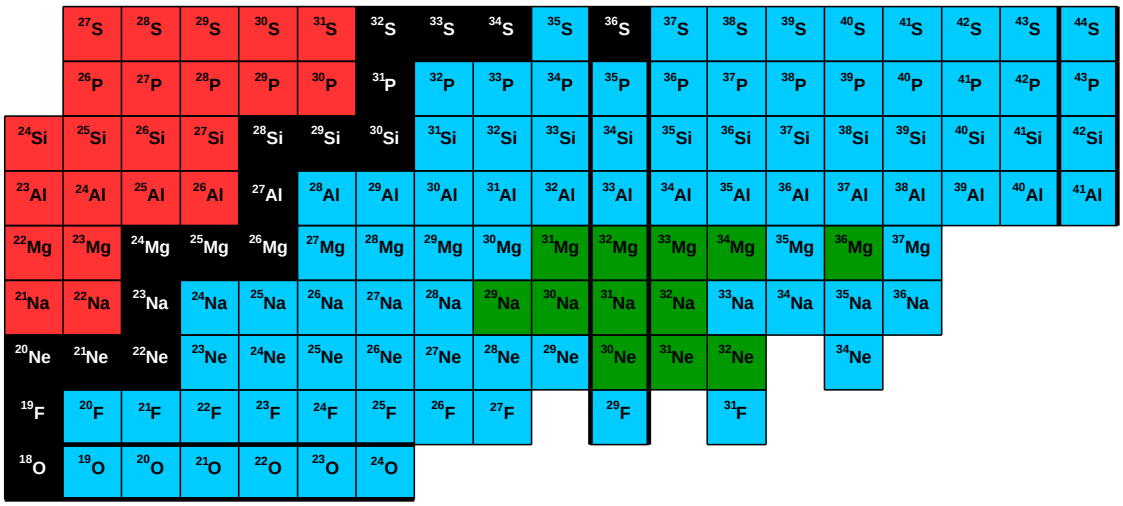

Figure 1.3: Nuclear chart from oxygen (O, $Z = 8$) to sulfur (S, $Z = 16$). Thick lines indicate the classic magic shell closures at $Z = 8$ and $N = 20, 28$. The "Island of Inversion" is marked in green.

noted that the exact border lines of the "Island of Inversion", especially on the neutron rich side, are not known. Due to the reduction of the $N = 20$ shell gap quadrupole correlations can enable low-lying deformed $2p-2h$ intruder states from the fp-shell to compete with spherical normal neutron $0p-0h$ states of the sd-shell. This effective lowering of the fp orbits compared to the normal sd-shell levels leads to an inversion of the single particle levels. In this situation the promotion of a neutron pair across the $N = 20$ gap can result in deformed intruder ground states. Consequentially the two competing configurations can lead to the coexistence of spherical and deformed 0^+ states in the neutron rich ^{30,32}Mg nuclei [HEY91].

Coulomb excitation experiments have shown that ^{30}Mg has a rather small B(E2) value for the $0^+_{\rm gs} \rightarrow 2^+_1$ transition [NIE05b, PRI99] placing this nucleus outside the "Island of Inversion". The excited deformed 0^+ state in ^{30}Mg at 1789 keV was recently identified at ISOLDE by its E0 decay to the ground state [MAC05, SCH09]. The small electric monopole strength $\rho^2(\mathrm{E0};\, 0^+_2 \rightarrow 0^+_{\rm gs}) = 26.2(75) \cdot 10^{-3}$ points to a small mixing

amplitude between the two shape coexisting 0^+ states. Calculations going beyond the mean field by incorporating configuration mixing [ROD07] using the finite range density dependent Gogny force with the D1S parametrization [BER84] have reasonably reproduced this coexistence scenario with an excitation energy of 2.11 MeV for the 0_2^+ state in ^{30}Mg and only weak mixing between the two 0^+ states. Fig. 1.4 shows the results of this calculation for ^{30,32}Mg [ROD08]. The bullets in Fig. 1.4 correspond to

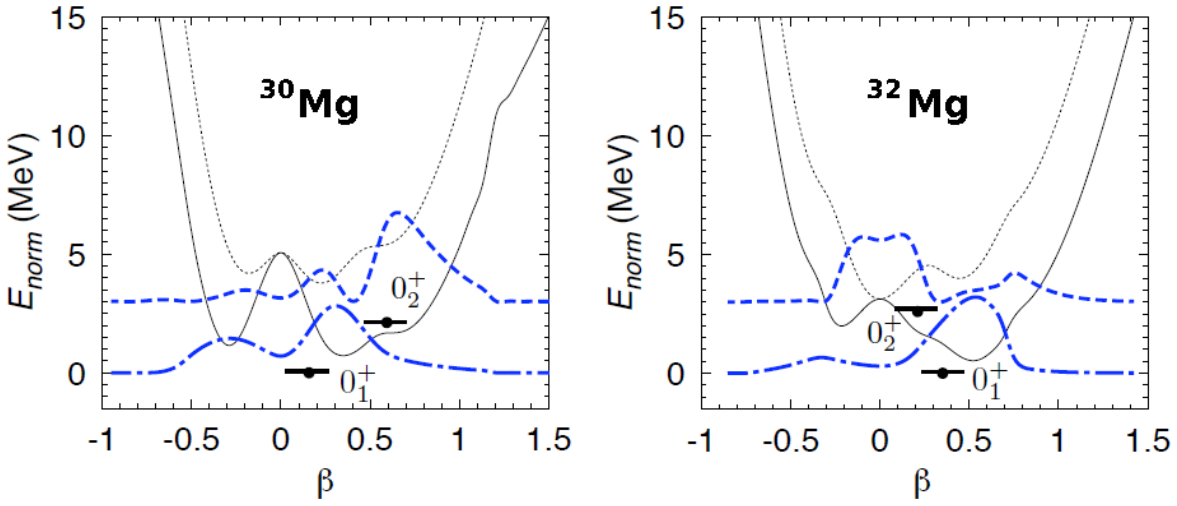

Figure 1.4: Calculated potential energy surfaces for ^{30,32}Mg [ROD08]. The dashed black lines show the results of particle number projected calculations. The solid black line represents the angular momentum projected energy surface for $J = 0$. The blue lines show the collective wave function, the probability density for finding a state with a given deformation β for the ground (dashed dotted) and the excited (dashed) 0^+ state.

the energy and intrinsic deformations of the 0_1^+ and 0_2^+ states in ^{30,32}Mg. It can be seen that in ^{30}Mg the ground state is predicted to be almost spherical, while the excited 0^+ state is strongly deformed. In ^{32}Mg the situation is reversed, with the ground state being deformed and a spherical excited state.

In ^{31}Mg a recent measurement of the ground state spin $J^\pi = 1/2^+$ [NEY05] could only be explained by a dominant intruder configuration in the ground state [MAR05], thus placing ^{31}Mg exactly on the border of the "Island of Inversion". The spins of low-lying states in ^{31}Mg have recently been determinded by the analysis of γ-ray angular distributions after a proton knockout reaction from ^{32}Al [MIL09]. For both the 51 keV and the 221 keV a spin of $J = 3/2$ has been deduced. This nucleus has also been investigated by a (d,p) one neutron transfer reaction at REX-ISOLDE. The aim of this experiment was to characterize the excited states in ^{31}Mg by measuring the angular distribution and cross section of the one neutron transfer. The results show that the state at 221 keV has a negative parity, while for the ground and 51 keV excited state $\Delta L = 0, 2$ has been observed [BIL10]. These positive parity state are dominated by intruder configurations.

^{32}Mg with the classic magic neutron number $N = 20$ has a strongly deformed ground state established by the large $B(\mathrm{E2}; 0^+_{\mathrm{gs}} \rightarrow 2^+_1)$ value [MOT95, PRI99]. However, while some spectroscopic information on excited states in ^{32}Mg is available from β-decay studies [MAC05, MAT07], no excited 0^+ state has been observed so far. Shell model calculations that correctly describe the deformed ground state in ^{32}Mg predict the spherical excited 0^+ state at 1.4 MeV [CAU01] and 3.1 MeV [OTS04]. The "beyond mean-field" calculations in Ref. [ROD02b] predict a spherical shape coexisting 0^+ state at about 1.7 MeV. The energy of this state may be sensitive to the strength of the quadrupole correlations as well as the single-particle energies and cross-shell mixing. Therefore, the observation of this shape coexisting spherical excited 0^+ state in ^{32}Mg would provide important input to refine the theoretical description of the transition into the "Island of Inversion".

The goal of the experiment described in this thesis was to find and characterize the excited shape coexisting 0^+ state in ^{32}Mg. Fig. 1.5 shows experimental level schemes for ^{30,32}Mg together with the predicted excited 0^+ state in ^{32}Mg. In a simplified picture

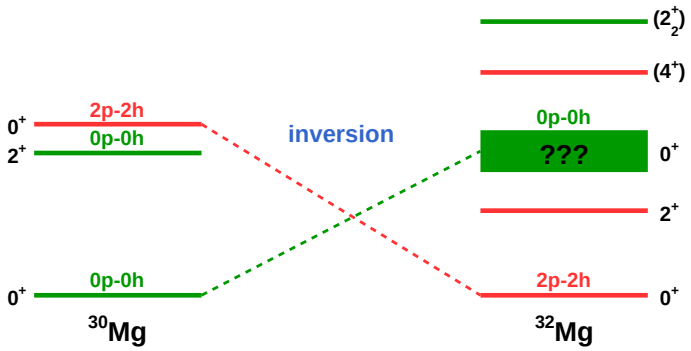

Figure 1.5: Shape coexistence of low-lying 0^+ states in ^{30,32}Mg. States which are expected to show a normal $0p - 0h$ configuration are marked in green, while those which are predicted to have an intruder $2p - 2h$ configuration are marked in red.

the ground state of ^{30}Mg is described by a normal $0p - 0h$ configuration, while the excited 0^+ state is composed of two particles outside the $N = 20$ shell gap. In ^{32}Mg the situation is inverted. The predicted configuration of the ground state is dominated by a $2p - 2h$ intruder configuration. Predictions for the excited 0^+ state suggest a spherical normal neutron $0p - 0h$ configuration for this state. In this picture the two neutrons in the transfer reaction are either added to the fp shell for the ground state or to the *sd* shell for the excited 0^+ state. Due to the similar particle-hole structure the overlap of the resulting state with the ground state of ^{30}Mg is large and the expected spectroscopic factor for the two neutron transfer reaction is large for both states. The shape of the angular distribution of the protons allows to unambiguously determine the angular momentum transfer ΔL of the reaction and thus to identify the 0^+ states. From the cross section the spectroscopic amplitudes can be deduced and compared

with shell model calculations. This allows to draw conclusions on the configuration of the populated state.

Outline of the thesis

In the next chapter the theory of transfer reactions is summarized. Besides the basic equations for the transfer amplitudes, the expected calculated cross sections and angular distributions for the t(^{30}Mg,p)^{32}Mg reaction are presented. In chapter 3 the experimental setup, in particular the T-REX charged particle detection array, is described. The data analysis steps are presented in chapter 4. The results for the d(^{22}Ne,p) reaction test measurement as well as the results for the populated states in ^{32}Mg are shown in chapter 5. Results on excitation energies and spectroscopic amplitudes are compared with shell model calculations. Chapter 6 is dedicated to possible further measurements using the T-REX setup. In the last chapter the results obtained in the framework of this thesis are summarized and an outlook to further measurements is presented.

2 Theoretical calculation of the transfer cross section

In this chapter a brief theoretical description of a few nucleon transfer reactions is presented. The formalism presented here is based on a recent book on nuclear reaction theory [THO09]. After a general introduction to scattering theory the Distorted Wave Born Approximation is introduced and its main ingredients are discussed in particular with respect to the t(^{30}Mg,p)^{32}Mg reaction.

2.1 Scattering theory

In quantum mechanics the two-body scattering is described by the Schrödinger equation for the relative motion with the center of mass energy E:

$$\left[\frac{-\hbar^2}{2\mu} + V(\vec{r}) - E\right] \psi(r, \vartheta, \varphi) = 0 \tag{2.1}$$

with the reduced mass μ. When the potential between the two interacting nuclei does not depend on the direction of the vector between them, the potential is spherical symmetric and can be written as $V(r)$. This angular independence also means that the wave functions are independent of φ, $\psi(r, \vartheta\varphi) = \psi(r, \vartheta)$, since the incoming wave function e^{ikz} is cylindrically symmetric and the potential does not break the symmetry. The center of mass coordinate system is chosen in such a way that the beam is a plane wave in z direction and the outgoing wave behaves asymptotically like a spherical wave. The asymptotic form in free space outside the range of the interaction potential $V(r)$ for the combined incident and scattered wave is

$$\psi^{\text{asymp}} = \psi^{\text{inc}} + \psi^{\text{scat}} = A\left[e^{ik_{\text{i}}z} + f(\vartheta)\frac{e^{ik_{\text{f}}r}}{r}\right], \tag{2.2}$$

with the scattering amplitude $f(\vartheta)$.

The wave function $\psi(r, \vartheta)$ is now expanded into partial waves using the Legendre polynomials $P_L(\cos\vartheta)$. Each partial wave is written as a product of a Legendre polynom and a part that depends on the radius $\chi_L(r)/r$.

$$\psi(r, \vartheta) = \frac{1}{kr}\sum_{L=0}^{\infty}(2L+1)i^L P_L(\cos\vartheta)\chi_L(r) \tag{2.3}$$

By using the orthogonality and normalization properties of the Legendre polynomials, for each value of L there is a separate partial-wave equation

$$\left[\frac{-\hbar^2}{2\mu}\left(\frac{\mathrm{d}^2}{\mathrm{d}r^2}-\frac{L(L+1)}{r^2}\right)+V(r)-E\right]\chi_L(r)=0. \tag{2.4}$$

2.1.1 Elastic scattering for Coulomb and nuclear potentials

In case of finite range potentials[1] with $V(r)=0$ for $r\geq R_\mathrm{n}$ where R_n is the range of the potential, the external scattering wave function can be written in terms of the Coulomb Hankel functions $H_L^\pm$ (for a definition see [THO09]).

$$\psi(r,\vartheta)\xrightarrow{r\geq R_\mathrm{n}}\frac{1}{kr}\sum_{L=0}^{\infty}(2L+1)i^L P_L(\cos\vartheta)A_L\left[H_L^-(0,kr)-\mathbf{S}_L H_L^+(0,kr)\right] \tag{2.5}$$

A_L and $\mathbf{S}_L$ are complex constants which are determined by matching the wave functions and their derivatives to the asymptotic form of Eq. 2.2 at the matching radius $r=a$ outside of the nuclear range R_n. By that the scattering amplitude can be expressed in terms of $\mathbf{S}_L$

$$f(\vartheta)=\frac{1}{2ik}\sum_{L=0}^{\infty}(2L+1)P_L(\cos\vartheta)(\mathbf{S}_L-1). \tag{2.6}$$

The $\mathbf{S}_L$ are called partial-wave S-matrix elements and are uniquely described by the potential. Each matrix element is equivalently described by a phase shift δ_L by $\mathbf{S}_L=e^{2i\delta_L}$ or by the partial-wave T-matrix elements $\mathbf{S}_L=1+2i\mathbf{T}_L$. For elastic scattering the phase shift is real, so $|\mathbf{S}_L|^2=1$.

The potential between two nuclei contains both a short range attractive nuclear potential as well as a long-range Coulomb repulsion. As the Coulomb potential $V_\mathrm{C}=Z_1Z_2e^2/r$ extends to infinity the results presented above are not valid. In case of a pure Coulomb potential the scattering amplitude $f_\mathrm{C}(\vartheta)$ is expressed in terms of the Coulomb phase shift $\sigma_L(\eta)$ with the Sommerfeld parameter $\eta=Z_1Z_2e^2/\hbar v$ for the relative velocity v. This lead to the point Coulomb (Rutherford) cross section

$$\left(\frac{\mathrm{d}\sigma}{\mathrm{d}\Omega}\right)_\mathrm{Ruth}=|f_\mathrm{C}(\vartheta)|^2=\frac{\eta^2}{4k^2\sin^4(\vartheta/2)}. \tag{2.7}$$

By including the nuclear potential as well as a deviation of the Coulomb potential from the $1/r$ form at short distances the scattering potential is $V(r)=V_\mathrm{C}(r)+V_\mathrm{n}(r)$ with $V_\mathrm{n}(r)$ being finite ranged and spherical. This leads to the phase shift $\delta_L=\sigma_L(\eta)+\delta_L^\mathrm{n}$ with the Coulomb distorted nuclear phase shift δ_L^n or $\mathbf{S}_L^\mathrm{n}=e^{2i\delta_L^\mathrm{n}}$. The external form of the wave function is similar to the one obtained for pure nuclear potentials (Eq. 2.5), but this time the first argument of the Hankel functions is not zero but given by the Sommerfeld parameter η.

$$\chi_L^\mathrm{ext}(r)=\frac{i}{2}\left[H_L^-(\eta,kr)-\mathbf{S}_L^\mathrm{n}H_L^+(\eta,kr)\right] \tag{2.8}$$

[1] this excludes Coulomb potentials which have a $1/r$ behavior for large r

Similar to Eq. 2.6 the scattering amplitude $f_{\rm nC} = f_{\rm C} + f_{\rm n}$ of the nuclear and Coulomb potential $V(r)$ is a combination of the point-Coulomb amplitude $f_{\rm C}$ and the Coulomb-distorted nuclear amplitude $f_{\rm n}$

$$f_{\rm n}(\vartheta) = \frac{1}{2ik}\sum_{L=0}^{\infty}(2L+1)P_L(\cos\vartheta)e^{2i\sigma_L(\eta)}(\mathbf{S}^{\rm n}_L - 1). \tag{2.9}$$

2.1.2 Multi-channel scattering

In general the scattering of two nuclei is not limited to elastic scattering only. There may be processes happening like inelastic excitations of one or both of the involved nuclei, nucleon or cluster rearrangements or capture reactions. Each of the outgoing channels defines a mass partition labeled by x. $\vec{R}_x$ describes the relative motion of the projectile-like and the target-like nucleus. p and t label the energy level, $I_{t,p}$ describes the spin and $\xi_{t,p}$ the internal coordinates, so $\phi^{xy}_{I_y m_y}(\xi_y)$ with $y = t, p$ describes the states of projectile and target, respectively. The coupling of the relative angular momentum $\vec{L}$, $\vec{I}_p$ and $\vec{I}_t$ to the total angular momentum $\vec{J}_{\rm tot}$ can be done in two ways. Either by first coupling I_p and I_t to S, the so-called S-basis, or by first coupling L and I_p to J_p, the J-basis. For a given $J_{\rm tot}$ $\alpha = \{xpt, LI_pJ_pI_t\}$ labels a partial wave channel in the J-basis ($\beta = \{xpt, LI_pI_tS\}$ in the S-basis). The radial wave function is now written as $\psi_\alpha(r_x)$ instead of $\chi_L(r)$ and the total wave function

$$\begin{aligned}\Psi^{M_{tot}}_{xJ_{tot}}(\vec{r},\xi_p,\xi_t) &= \sum_\alpha \left[\left[i^L Y^M_L(\hat{r}_x)\otimes\phi^{xp}_{I_p m_p}(\xi_p)\right]_{J_p}\otimes\phi^{xt}_{I_t m_t}(\xi_t)\right]_{J_{\rm tot}M_{\rm tot}}\frac{\psi^{J_{\rm tot}}_\alpha(r_x)}{r_x}\\ &= \sum_\alpha |\alpha; J_{\rm tot}M_{\rm tot}\rangle\frac{\psi^{J_{\rm tot}}_\alpha(r_x)}{r_x}\end{aligned} \tag{2.10}$$

instead of $\psi(r,\vartheta)$, and similar for the S-basis.

Eq. 2.8 is then generalized to

$$\begin{aligned}\psi^{J_{\rm tot}\pi}_{\alpha\alpha_{\rm i}}(r_x) &= \frac{i}{2}\left[H^-_{L_{\rm i}}(\eta_\alpha,k_\alpha r_x)\delta_{\alpha\alpha_{\rm i}} - \mathbf{S}^{J_{\rm tot}\pi}_{\alpha\alpha_{\rm i}}H^+_L(\eta_\alpha,k_\alpha r_x)\right]\\ &= F_{L_{\rm i}}(\eta_\alpha,k_\alpha r_x)\delta_{\alpha\alpha_{\rm i}} + \mathbf{T}^{J_{\rm tot}\pi}_{\alpha\alpha_{\rm i}}H^+_L(\eta_\alpha,k_\alpha r_x)\end{aligned} \tag{2.11}$$

for $r_x > R_{\rm n}$, $\alpha_{\rm i}$ the incoming channel and $\pi = (-1)^L\pi_{xp}\pi_{xt}$ the total parity of the partial-wave channel. F_L is the regular Coulomb function with $2iF_L = H^+_L - H^-_L$.

2.1.3 Coupled equations

In order to find the channel wave functions $\psi_\alpha(r_x)$ one has to solve the Schrödinger equation for the whole system $[H-E]\Psi^{M_{tot}}_{J_{tot}\pi}$. The total Hamiltonian H

$$H = H_x + \hat{T}_x(r_x) + V_x(r_x,\xi_p,\xi_t) \tag{2.12}$$

contains the internal Hamiltonian $H_x = H_{xp}(\xi_p) + H_{xt}(\xi_t)$ (with $H_{xy}(\xi_y)\phi^{xy}_{I_y}(\xi_y) = \varepsilon_{xy}\phi^{xy}_{I_y}(\xi_y)$ for $y = p, t$, $\phi^{xpt} = \phi^{xt}\phi^{xp}$ and $\varepsilon_{xpt} = \varepsilon_{xp} + \varepsilon_{xt}$), the kinetic energy $\hat{T}$ and the interaction potential V. In the J-basis the Schrödinger equation (omitting $J_{\rm tot}$ and $M_{\rm tot}$)

$$\sum_\alpha [H - E]|\alpha\rangle \frac{\psi_\alpha(r_x)}{r_x} = 0 \tag{2.13}$$

can be projected onto a basis state by operating from the left with $r_x\langle\alpha'|$

$$\begin{aligned} \sum_\alpha r_{x'}\langle\alpha'|[H - E]|\alpha\rangle\psi_\alpha(r_x)r_x^{-1} &= 0 \\ \sum_\alpha (H - E)_{\alpha'\alpha}\psi_\alpha(r_x) &= 0 \end{aligned} \tag{2.14}$$

The matrix element $\langle\alpha'|[H-E]|\alpha\rangle$ may be written by either replacing H by $H_x+\hat{T}_x+V_x$ acting on the right side (the prior form) or by $H_{x'} + \hat{T}_{x'} + V_{x'}$ acting on the left side, the post form. In the prior form the matrix element is given by

$$\begin{aligned} (H - E)_{\alpha'\alpha} &= r_{x'}\langle\alpha'|[\hat{T}_x - E_{xpt} + V_x]|\alpha\rangle r_x^{-1} \\ &= r_{x'}\langle\alpha'|\alpha\rangle r_x^{-1}[\hat{T}_{xL} - E_{xpt}] + r_{x'}\langle\alpha'|[V_x]|\alpha\rangle r_x^{-1} \\ &= \hat{N}_{\alpha'\alpha}[\hat{T}_{xL} - E_{xpt}] + \hat{V}^{\rm prior}_{\alpha'\alpha} \end{aligned} \tag{2.15}$$

with $E_{xpt} = E-\varepsilon_{xp}-\varepsilon_{xt}$ and the overlap operator between the partial-wave basis states $\hat{N}_{\alpha'\alpha}$. Within one partition $x' = x$ these overlaps are diagonal $\hat{N}_{\alpha'\alpha} = \delta_{\alpha'\alpha}$. With these definitions Eq. 2.14 can be rewritten

$$[\hat{T}_{xL} - E_{xpt}]\psi_\alpha(r_x)r_x + \sum_{\alpha'} \hat{V}^{\rm prior}_{\alpha\alpha'}\psi_\alpha(r_{x'})r_{x'} + \sum_{\alpha',x'\neq x} \hat{N}_{\alpha\alpha'}[\hat{T}_{x'L'} - E_{x'p't'}]\psi_\alpha(r_{x'})r_{x'} = 0. \tag{2.16}$$

Here the third term is called non-orthogonality term. It involves the overlap of the basis functions $\langle\alpha'|\alpha\rangle$ between different mass partitions. These are in particular important for transfer reactions.

2.2 Integral equations

An alternative method to describe the scattering cross sections in terms of the S- or T-matrix is the use of the integral forms instead of the definition by the boundary condition (matching) of the differential equations. Separating the Coulomb from all other potentials V the coupled equations are

$$[E - T - V_{\rm C}]\,\psi_\alpha(r) = \sum_{\alpha'}\langle\alpha|V|\alpha'\rangle\psi_{\alpha'}(r') \equiv \Omega_\alpha(r) \tag{2.17}$$

with the source term $\Omega_\alpha(r)$. Using the Green's functions method the wave function can be written as

$$\begin{aligned}\psi &= \phi + \hat{G}^+\Omega \\ &= \phi + \hat{G}^+ V\psi \end{aligned} \tag{2.18}$$

with the Green's operator $\hat{G}^+ = [E-\hat{T}-V_\mathrm{C}]^{-1}$ with the kernel function $2\mu_x/\hbar^2 G^+(r,r')$. ϕ represents the homogeneous solution ($\Omega = 0$) and is only present in the elastic channel. Eq. 2.18 is called partial-wave Lippmann-Schwinger equation. Combining this and Eq. 2.11 the partial wave T-matrix is the integral

$$\mathbf{T} = -\frac{2\mu}{\hbar^2 k}\langle\phi^{(-)}|V|\psi\rangle = -\frac{2\mu}{\hbar^2 k}\int \phi(r)V(r)\psi(r)\mathrm{d}r \tag{2.19}$$

where $(-)$ is used to mark complex conjugation and this wave function satisfies the boundary condition for the incoming wave.

2.2.1 Two potential formula

If the potential can be decomposed in two parts $V(r) = U_1(r)+U_2(r)$ with the distorting potential U_1 and the remaining potential U_2, the T-matrix can as well be written in two terms. Let ϕ be the solution for no potential, so for each partial wave $\phi = F_L$, χ are the solutions for U_1 only, these are called distorted waves, and ψ the full solution. The Lippmann-Schwinger equations are given in table 2.1. The T-matrix integral

	Schrödinger Eq.	Lippmann-Schwinger Eq.	asympt. solution
free	$[E-T]\phi = 0$	$\hat{G}^+ = [E-T]^{-1}$	$\phi = F$
distorted	$[E-T-U_1]\chi = 0$	$\chi = \phi + \hat{G}^+U_1\chi$	$\chi \to \phi + \mathbf{T}^{(1)}H^+$
full	$[E-T-U_1-U_2]\psi = 0$	$\psi = \phi + \hat{G}^+(U_1+U_2)\psi$	$\psi \to \phi + \mathbf{T}^{(1+2)}H^+$

Table 2.1: Lippmann-Schwinger equations for the two potential formula. The full solution ψ can also be written as $\psi = \chi + \hat{G}_1^+U_2\psi$ using $\hat{G}_1^+ = [E-T-U_1]^{-1}$.

$\mathbf{T}^{(1)} = -2\mu/(\hbar^2 k)\langle\phi^{(-)}|V|\chi\rangle$ describes the scattering by potential U_1 only. This creates the distorted waves χ. Inserting the equations from table 2.1 the T-matrix for the combined potential can be written as

$$\begin{aligned}-\frac{\hbar^2 k}{2\mu}\mathbf{T}^{(1+2)} &= \int \phi(U_1+U_2)\psi\mathrm{d}r \\ &= \int (\chi - \hat{G}^+U_1\chi)(U_1+U_2)\psi\mathrm{d}r \\ &= \int \chi(U_1+U_2)\psi - \chi U_1\hat{G}^+(U_1+U_2)\psi\mathrm{d}r \\ &= \int \chi(U_1+U_2)\psi - \chi U_1(\psi-\phi)\mathrm{d}r \\ &= \langle\phi^{(-)}|U_1|\chi\rangle + \langle\chi^{(-)}|U_2|\psi\rangle \end{aligned} \tag{2.20}$$

This is called the two potential formula and is exact for the complex potentials U_1 and U_2. The matrix element $\langle\chi^{(-)}|U_2|\psi\rangle$ is called post T-matrix integral as the solutions χ for U_1 is in the final (post) channel. This can also be written in the prior form

$$\begin{aligned} \mathbf{T}^{(1+2)}_{\alpha\alpha_\mathrm{i}} &= \mathbf{T}^{(1)}_{\alpha\alpha_\mathrm{i}} - \frac{2\mu}{\hbar^2 k}\langle\chi^{(-)}_\alpha|U_2|\psi^{(+)}_{\alpha_\mathrm{i}}\rangle \qquad \text{post} \\ &= \mathbf{T}^{(1)}_{\alpha\alpha_\mathrm{i}} - \frac{2\mu}{\hbar^2 k}\langle\psi^{(-)}_\alpha|U_2|\chi^{(+)}_{\alpha_\mathrm{i}}\rangle \qquad \text{prior} \end{aligned} \tag{2.21}$$

where $(+)$ is used to mark outgoing boundary conditions.

2.3 Born approximations

In the Lippmann-Schwinger equation $\chi = \phi + \hat{G}^+ U\chi$ the wave function χ appears on both sides, this is an implicit equation. In order to find the solution this equation this equation can be iterated

$$\begin{aligned} \chi &= \phi + \hat{G}^+U\left[\phi + \hat{G}^+U\left[\phi + \hat{G}^+U\left[\ldots\right]\right]\right] \\ &= \phi + \hat{G}^+U\phi + \hat{G}^+U\hat{G}^+U\phi + \ldots \\ \mathbf{T} &= -\frac{2\mu}{\hbar^2 k}\langle\phi^{(-)}|U|\chi\rangle \\ &= -\frac{2\mu}{\hbar^2 k}\left[\langle\phi^{(-)}|U|\phi\rangle + \langle\phi^{(-)}|U\hat{G}^+U|\phi\rangle + \ldots\right] \end{aligned} \tag{2.22}$$

If the potential $U(r)$ is weak compared to the beam energy, it can be treated as a perturbation and the Born series might be truncated after the first term. This is called the plane-wave Born approximation (PWBA)

$$\begin{aligned} \mathbf{T}^{\mathrm{PWBA}} &= -\frac{2\mu}{\hbar^2 k}\langle\phi^{(-)}|U|\phi\rangle \\ f^{\mathrm{PWBA}}(\vartheta) &= \frac{\mu}{2\pi\hbar^2}\int e^{-i\vec{q}\cdot\vec{r}}U(r)\mathrm{d}^3r. \end{aligned} \tag{2.23}$$

The scattering amplitude is proportional to the Fourier transformed of the potential with the momentum transfer $\vec{q} = \vec{k} - \vec{k}_\mathrm{i}$. This approximation may be used if the potential is weak, so for example in e^--nucleus scattering.

2.3.1 Distorted wave Born approximation

In case of the two potential formula the Born series is written for the potential U_2

$$\mathbf{T}^{(1+2)} = \mathbf{T}^{(1)} - \frac{2\mu}{\hbar^2 k}\left[\langle\chi^{(-)}|U_2|\chi\rangle + \langle\chi^{(-)}|U_2\hat{G}_1^+U_2|\chi\rangle + \ldots\right] \tag{2.24}$$

if the potential U_2 is weak (it is not required for U_1 to be weak) this series may be truncated after the first term. This is called distorted wave Born approximation

(DWBA) as the wave functions χ are obtained from the distorting potential U_1. In cases where U_1 cannot cause transitions, i.e. if it is a central potential, $\mathbf{T}^{(1)} = 0$. In terms of the multi scattering coupled equation formalism presented in section 2.1.3 the first order DWBA can be written

$$\begin{aligned} \mathbf{T}^{\mathrm{DWBA}}_{\alpha\alpha_\mathrm{i}} &= -\frac{2\mu_\alpha}{\hbar^2 k_\alpha}\langle\chi^{(-)}_\alpha|U_2|\chi_{\alpha_\mathrm{i}}\rangle \\ &= -\frac{2\mu_\alpha}{\hbar^2 k_\alpha}\langle\chi^{(-)}_\alpha|r_x\langle\alpha|H-E|\alpha_\mathrm{i}\rangle r^{-1}_{x_\mathrm{i}}|\chi_{\alpha_\mathrm{i}}\rangle \end{aligned} \tag{2.25}$$

with the inner integration over the internal nuclear coordinates ξ. The DWBA T-matrix may be written in post or prior form.

$$\begin{aligned} \mathbf{T}^{\mathrm{DWBA\ post}}_{\alpha\alpha_\mathrm{i}} &= -\frac{2\mu_\alpha}{\hbar^2 k_\alpha}\langle\chi^{(-)}_\alpha|[\hat{T}_{xL}-E_{xpt}+U_\alpha]\hat{N}_{\alpha\alpha_\mathrm{i}}+\hat{V}^x_{\alpha\alpha_\mathrm{i}}|\chi_{\alpha_\mathrm{i}}\rangle \\ &= -\frac{2\mu_\alpha}{\hbar^2 k_\alpha}\langle\chi^{(-)}_\alpha|\hat{V}^x_{\alpha\alpha_\mathrm{i}}|\chi_{\alpha_\mathrm{i}}\rangle \\ \mathbf{T}^{\mathrm{DWBA\ prior}}_{\alpha\alpha_\mathrm{i}} &= -\frac{2\mu_\alpha}{\hbar^2 k_\alpha}\langle\chi^{(-)}_\alpha|\hat{V}^{x_\mathrm{i}}_{\alpha\alpha_\mathrm{i}}|\chi_{\alpha_\mathrm{i}}\rangle \end{aligned} \tag{2.26}$$

in first order DWBA the non-orthogonality terms $\hat{N}_{\alpha\alpha_\mathrm{i}}$ disappear because the wave functions χ are solution to $\chi^{(-)}_\alpha[\hat{T}_{xL}-E_{xpt}+U_\alpha]=0$.

2.4 The optical model

In a nuclear reaction the potential between the two nuclei is determining the scattering amplitude f and thus the cross section. In general the interaction potential between two nuclei can be complex, having negative imaginary as well as real parts, even if the microscopic interaction of two nuclei is real. The imaginary components are effective and arise because there are more reactions occurring than described by the spherical potential. These other reactions remove flux from the elastic scattering channel, and this can be described by a complex potential as shown in the following. Using a complex potential $V(r)+iW(r)$ the Hamiltonian is no longer Hermitian and the S-matrix not unitary, so $|\mathbf{S}_L| \neq 1$. With the time-dependent Schrödinger equation $(\hat{T}+V+iW)\psi = i\hbar\partial\psi/\partial t$ the loss of flux can be calculated.

$$\frac{\partial\psi^*\psi}{\partial t} = -\nabla\vec{j} + \frac{2}{\hbar}W\psi^*\psi = \frac{\partial\rho(r,t)}{\partial t} \tag{2.27}$$

W violates the continuity equation and for $W<0$ it removes flux from the incident beam. In analogy to the refractive index in optics which has an absorptive imaginary part the complex potential is called optical potential.

The typical form of the attractive interaction potential between two nuclei is a Woods-Saxon shape:

$$V(r) = \frac{-V_r}{1+\exp(\frac{r-R_0}{a})} \tag{2.28}$$

where V_r is around 50 MeV for protons, 100 MeV for deuterons and $150-180$ MEV for tritons, $R_0 = (A_1^{1/3} + A_2^{1/3})r_0$ with $r_0 \approx 1.2$ fm and the diffuseness $a \approx 0.6$ fm. The imaginary part is surface peaked for low energies and has shape like the derivative of Eq. 2.28. The depth W is fitted to experiments and usually $W = 10-20$ MeV. The radius parameter of the imaginary part is $r_W \gtrsim r_0$ and $a_W \approx a$. In addition a Coulomb potential is needed.

$$V_{\mathrm{C}}(r) = \begin{cases} \frac{Z_{\mathrm{p}} Z_{\mathrm{t}} e^2}{2R_{\mathrm{C}}} \left(3 - \frac{r^2}{R_{\mathrm{C}}^2}\right) & r \leq R_{\mathrm{C}} \\ \frac{Z_{\mathrm{p}} Z_{\mathrm{t}} e^2}{r} & r > R_{\mathrm{C}} \end{cases} \tag{2.29}$$

The typical shape of the potentials is shown in Fig. 2.1. The depth of the real part of the

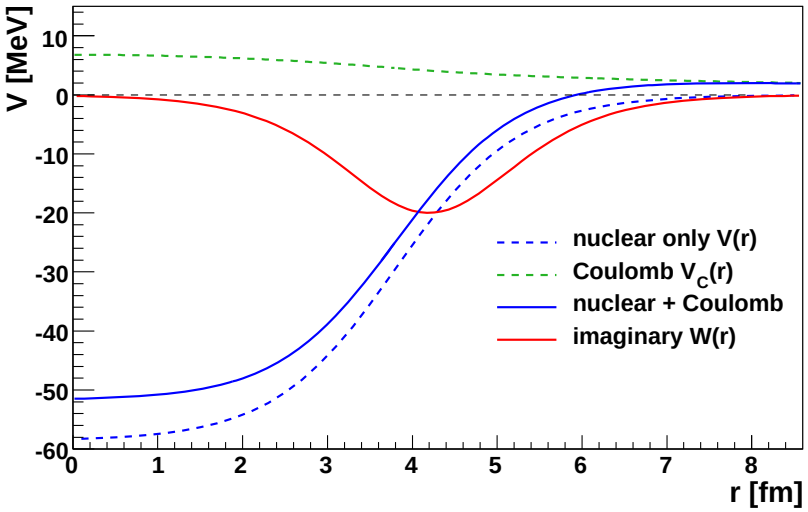

Figure 2.1: Optical potentials using a Wood-Saxon form for the real nuclear part (dashed blue), the Coulomb potential (dashed green) and the combined nuclear and Coulomb real potential (solid blue) together with a surface peaked imaginary potential (red) with the shape of the derivative of the Wood-Saxon form.

optical potential gets smaller with increasing beam energy with about $\partial V_r/\partial E \approx 0.3$ and it is approximately proportional to the number of nucleons in the light reaction partner (≈ 50 MeV for nucleons, ≈ 100 MeV for deuterons).

2.4.1 Global optical model parameters

The parameters of the optical potentials have been fitted to experimental scattering data for large ranges of mass A and beam energies. This results in global scaling relations which can be used for interpolation. Such scaling relations are for example given in [PER76, DAE80, BEC69]. The Triton scaling for V and W from [PER76] is

$$\begin{aligned} V &= 165 - 0.17E - 6.4(N-Z)/A \\ W &= 46.0 - 0.33E - 110(N-Z)/A. \end{aligned} \tag{2.30}$$

The global parameters have been obtained from stable beam experiments, typically the lowest beam energies are $10-20$ MeV, while the beam energies at REX-ISOLDE correspond to normal kinematics energies $E_{\mathrm{d}} \approx 6$ MeV for deuterons. Also the dependence on the asymmetry $(N-Z)$ is quite strong (see Eq. 2.30) and it is not clear whether this is appropriate for exotic nuclei. In general the description of elastic scattering with global parameter sets is worse than with a fitted potential. Thus in this thesis the potential parameters have been fitted to the elastic scattering which is measured simultaneously with the transfer reaction.

2.5 Transfer reactions

In this section the equations derived above are applied to the calculation of the transfer amplitude. In a transfer reaction one nucleon or a cluster is transferred from the target to the projectile (pickup) or vice versa (stripping)[2]. For a transfer reaction like the

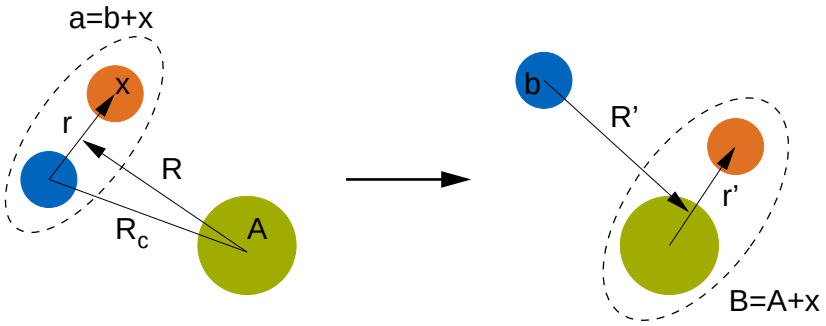

Figure 2.2: Coordinates for the A(a,b)B transfer reaction. R_c is the core-core distance, $\vec{R}$ and $\vec{R}'$ are the distances between projectile and target, or ejectile and recoil, while $\vec{r}$ and $\vec{r}'$ refer to the distances of the cluster to its core.

(d,p) reaction a+A→b+B or A(a,b)B with B=A+x and a=b+x the coordinates used in the following are shown in Fig. 2.2. The internal wave functions are described by

$$\begin{aligned} [H_t - \varepsilon_t]\,\phi_t(\vec{r}) &= [T_r + V_t(\vec{r}) - \varepsilon_t]\phi_t(\vec{r}) = 0 \\ [H_p - \varepsilon_p]\,\phi_p(\vec{r}') &= [T_{r'} + V_p(\vec{r}') - \varepsilon_p]\phi_p(\vec{r}') = 0 \end{aligned} \tag{2.31}$$

with the binding potentials $V_t = V_{\mathrm{bx}}$ and $V_p = V_{\mathrm{Ax}}$ which are fitted to reproduce the separations energies. The total Hamiltonian involves these binding potentials as well as the core-core optical potential U_{bA} and can be written either in the prior or in the post representation

$$\begin{aligned} H &= T_r + T_R + V_{\mathrm{bx}}(\vec{r}) + V_{\mathrm{Ax}}(\vec{r}') + U_{\mathrm{bA}}(\vec{R}_c) = \\ H^{\mathrm{prior}} &= T_R + U_{\mathrm{i}}(R) + H_p(\vec{r}) + V^{\mathrm{prior}}(\vec{R},\vec{r}) = \\ H^{\mathrm{post}} &= T_{R'} + U_{\mathrm{f}}(R') + H_t(\vec{r}') + V^{\mathrm{post}}(\vec{R}',\vec{r}') \end{aligned} \tag{2.32}$$

[2]These names refer to normal kinematics. In the following only reactions were neutrons are transferred from the light reaction partner (d or t) to the heavy one are discussed.

where the $U_{\mathrm{i,f}}$ are diagonal potentials (U_1 in section 2.2.1) for the incoming or outgoing channel. The potentials creating the transition from one channel to the other are the interaction terms containing the binding potentials and the remnant terms which are similar in magnitude and often neglected.

$$\begin{aligned} V^{\mathrm{prior}} &= V_{\mathrm{bx}}(\vec{r}) + U_{\mathrm{bA}}(\vec{R}_c) - U_{\mathrm{i}}(R) \\ V^{\mathrm{post}} &= V_{\mathrm{Ax}}(\vec{r}) + U_{\mathrm{bA}}(\vec{R}_c) - U_{\mathrm{f}}(R') \end{aligned} \tag{2.33}$$

The potentials $U_{\mathrm{i,f}}$ are used to obtain the distorted waves $\chi_{\mathrm{i,f}}$ in the incoming and outgoing channel and with them the T-matrix can be calculated using Eq. 2.26.

The inputs required to calculate the transfer reaction are

(a) the optical potentials for incoming U_{i} and outgoing U_{f} channel to get the distorted waves,

(b) the binding potentials with the depth fitted to reproduce binding energies V_{bx} and V_{Ax} and the quantum numbers nlj of the final states in order to calculated the overlap functions $\phi_{I_{\mathrm{A}},I_{\mathrm{B}}}$ and $\phi_{I_{\mathrm{a}},I_{\mathrm{b}}}$, and

(c) the core-core interaction U_{bA}

2.5.1 Angular distributions

In a semi-classical picture the position of the first maximum of the differential cross section as a function of angle can be related to the angular momentum transfer L. If the nucleons is placed in an orbit with $L = Rq$ where q is the momentum transfer which is related to the scattering angle ϑ by $q^2 = p_{\mathrm{i}}^2 + p_{\mathrm{f}}^2 - 2p_{\mathrm{i}}p_{\mathrm{f}}\cos\vartheta$, the scattering angle is related to $L \propto \sin(\vartheta/2)$. The proportionality factor depend on the energies and masses of the reaction partners.

The dependence of the shape of the cross section on the angular momentum transfer can be best seen in the zero range approximation (neglecting remnant terms and assuming an interaction potential of zero range $V\phi(\vec{r}) = D_0\delta(\vec{r})$). Using for simplicity the plane-wave approximation the T-matrix is

$$\begin{aligned} T_{\mathrm{fi}}^{\mathrm{PWBA}} &= D_0 \int e^{-i\vec{q}\cdot\vec{r}}\phi_{I_{\mathrm{A}},I_{\mathrm{B}}}(\vec{r})\mathrm{d}^3r \\ &= \sum_{L=0}^{\infty} i^L(2L+1)\int \frac{F_L(0,qr)}{qr}P_L(\cos\vartheta)\phi_{I_{\mathrm{A}},I_{\mathrm{B}}}(\vec{r})\mathrm{d}^3r \end{aligned} \tag{2.34}$$

with the angular momentum transfer L and the momentum transfer $\vec{q}$. The sum just contains those L values which appear in the overlap function. So for a single value of L the cross section as a function of q (ϑ) is proportional to the regular Coulomb function squared $|F_L(0,qr)|^2$ (for $\eta = 0$ the regular Coulomb functions are related to the more known Bessel functions $F_L(0,x)/x = j_L(x)$).

Even if the distorted wave Born approximation is used the general features remain, for higher L the first maximum of the cross section gets shifted to larger ϑ_{cm} and the overall cross section gets smaller. This is shown in Fig. 2.3.

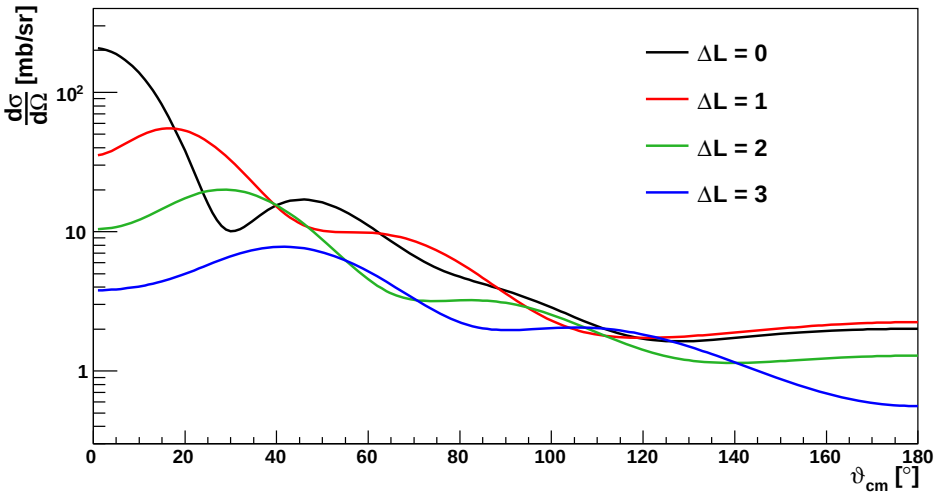

Figure 2.3: Angular distributions for different ΔL for a (d,p) reaction. The first maximum of the cross section gets shifted to larger ϑ_{cm} and the overall cross section gets smaller for increasing ΔL.

2.5.2 Energy dependence

The transfer cross section depends of course on the center of mass energy, so on the incoming beam energy. But not only the total cross section, also the angular distribution change with the available energy. This is shown in Fig. 2.4 for the d(^{94}Sr,p)^{95}Sr reaction which is of interest for future experiments at HIE-ISOLDE. Although the maximum total cross section for $\Delta L = 0$ transfer is for a beam energy between 3 and 5 MeV/u, the shapes for angular momentum transfer $\Delta L = 0$ and 2 are very similar for low energies. For the current REX-ISOLDE beam energy of 3 MeV/u both angular distributions are rather flat. The only difference below $\vartheta_{\mathrm{cm}} = 20°$ is in a region where the detection efficiency of the setup is small. Thus transfer reactions are at the moment limited to nuclei with mass below around 50 or to very intense beams in order to obtain sufficient statistics to extract the small differences in the angular distribution.

2.5.3 Q-value matching

The transfer cross section strongly depends on the Q-value of the reaction. This is shown in Fig. 2.5. For the transfer of a neutral particle the cross section is largest for $Q = 0$, so by choosing a specific reaction the population of certain states can be favored, for example (p,d) ($Q = 2.2$ MeV) populates low-lying and (^{3}He,α) ($Q = 19.8$ MeV)

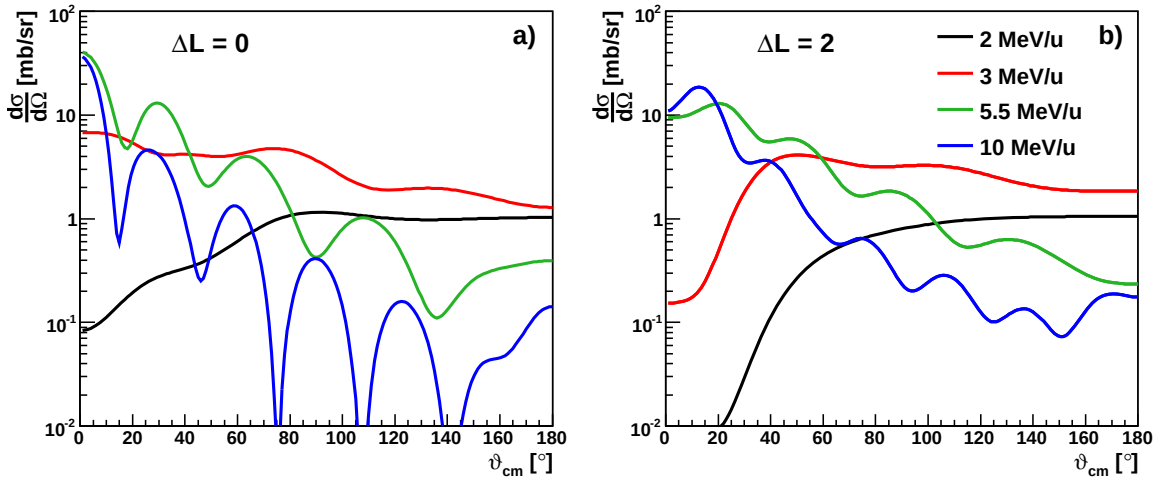

Figure 2.4: Energy dependence of the transfer cross section for the d(^{96}Sr,p)^{97}Sr reaction, a) $\Delta L = 0$, b) $\Delta L = 2$. For the current REX-ISOLDE beam energy of 3 MeV/u both angular distributions are rather flat. The only difference below $\vartheta_{\mathrm{cm}} = 20°$ is in a region where the detection efficiency of the setup is small. For larger energies the shapes of the angular distributions are more distinctive.

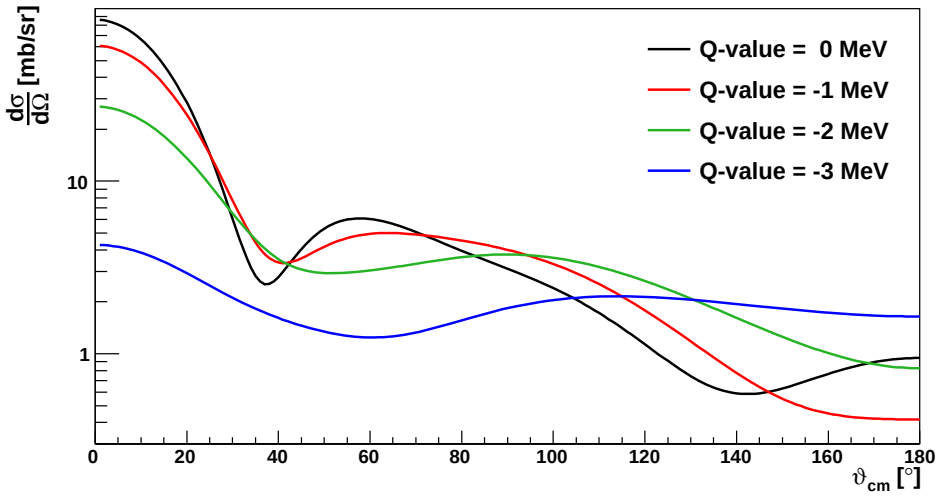

Figure 2.5: Angular distributions for different Q-values for a (d,p) reaction. The larger the Q-value mismatch the smaller the cross section.

highly excited states. In addition to that, the latter reaction also strongly favors high ΔL transfers [BOY70].

2.5.4 Spectroscopic factors

In order to calculate the transfer amplitude the knowledge of the overlap function $\phi = \langle \Phi_{\rm A} | \Phi_{\rm B} \rangle$ of core A $\Phi^{\rm A}_{I_{\rm A}}(\xi_{\rm A})$ and final nucleus B $\Phi^{\rm B}_{I_{\rm B}}(\xi_{\rm B})$ is required. ϕ measures the amplitude for adding a valence particle to A in state $I_{\rm A}$ and forming the state $I_{\rm B}$ in B. So the state $I_{\rm B}$ can be written as a superposition of all orthogonal core states

$$\Phi^{\rm B}_{I_{\rm B}}(\xi_{\rm A}, \vec{r}) = \sum_{I_{\rm A}} \phi_{I_{\rm A}, I_{\rm B}} \Phi^{\rm A}_{I_{\rm A}}(\xi_{\rm A}). \tag{2.35}$$

This overlap function is expanded in partial waves

$$\begin{aligned} \Phi^{\rm B}_{I_{\rm B}}(\xi_{\rm A}, \vec{r}) &= \sum_{I_{\rm A}, lsj} \left[\varphi_{lsj}(\vec{r}) \otimes \Phi^{\rm A}_{I_{\rm A}}(\xi_{\rm A}) \right]_{I_{\rm B}} \\ &= \sum_{I_{\rm A}, lsj} u^{j I_{\rm A} I_{\rm B}}_{lsj}(r)/r \left[\left[Y_l(\hat{r}) \otimes \chi_s \right]_j \otimes \Phi^{\rm A}_{I_{\rm A}}(\xi_{\rm A}) \right]_{I_{\rm B}} \\ &= \sum_{I_{\rm A}, lsj} A^{j I_{\rm A} I_{\rm B}}_{lsj} v^{j I_{\rm A} I_{\rm B}}_{lsj}(r)/r \left[\left[Y_l(\hat{r}) \otimes \chi_s \right]_j \otimes \Phi^{\rm A}_{I_{\rm A}}(\xi_{\rm A}) \right]_{I_{\rm B}} \end{aligned} \tag{2.36}$$

as the radial wave functions $u^{j I_{\rm A} I_{\rm B}}_{lsj}(r)$ are not normalized, they are written as the product of the normalized wave function $v^{j I_{\rm A} I_{\rm B}}_{lsj}(r)$ and the spectroscopic amplitude or coefficient of fractional parentage A. The square of A

$$S^{j I_{\rm A} I_{\rm B}}_{lsj} = |A^{j I_{\rm A} I_{\rm B}}_{lsj}|^2 \tag{2.37}$$

is the spectroscopic factor. The differential cross section is proportional to the spectroscopic factor. Since $\Phi^{\rm A}$, $\Phi^{\rm B}$, and $v^{j I_{\rm A} I_{\rm B}}_{lsj}(r)$ are normalized to unity the sum rule for the spectroscopic amplitude is

$$\sum_{I_{\rm A}, lsj} |A^{j I_{\rm A} I_{\rm B}}_{lsj}|^2 = \sum_{I_{\rm A}, lsj} S^{j I_{\rm A} I_{\rm B}}_{lsj} = 1 \tag{2.38}$$

where the sum is over all initial states $I_{\rm A}$.

For large distances outside the nuclear range the bound state wave functions, and thus the overlap functions, are proportional to a Whittaker function

$$\phi_{I_{\rm A}, I_{\rm B}} \xrightarrow{r > R_{\rm n}} C^{\rm A,B}_{lj} W_{-\eta, l+1/2}(-2k_{\rm x} r) \approx C^{\rm A,B}_{lj} e^{-k_{\rm p} r}. \tag{2.39}$$

The wave function $u_{jl}(\vec{r})$ has the same asymptotic behavior with a normalization b_{lj}. The product $C^{\rm A,B}_{lj} = A^{j I_{\rm A} I_{\rm B}}_{lsj} b_{lj}$ is called the asymptotic normalization coefficient (ANC). In peripheral reactions the cross section is proportional to $(C^{\rm A,B}_{lj})^2 = S^{j I_{\rm A} I_{\rm B}}_{lsj} (b_{lj})^2$ and not on the spectroscopic factor alone. b_{lj} is determined by the potential parameters and here the uncertainty is large for low energy reactions. ANCs are interesting for nuclear astrophysics as they determine the capture rate A(x,γ)B in the limit of zero energy. Due to the low beam energy as used for the experiments described in this thesis

spectroscopic factors should not be extracted [THO09]. Thus in this thesis S refers to the cross section scaling factor. A recent study compared the cross section scaling factors for the d(^{54}Fe,p)^{55}Fe obtained in normal kinematics (E_{d}=14 MeV) and inverse kinematics (E_{Fe}=2.5 MeV/u $\widehat{=}$ E_{d}=5.2 MeV) [MAH08]. For some states in ^{55}Fe the extracted scaling factors agree, while for others they differ by up to factors of 10.

2.6 Predictions for t(^{30}Mg,p)^{32}Mg

In this section the formalism derived above is applied to the specific case of the t(^{30}Mg,p)^{32}Mg reaction. In one nucleon transfer reactions the angular distribution is sensitive to the orbital angular momentum of the state into which the nucleon is transferred. In a two nucleon transfer reaction, however, the angular momentum is carried by a pair of nucleons and thus does not reflect the angular momentum of the single particle state the nucleons are transferred to. Only the sum of two single particle angular momenta must give the transferred angular momentum. There are many different ways how the angular momentum can be shared between them and thus all possibilities consistent with the structure of the initial and final state add up coherently. This can produce large cross sections for constructive and very small ones for destructive interference, depending on the correlation between the two nucleons.

2.6.1 Sequential and simultaneous transfer of two neutrons

The transfer amplitude for two neutron transfer contains two components, the one step (simultaneous) and the two step (sequential) process. The sum of both gives the differential cross section

$$\left(\frac{\mathrm{d}\sigma}{\mathrm{d}\Omega}\right) = |f_{\mathrm{sim}}(\vartheta) + f_{\mathrm{seq}}(\vartheta)|^2. \tag{2.40}$$

In principle this sum also includes a non-orthogonality term, however it vanishes in first order DWBA, and by choosing a prior-post combination it can also be avoided in the second-order DWBA [UDA73, THO09]. In Fig. 2.6 the individual contributions and the sum are shown for $\Delta L = 0, 1, 2$ transfer in the t(^{30}Mg,p)^{32}Mg reaction. The two-step cross section is at least one order of magnitude lower than the one-step process. This is due to the large negative Q-value of the t(^{30}Mg,d) reaction to the intermediate nucleus ^{31}Mg. This Q-value is -3.9 MeV, while the one for the (t,p) reaction is very small (-0.295 MeV). Fig. 2.7 a) shows the energy levels for the t(^{30}Mg,p) reaction. This makes the simultaneous transfer energetically favored. In the case of the t(^{44}Ar,p)^{46}Ar reaction, which is also discussed in this thesis (see chapter 6), the Q-value of the (t,d) reaction is quite small (-1.1 MeV) and both sequential and simultaneous transfer are possible (Fig. 2.7 b)). The Q-value of the t(^{44}Ar,p) reaction reaction is -4.7 MeV, this favors the population of higher lying states (see Fig. 6.8 in section 6.3). In Fig. 2.6 it can be seen that the interference of one- and two-step processes is destructive for $\Delta L = 0$ and 2 while it is constructive for negative parity. The cross sections for the

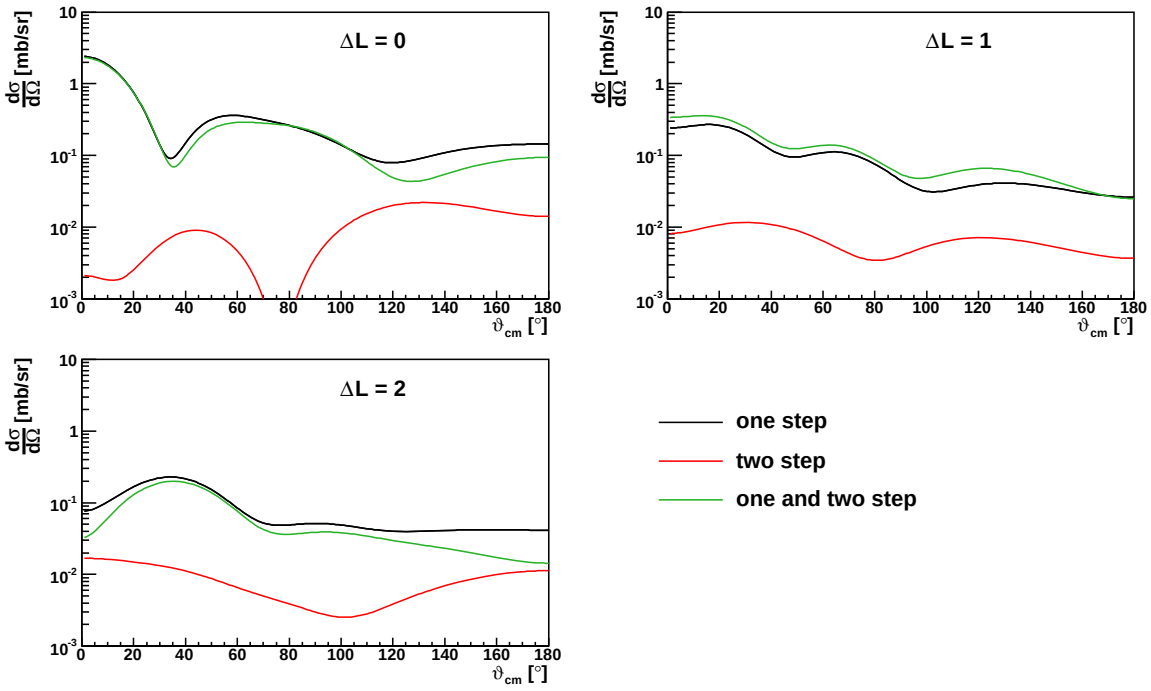

Figure 2.6: Second order calculation of the two neutron transfer cross section. The individual contributions from one- and two-step processes as well as the sum are shown for $\Delta L = 0, 1, 2$.

individual processes are proportional to their individual spectroscopic factors. The contribution of sequential transfer might be even lower than shown in Fig. 2.6 where a spectroscopic factor of $S = 1$ was assumed for all transitions. At least for the d(^{30}Mg,p) reaction the spectroscopic factors are significantly smaller than unity [BIL10] for all states observed in this experiment. As the inclusion of sequential transfer does not change the shape nor the spectroscopic factor extracted from experiment and in the experiment no indications for a t(^{30}Mg,d) reaction have been observed, in the following and in the analysis presented in chapter 5 only simultaneous transfer is considered.

2.6.2 Expected cross section

Fig. 2.8 shows the calculated differential cross section for the t(^{30}Mg,p) reaction at 1.8 MeV/u for the known states in ^{32}Mg, the predicted 0^+ state at 1500 keV and a hypothetical 1^- state. The configuration assumed for the different states is shown in table 2.2.

Due to the different shapes of the angular distribution the 0^+ states can clearly be identified. The absolute cross section depends on the structure of the populated state. The population of the excited 0^+ state is expected to be favored, since it has a similar structure as the ground state of ^{30}Mg. The angle integrated cross section of a few mb for the excited 0^+ state results in a count rate of $1 - 4$ protons/h per state with

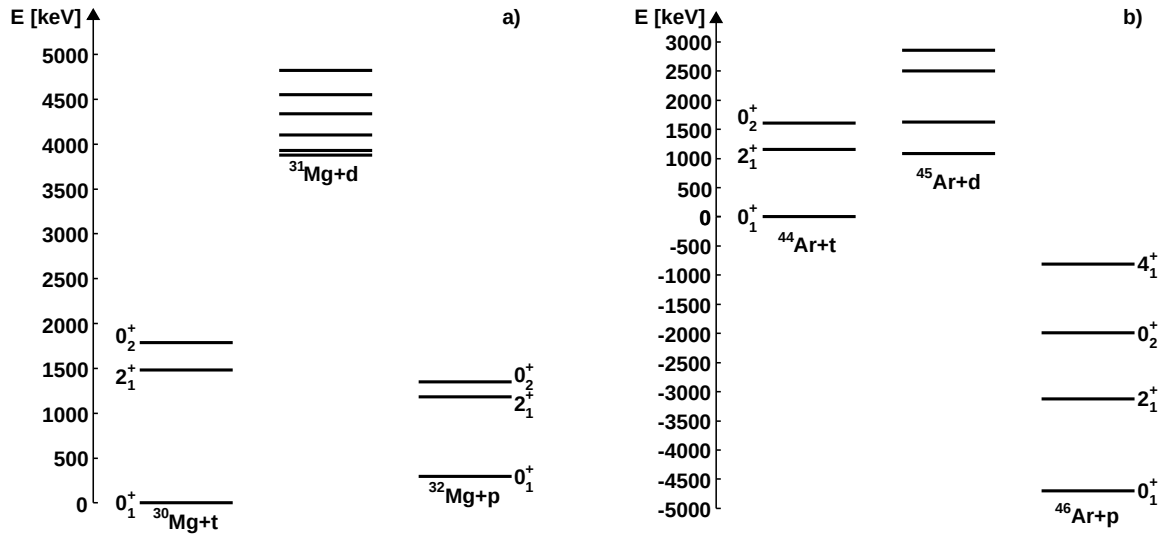

Figure 2.7: Energy levels for the (t,p) two neutron transfer reactions on ^{30}Mg and ^{44}Ar. In the case of Mg the Q-value of the (t,d) reaction is -3.9 MeV. This disfavors the sequential transfer compared to the simultaneous one. For the t(^{44}Ar,d)^{45}Ar reaction the Q-value is negative as well but only -1.1 MeV. Thus here both sequential and simultaneous transfer are possible.

state	$0^+_{\rm gs}$	2^+_1	0^+_2	1^-_1	2^+_2	3^-_1
E [keV]	0	886	1500	1500	2858	3133
configuration	$(p_{3/2})^2$	$(d_{3/2})^2$	$(s_{1/2})^2$	$(p_{3/2})(d_{3/2})$	$(p_{3/2})(f_{7/2})$	$(d_{5/2})(f_{7/2})$

Table 2.2: Configurations of states in ^{32}Mg used for the predictions shown in Fig. 2.8. Spectroscopic amplitudes have been set to unity for all states.

the expected beam intensity of $1 \cdot 10^5$ ^{30}Mg/s. This allows to measure the angular distributions within a beam time of 10 days [KRÖ08].

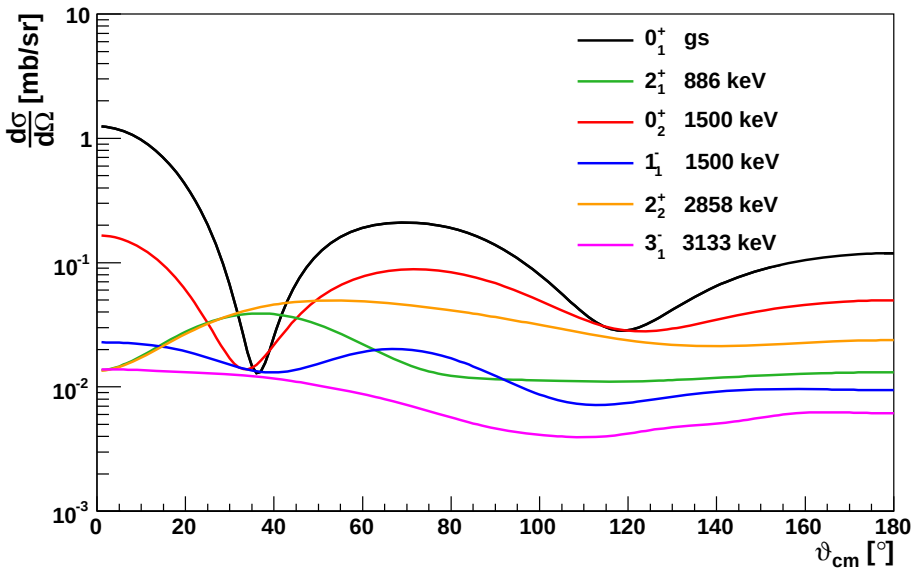

Figure 2.8: Expected differential cross sections for the t(^{30}Mg,p) reaction. The angular distributions for known states as well as for a predicted 0^+ state at 1500 keV and a hypothetical 1^- state are shown. The shape of the angular distribution allows to clearly identify the $\Delta L = 0$ transfer reaction to the 0^+ states.

3 The experimental setup at REX-ISOLDE

At an ISOL facility like ISOLDE radioactive isotopes are produced by spallation, fission, or fragmentation reactions in a thick target irradiated by light particles like neutrons or protons. In contrast to in-flight production facilities like GSI, MSU, or RIKEN, where a heavy beam is fragmented in-flight, at ISOL facilities the reaction products are produced at rest. Thus, they have to be extracted out of the target, ionized, and then accelerated. This procedure is described in the following section focusing on the special settings used in the described experiments.

3.1 Production of radioactive ion beams at ISOLDE

At the ISOLDE facility (CERN) the radioactive ions are produced by a 1.4 GeV proton beam from the PS-Booster impinging on a thick Uranium Carbid (UC_x) target. On average the PS-Booster supplies $3 \cdot 10^{13}$ protons every 2.4 s to ISOLDE. This is equivalent to a 2 μA dc beam. The produced isotopes then have to diffuse out of the target to its surface from where they can be extracted. Already at this stage a chemical selection can be applied by the choice of the target materials which alters the diffusion of the atoms. The extracted atoms have to be ionized to be accelerated and mass separated. For the ionization of ^{30}Mg the Resonant Ionization Laser Ion Source (RILIS) [MIS93] was used. In the RILIS the atoms of interest are excited by one or more resonant laser beams and then ionized. This reduces the isobaric contamination of the beam. The ionization potential of Mg amounts to 7.646 eV $\widehat{=}$ 61671.05 cm^{-1}, the ionization scheme is shown in Tab. 3.1 [FED00].

state	configuration	wave number [cm^{-1}]	excitation wavelength [nm]
0	$3s^2\ ^1S_0$	0	
1	$3s3p\ ^1P_1$	35051.26	285.2
2	$3s4d\ ^1D_2$	53134.64	552.8
3	continuum	>61671.05	510.6, 578.2

Table 3.1: Ionization scheme for Mg used at RILIS [FED00]. Mg is first excited in 2 steps to the $3s4d\ ^1D_2$ state and then ionized to the continuum. This multi-step process guarantees an element specific, selective ionization of the desired species.

The ion source efficiency for Mg isotopes is almost 10% [FED00]. The selectivity is garantueed by the choice of element specific excitation steps. With the selective laser ionization even an isomer separation can be achieved [KÖS00]. As the cavity where the atoms interact with the laser is heated, thermal ionization of atoms may also occur which leads to a contamination of the beam. Major contributions to the beam composition as well as their analysis are described in section 3.3.

The produced 1^+ ions are then accelerated to 30-60 keV by an electric field and guided to the mass separator. The ISOLDE facility uses two target stations with two independent mass separators that can both deliver their mass separated beams to various experiments (see Fig. 3.1). The General Purpose Separator (GPS) allows to select 3 masses within a mass range of $\pm 15\%$ and a mass resolution of $M/\Delta M = 2400$. The second separator, the High Resolution Separator (HRS), has a much higher resolving power of more than 30000, however the RILIS efficiency is lower due to the longer optical path length to the HRS. For the experiment described in this thesis the GPS was used.

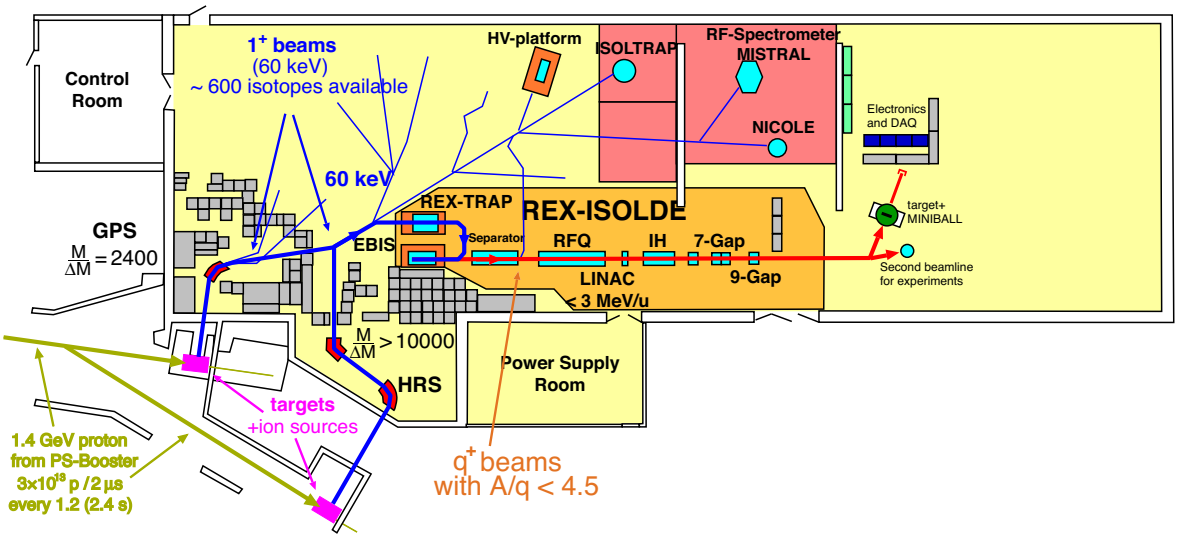

Figure 3.1: Layout of the ISOLDE hall. The two target stations with the GPS and HRS can be seen, as well as the beam distribution system to the various experiments.

3.2 The post-accelerator REX

With the low energy beam provided by the ISOLDE facility nuclear structure studies are limited to mass measurements, laser spectroscopy and decay experiments. To overcome this limitation and study exotic nuclei by Coulomb excitation and transfer reactions the post-accelerator REX was constructed at ISOLDE. It is described in great detail in [AME05, HAB00]. The ions are first collected, cooled, and bunched in the

REX-TRAP, a Penning trap. Here the ions are stopped by a retardation potential of 60 kV to energies of some eV and then further cooled by the Ar buffer gas. After a cooling time of 20 ms (corresponding to a bunch repetition rate at the experiment of 50 Hz) they are transferred to the EBIS electron beam ion source for charge breeding. In the experiment described here a breeding time of 8 ms to charge state 7+ was chosen. The charge state is chosen in such a way that no stable contaminant from buffer and rest gas in the REX-TRAP and EBIS has the same or very similar mass-to-charge (A/q) ratio. Finally, the ions with $A/q < 4.5$ (for $^{30}Mg^{7+}$ $A/q = 4.285$) are accelerated to energies of up to 3.0 MeV/u with the REX-LINAC. The linac consists of a RFQ, an IH-structure, three 7-gap resonators, and one 9-gap resonator. However, in the present experiment the beam energy had to be lowered to 1.83 MeV/u in order to avoid fusion reactions with the target carrier material Ti (see section 3.6). Therefore, the 9-gap and the last 7-gap resonator were switched off. The transmission of the ^{30}Mg beam from the ion source to the target at the MINIBALL setup was measured to be 9.3 %.

3.3 Beam composition

Due to the production mechanism of radioactive isotopes pure beams are not available at ISOLDE. Contaminating isobars are produced in the target as well as by β decay in the traps. Another source of contamination comes from stable ions from the buffer gas in the EBIS. For the analysis of the beam composition two independent methods have been used. The overall beam composition can be measured with the Bragg chamber [WEI06] at the beam dump about 4 m behind the target. Fig. 3.2 shows the energy loss versus the total energy detected in the Bragg chamber. The energy loss depends on the charge Z of the nucleus, the total energy should be the same for all $A = 30$ isobars. As there is a 2 μm Mylar entrance foil before the chamber, ions with higher Z have already lost more energy before they enter the detection volume, thus higher Z are more to the left in Fig. 3.2. The total Al content of the beam can be estimated to 15.0(37) %. However, the Bragg chamber was not operating during the whole beam time, and thus only snapshots of the beam composition are available.

Another independent method to obtain the beam composition is the analysis of the release time of ions from the ISOLDE target. By plotting the time difference between the detection of a particle in T-REX and the arrival time of the proton pulse at the ISOLDE target (T1 pulse) the composition of the beam released from the target can in principle be obtained. This method does not measure the decay of the radioactive beam during trapping and breeding as the time structure of the Al decay products is the same as for Mg from the ion source. However, a significant amount of beam is deposited in the chamber and thus most of the detected events in T-REX are electrons from β decay. Thus, separate time spectra have been generated for the different particle types (Fig. 3.3). The release curves fitted to the spectra is given in [LET97], initial parameters were taken from [KÖS03] where the release of stable Mg has been measured. The fast release time of ^{30}Mg is 125(2) ms, which agrees with the expected value of 121 ms when folding the fast release time of stable Mg (190 ms) with the half-life of

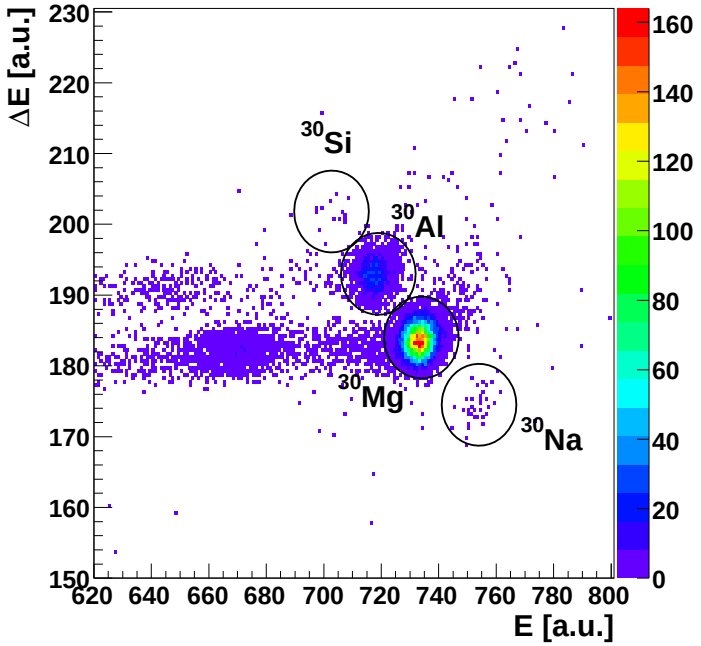

Figure 3.2: Beam identification in the Bragg chamber using the energy loss ΔE and the total energy E. The beam contains in addition to ^{30}Mg and 15 % ^{30}Al a very small fraction of ^{30}Si and ^{30}Na ($< 0.3\%$).

^{30}Mg ($t_{1/2} = 335(17)$ ms). The result for the beam composition is shown in Table 3.2. As the stopped particle cuts for protons and tritons still contain electrons an average of 10.8(14) % of ^{30}Al in the ISOLDE beam has been determined. During the trapping

method	Al [%]	Al [%] cut $t < 1.2$ s
release curve average	11.3(14)	6.7(15)
all tritons	12.7(1)	9.1(1)
identified tritons	10.1(4)	5.0(4)
transfer protons	9.6(2)	6.0(3)
elastic scattered protons	12.9(4)	6.9(1)
		comment
minimum time in REX-TRAP	1.64(8)	8 ms breeding
maximum time in REX-TRAP	5.61(27)	28 ms trapping and breeding
decay during trapping and breeding	3.64(18)	average time in traps
Bragg chamber	15.0(37)	

Table 3.2: Beam composition determined by different methods. The release curve analysis only measures the composition of the ISOLDE beam, additional contamination is produced by decay in the REX-TRAP and EBIS. The Bragg chamber measured the total beam composition.

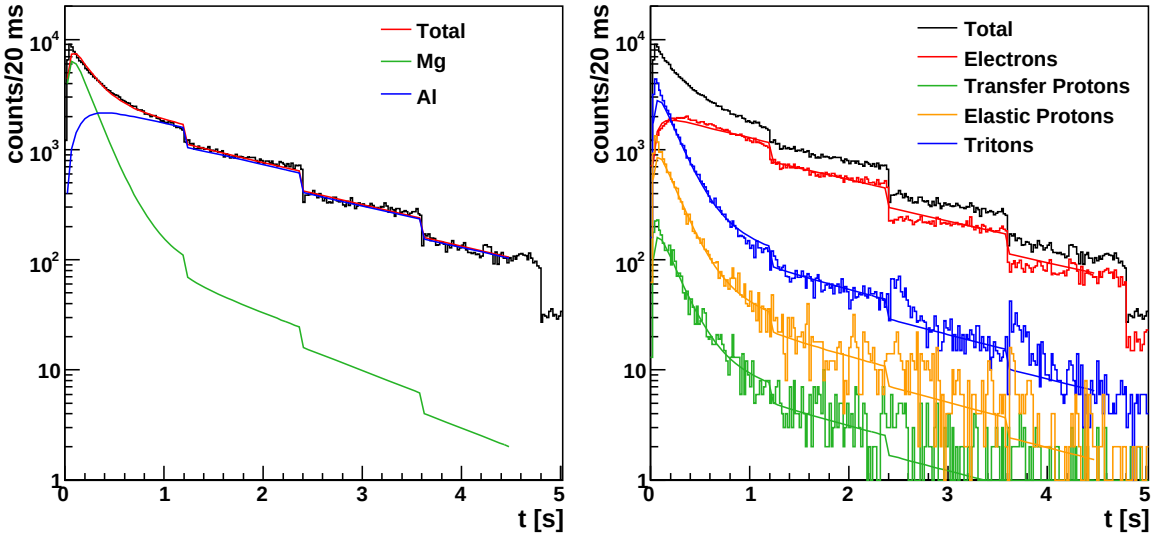

Figure 3.3: Time difference between detection of a particle in T-REX and the arrival time of the proton pulse at the ISOLDE target. This shows the release of ions from the primary target. Most of the detected particles are electrons from β decay of stopped beam (left panel). The right panel shows the release curves obtain when gating on different particle types identified in T-REX.

and breeding the produced isotopes can decay, but the product ^{30}Al has the same time structure as ^{30}Mg. The amount of ^{30}Al produced by decay during trapping and breeding can be estimated using the half-lives of ^{30}Mg and ^{30}Al. The ions spend a maximum time of 28 ms (20 ms trapping and 8 ms breeding) in the traps, the minimum decay time is given by just the breeding time. Averaged over this time window additional 3.64(18) % of Al in the beam is expected. It should be noted that due to the recoil energy of the daughter nucleus additional losses of Al in the trap can not be excluded. This has been observed for the case of ^{61}Mg [WAL09]. For the ^{30}Mg β-decay the maximum recoil energy of the daughter nucleus is around 1 keV (Q_β = 6.961 MeV) and the trapping potentials are around 100 kV. Adding amount of Al produced by in-trap decay to the ISOLDE contamination a total Al content of 14.4(14) % in the beam is expected, which agrees with the value determined by the Bragg chamber. By taking only particles which are detected during the first 1.2 s after the proton impact, the ^{30}Al contamination can be reduced to 10.4(23) %.

3.4 The setup for transfer reactions

For the study of nucleon transfer reactions at REX-ISOLDE a special particle detector system has been constructed [BIL07, BIL10] based on $\Delta E - E$ telescopes for particle identification. A picture of the T-REX setup is shown in Fig. 3.4. All detector

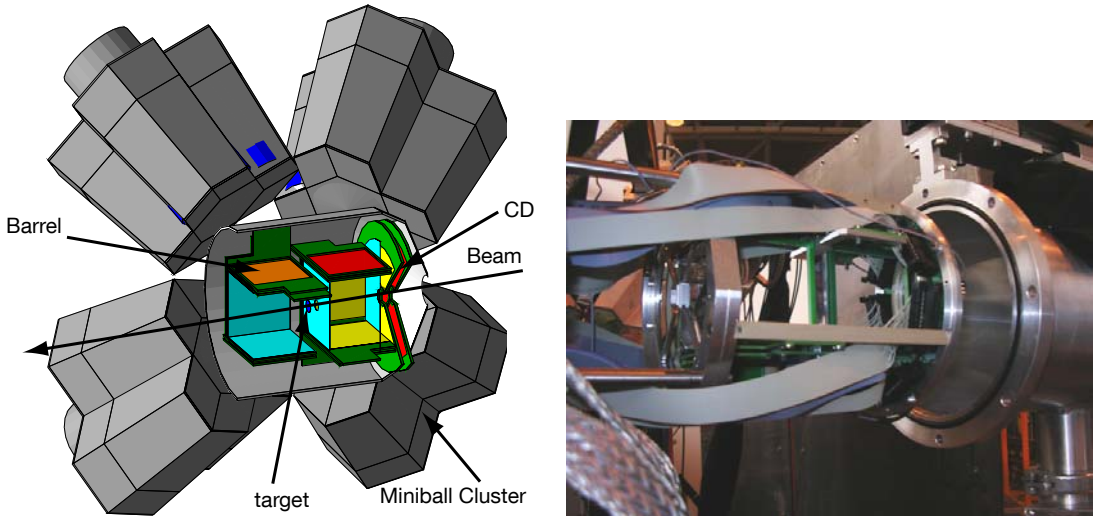

(a) (b)

Figure 3.4: Experimental T-REX setup at REX-ISOLDE. (a) Picture from the GEANT4 simulation of the experiment (see 3.7), (b) photo of the particle detector array. Beam is coming from the right.

modifications as compared to the 2007 experiments [BIL10] are shown in red, while the foils are light blue. Also the chamber itself was modified, instead of a spherical now a cylindrical chamber is used. It consists of two double sided segmented annular Silicon strip detector stacks (the CDs) and a barrel of 8 position sensitive Silicon strip detector stacks around the target with a total angular coverage of nearly 4π. Each detector stack contains two layers and acts thus as a $\Delta E - E$ telescope for particle identification by their specific energy loss. The ΔE detectors of the CD (thickness 500 μm) has 4 quadrants, each segmented in 16 annular rings on the front side and 24 sectors on the back. Thus ϑ_{lab} and φ_{lab} are measured for each hit. The E_{rest} detector also consists of 4 quadrants. Until today only a CD in backward direction is available. In the future the T-REX setup will be upgraded to have two CD detectors. The forward part with respect to the beam axis of the T-REX barrel consists of 140/1000 μm $\Delta E - E$ telescopes[1], while in backward direction only one detector layer of 500 μm was used in the 2007 experimental campaign [BIL10]. For the t(^{30}Mg,p)^{32}Mg reaction this was changed. In order to make particle identification possible also in backward direction, the same 140/1000 μm $\Delta E - E$ stacks as in forward direction were used. The ΔE detectors are segmented in 16 strips perpendicular to the beam direction. The position information along each strip is obtained by the charge division on a resistive layer. In order to reduce the large background from elastically scattered ^{30}Mg beam particles and Ti from the carrier material of the tritium target a system of foils to shield the detectors was installed. The optimized thickness and positions of the foils

[1]produced by Micron http://www.micronsemiconductor.co.uk/ (ΔE) and Canberra http://www.canberra.com/ (E)

were determined with the GEANT4 simulation (see section 3.7). The angular and energy resolution are both depending on the angle and the energy itself. The angular resolution depends strongly on the position of the hit on the detector, this is shown in Fig. 3.5. Assuming a beam spot diameter of 5 mm and using a pixel size on the

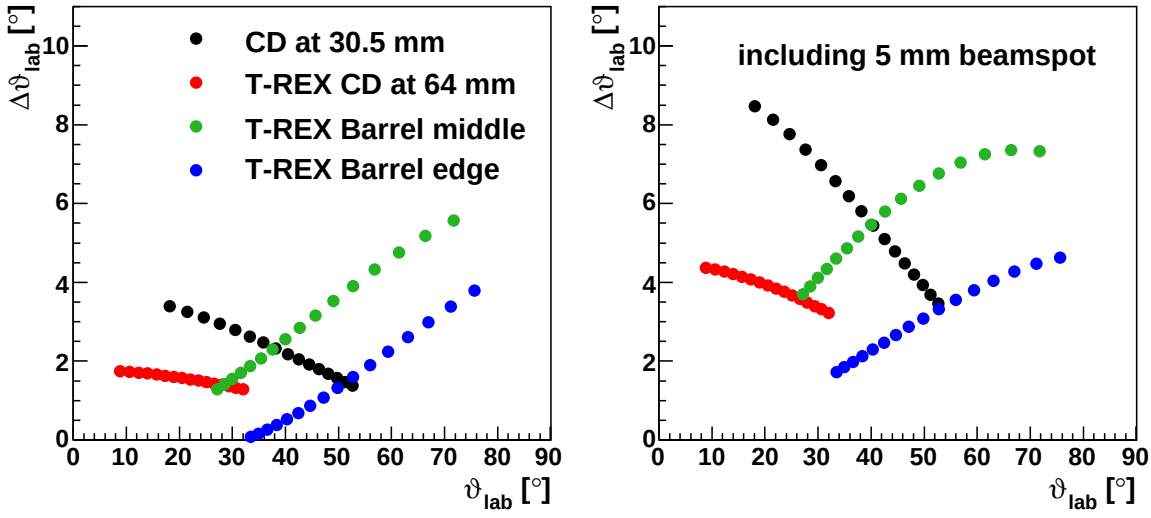

Figure 3.5: Angular resolution of the T-REX detector array. The resolution depends strongly on the position of the hit on the detector. The resolution is given by dividing the detector into pixels of 3.125×3.125 mm^2. For comparison the Coulomb excitation setup with a CD detector at 30.5 mm distance from the target is plotted as well.

detector of 3.125×3.125 mm^2 the resolution is between 2° and 6°. Fig. 3.4 shows an illustration of the setup taken from the simulation, to show the position of the detectors (yellow ΔE and orange/red E) and the foils (blue), and a photo of the actual setup used in 2008.

3.5 The MINIBALL detector array

The MINIBALL γ-spectrometer is a high resolution Germanium detector array [EBE01]. This high-efficiency spectrometer is built for experiments with radioactive ion beams at REX-ISOLDE. The MINIBALL-spectrometer with its high solid angle coverage and the good Doppler correction capability, resulting from the segmentation of the Ge crystals, is best suited for reactions with low γ-multiplicity. It consists of 24 individually encapsulated high purity Germanium detectors, which are electronically 6-fold segmented. These are arranged in 8 triple cluster cryostats around the target chamber. The solid angle coverage of the 8 clusters at a target-cluster distance of 11 cm is ≈ 60 % with a photopeak efficiency of about 7 % at $E_\gamma = 1.3$ MeV. The possibility to position the clusters individually in ϑ, φ, to vary their distance to the target, and to rotate

them around their axis allows to position them in a very close geometry. With the T-REX setup all clusters are slightly more oriented to backward angles compared to the Coulomb excitation setup.

3.6 Tritium loaded Titanium target

Two neutron (t,p) transfer reactions with radioactive beams are only possible with a radioactive target, in our case a tritium-loaded Ti foil[2]. The target is based on a 4.5×12 mm^2 strip metallic Ti foil. This foil has a thickness of 500 μg/cm^2 and it is loaded with an atomic ratio ^{3}H/Ti of 1.5 corresponding to a target thickness of 40 μg/cm^2 ^{3}H. A photo of the target is shown in Fig. 3.6(a). With an activity of less

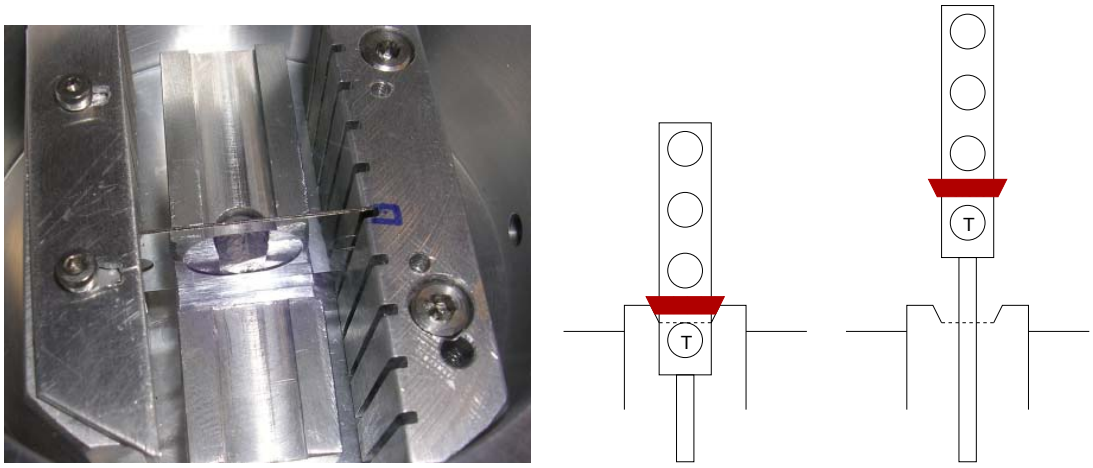

(a) (b)

Figure 3.6: a) Photo of the target, the target shows a small kink of about 1 mm height. b) Special target ladder for the use of the tritium target. For transportation and mounting the target is pulled down (left) and the sealing (red) creates a separate airtight enclosed volume for the tritium target.

than 10 GBq the target handling at ISOLDE was permitted following CERN Specification N° 4229RP20070405-GD-001 [OTT07]. In order to demonstrate the feasibility of using a tritium loaded Titanium target a stable beam experiment has been performed at HMI Berlin with an ^{40}Ar beam at 2.25 MeV/u and $6 \cdot 10^8$ part/s [MAH08]. The rate of scattered tritium nuclei was monitored during the whole run. No reduction indicating a loss of material in the target has been observed. Additionally, after the experiment the filter in front of the vacuum pumps exhibited no radioactivity. Similar targets, but loaded with deuterium instead of tritium, worked well and reliably in several experiments [MAH08] even at higher beam intensities than available at REX-ISOLDE. It was

[2]produced by EADS SODERN, 94451 Limeil-Brévannes Cedex, France

found by a RBS[3] experiment performed at the Maier-Leibnitz-Laboratory (Garching) that only at intensities of around 5 pnA, hence more than three orders of magnitude higher than intensities available at REX-ISOLDE, a loss of deuterium was observed. For safety reasons the target has to be sealed airtight for transportation and mounting. This was achieved by using a special target ladder which encloses the tritium target and at the same time allows the use of other targets for background and calibration measurements. This is shown in Fig. 3.6(b).

The use of Ti as a carrier material poses some challenges. First the beam energy has to be lowered to 1.83 MeV/u from the maximum REX-ISOLDE beam energy of 2.85 MeV/u as the fusion barrier for the reaction of ^{30}Mg on ^{48}Ti is $V_{\mathrm{fus}}^{\mathrm{cm}} = 35.6$ MeV which corresponds to a beam energy of $E = 59.6$ MeV or 1.99 MeV/u. The energy dependence of the fusion cross section for ^{30}Mg and ^{44}Ar is shown in Fig. 3.7. Compared to the transfer cross section (≈ 2 mb, see section 2.6) the cross section for fusion is by factors of hundred higher at the normal REX-ISOLDE beam energy of $2.8-2.9$ MeV/u. At the barrier the fusion cross section for ^{30}Mg on ^{48}Ti is still 60 mb. Although only few

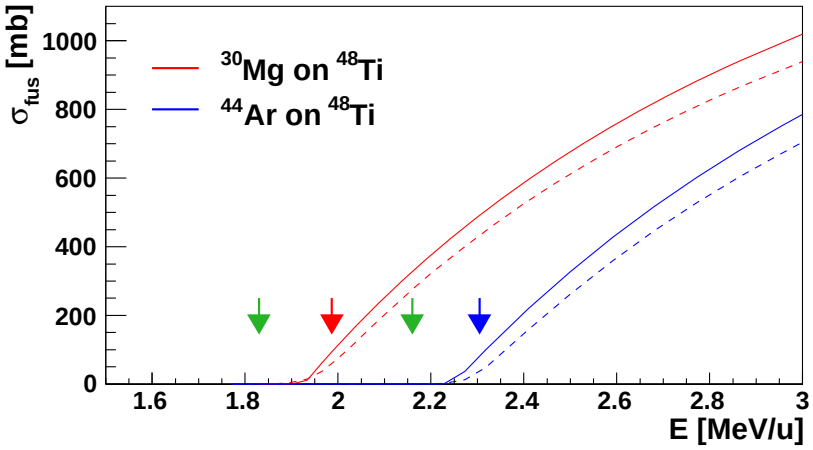

Figure 3.7: Fusion cross section for ^{30}Mg (red) and ^{44}Ar (blue) beams on ^{48}Ti. The solid lines are calculations using the PACE code [GAV80], the dashed lines are calculated with the CASCADE code [PÜH77]. The red and blue arrows indicate the Coulomb barrier for ^{30}Mg $+^{48}$Ti and ^{44}Ar $+^{48}$Ti, respectively. The green arrows indicate the beam energy actually used in the experiments.

reaction channels will have protons in the final state which would cause background in the spectra, the beam energy was chosen well below the Coulomb barrier as indicated by the green arrows in Fig. 3.7.

As a second difficulty, the beam ^{30}Mg is lighter than the target and can thus be scattered to backward laboratory angles. Since the Rutherford cross section in this angular region is comparable to the transfer cross section a shielding for heavy ejectiles has to be used.

[3]Rutherford backscattering spectrometry

The optimized geometry of the shielding foil has been determined using the GEANT4 simulation described in section 3.7.

3.7 Simulation of the setup and the reaction

In order to study the detector response and detection efficiency and to plan the current experiment as well as future experiments (see Chapter 6) the setup has been implemented in the GEANT4 simulation framework [AGO03] of the MINIBALL detector array [BOI09]. Details of the transfer simulation are given in [BIL10]. Here only the modifications relevant for the t(^{30}Mg,p)^{32}Mg experiment are described. A picture of the setup as included in the simulation is shown in Fig. 3.4(a).

For the simulation a number of input parameters are needed. For the geometry of the setup, the size and the position of the individual particle and γ-ray detectors as well as the dimensions of the foils are needed. Furthermore the resolution of the detectors has to be specified. There are several event generators implemented in the T-REX simulation package, including isotropic α, β, and γ sources as well as elastic and inelastic reactions. In order to simulate a reaction, the type of the reaction, elastic scattering, one or two neutron transfer, the reaction partners, the beam energy and the angular distribution in the center of mass system is needed. The output of the simulation is the same as the calibrated data tree (section 4.1) such that the further analysis of reconstructing particles and physics information is the same as for the data. This way the simulation can be used to test and develop the analysis as well as to determine the cut efficiency (see section 4.3). Furthermore simulations for the proposal of a new (t,p) experiment have been carried out and an event generator for Coulomb excitation experiments has been included (see Chapter 6).

Fig. 3.8 shows a simulation of the t(^{30}Mg,p) reaction. This simulation includes several states in ^{32}Mg which can be separated by their energy in laboratory backward angles. In forward direction the possibility to separate states depends on their energy difference as well as the beam energy and target thickness. Prior to the experiment the reaction has been studied in great detail in the framework of this thesis using the GEANT4 simulation package.

The use of Ti as a carrier material for the tritium target induces background in the detectors as events from elastic scattering with the Ti (or C in case of (d,p) reactions on CD_2 targets) from the target would overload the detectors. This is achieved by using a system of foils. In forward direction the aluminized Mylar foils are parallel to the detectors and have a thickness of 12 μm. Thus the effective thickness of the foil is larger for smaller ϑ_{lab} angles. As the energy of the heavy ejectiles and recoils of the elastic scattering reaction on Ti is larger for forward angles, this foil configuration stops them while at the same time allowing for low-energy tritons and protons from the reaction on ^{3}H to pass through the foil. In backward direction the situation is reverse. Here one needs a thicker foil for angles around 90° as compared to larger angles. Thus the foil in backward direction is perpendicular to the beam axis with a 8 mm diameter

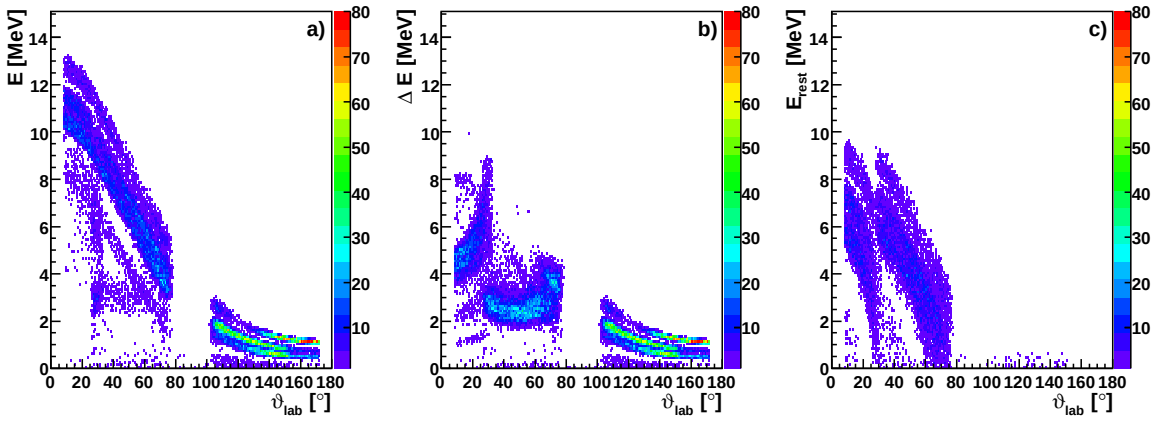

Figure 3.8: Simulation of the t(^{30}Mg,p) reaction. a) energy versus ϑ_{lab} spectrum for protons, b) ΔE and c) E_{rest} versus ϑ_{lab}.

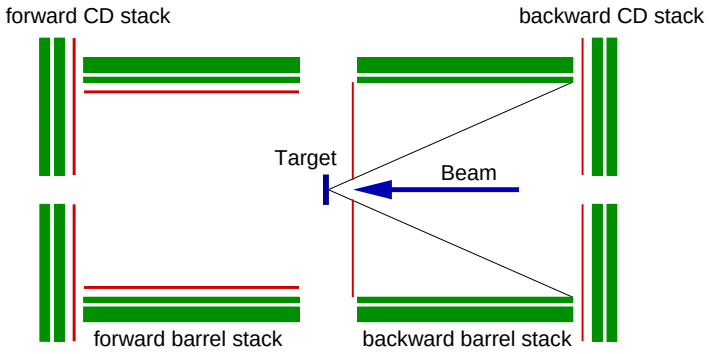

Figure 3.9: Foil system for the suppression of elastic scattering on Ti (red). The T-REX detectors including two CD stacks and the barrel are indicated in green. In forward direction the foils with a thickness of 12 μm are parallel to the detector, while in backward direction the foils are perpendicular to the beam axis. The size of the hole was adjusted to shield the whole detector as indicated by the thin black lines.

hole for the beam and only 2 μm thick. The effect of these foils on elastic scattered particle is shown in Fig. 3.10.

An important problem discovered in the first transfer experiment using T-REX was that a large amount of the beam is stopped inside the chamber. The β decay of the radioactive isotopes produced a large background not only in the γ spectra but also for the particle detection. With a Q-value of 6.961 MeV the energy of the β electrons becomes as large as the proton energy in backward direction. With the 500 μm thick detectors used in 2007 for the backward half of T-REX there was no possibility to decide whether an event detected there is an electron or a proton. In order to study the possibility to discriminate these events with a modified setup an event generator for β decay had to be included in the simulation. By using the same 140/1000 μm

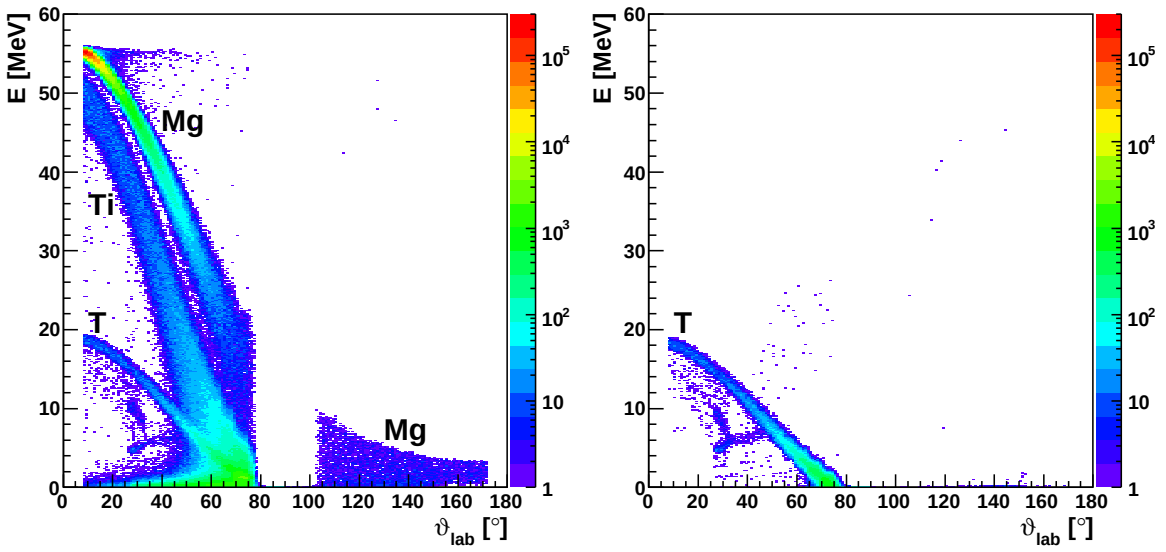

Figure 3.10: Suppression of elastic scattering on Ti with foils. The left panel shows a simulation of elastic scattering on tritium loaded Ti. A large amount of Ti and Mg particles is detected. The right hand side shows the same but with the foil system described in the text. Only elastic scattered tritons (T) are detected, while heavy ions are stopped in the foils.

thick $\Delta E - E$ detectors as in forward direction a suppression of electrons by a factor of 33 could be achieved, while at the same time the efficiency for proton detection is not affected. This is shown in Fig. 3.11. Electrons can go through the ΔE detector and induce a signal in the E detector, when gating on events with no energy in the E detector, most events lie below the trigger threshold of 200 keV.

3.8 Electronics and data acquisition

A scheme of the T-REX read-out electronics is displayed in Fig. 3.12. For the barrel the strip signals are amplified with MPR-64[4] preamplifiers and shaped with 8 STM-16 shapers. Their signals are then fed into 4 ADCs[5]. For the energy signals of ΔE and E detectors as well as for the CD E detectors combined MSI-8 preamplifier, shaper, and timing-filter amplifiers are used. The signals of the CD ΔE detector are processed using MUX-32 multiplexers. These units deliver 5 output signals, one combined trigger, energy, and analog position information for the channel with the first signal above threshold and the same for the second one. In case of more channels with a signal above threshold within 50 ns a reject signal is generated. Two quadrants of each side of the CD are combined in one MUX-32 unit. All energy signals are fed into 2 further

[4]All amplifiers for T-REX are from Mesytec http://www.mesytec.com/
[5]analog-to-digital converter produced by CAEN http://www.caen.it/nuclear

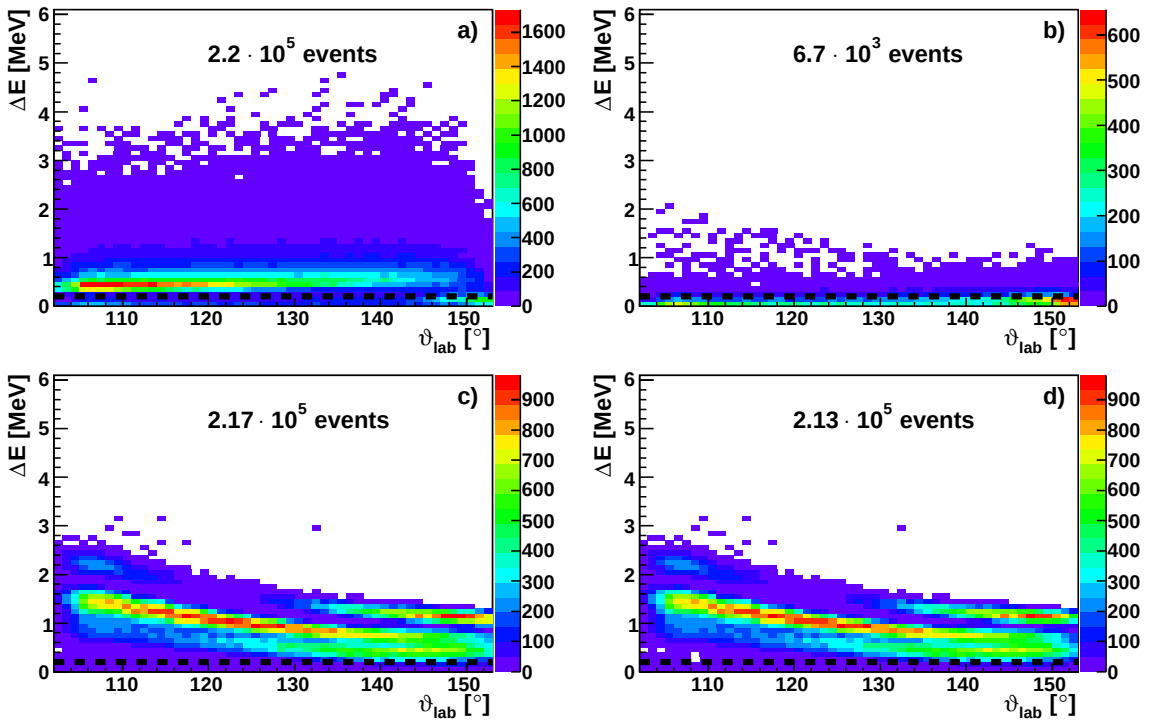

Figure 3.11: Simulation of electron suppression with the 140/1000 μm (b,d) $\Delta E - E$ detectors in the backward barrel instead of the 500 μm single layer detectors (a,c) used in 2007. Each panel shows the ΔE versus ϑ_{lab} for a simulation of $1 \cdot 10^6$ events. a) and b) Simulation of electrons only, a suppression factor of 33 can be achieved with a detection threshold of 200 keV (dashed line). c) and d) shows only transfer events, they are not affected as all protons are stopped in the ΔE layer.

ADCs while the timing signal are combined to two signals, one for all TOP (T) and LEFT (L) detectors and one for all BOTTOM (B) and RIGHT (R) detectors. These triggers are further processed and delayed to serve as a gate signal for 3 ADCs each. For the timing information of the particle signals these triggers are also fed into a DGF module each for time-stamping (not shown). The energy data of the 168 channels of cores and segment of the MINIBALL detector are recorded by one DGF channel each. For the time-stamp signal of the crystal, the core time is used. A detailed description of the logic signals and the MINIBALL electronics which are the same as for Coulomb excitation experiments can be found in [WAR08].

For the data acquisition and the analysis the timing of the beam at REX-ISOLDE is very important. With every proton pulse impinging on the ISOLDE target the T1 pulse signal is generated. From that time on the produced atoms will diffuse out of the target. The second important time signal is the EBIS pulse, this is created when the ions are injected into the linac. The EBIS pulse is used to start the so called ON-BEAM window which lasts for 800 μs. Only during that time accelerated ions can reach the

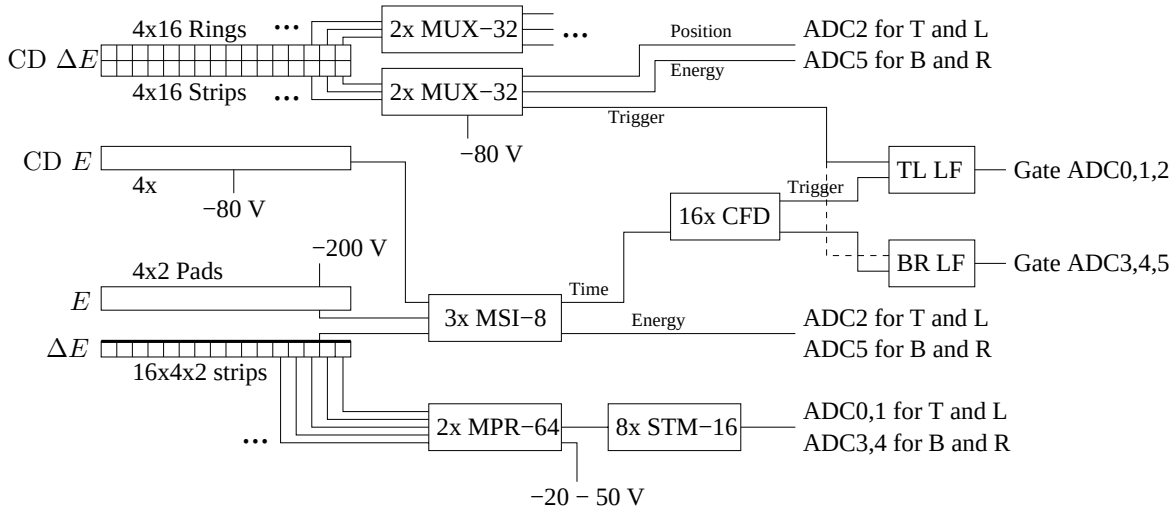

Figure 3.12: Electronics setup for T-REX, for details see text.

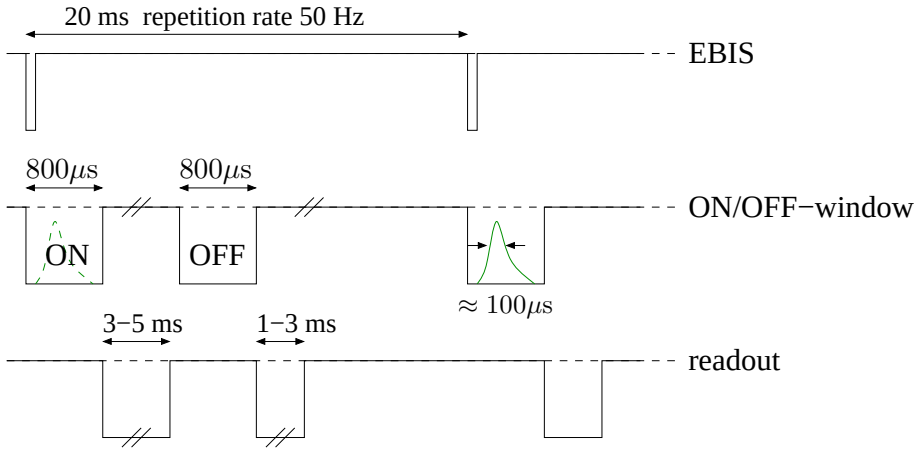

Figure 3.13: Time structure of REX-ISOLDE beams and the readout. With the EBIS pulse the ON-BEAM window is started, this lasts for 800 μs. After the readout and storage of the data an OFF-BEAM window for background subtraction is created.

setup and data is recorded. All physical events within this window are buffered in the ADCs. With the end of the ON-BEAM window the readout with the MARaBOU Data Acquisition software [LUT03] is started. The readout and storage of the data takes a few ms. When the readout is completed, the OFF-BEAM window is opened. Here no beam is present and only events from β decay and natural background can occur. The data recorded in the OFF-BEAM window is used for background subtraction. The special structure of multievent buffering of one full spill allows to minimize the deadtime of the data acquisition system.

4 Data analysis

In order to extract physical properties of the t(^{30}Mg,p)^{32}Mg reaction and to allow for a detailed comparison with theory (see chapter 5) a series of different absolute and relative calibrations have to be performed. First of all, the ADC and DGF values recorded by the MARaBOU Data Acquisition software [LUT03] have to be calibrated to obtain the energy, position, and time of each event detected in the T-REX and MINIBALL detectors. Then the particles are identified by their characteristic energy loss in the $\Delta E - E$ detector stacks and the energy and angle at the emission point can be reconstructed. Also, the efficiency for the detection of a photo-peak event in the MINIBALL detector as well as the particle detection and identification efficiency have to be analyzed. Finally, the angular distributions can be determined.

4.1 Calibration procedure

For the offline analysis first the raw data have to be unpacked from the MED data format [LUT05] and converted to ROOT files [ROO07]. The unpacking code used in this work is based on the Coulomb excitation analysis [NIE05a] and adapted to the special requirements of transfer experiments [BIL10]. Due to the special readout, each event in the MED format contains the physical events of a whole ON- or OFF-BEAM window. In order to separate the physical events (event building) first the time-stamps for the particle events are matched with the ADC data. Then a coincidence window of 1 μs between ADC and DGF events is used to correlate particles and γ-rays. This window is much wider than the actual coincidence window used in the analysis (see section 4.1.3) so these events still contain random coincidences. For the analysis only those events are considered which lie within 125-200 μs after the EBIS pulse. During this time the beam pulse arrives at the MINIBALL setup (see Fig. 3.13). All other events can be used for background subtraction. After the unpacking and event building the data have to be calibrated.

4.1.1 Calibration of the MINIBALL array

The HPGe detector array MINIBALL has been calibrated using radioactive ^{152}Eu and ^{60}Co sources. Both sources show various γ-transitions between 100 and 1400 keV which can be used for energy calibration. The resolution of this detector amounts to $\approx$ 3.0 keV (FWHM) for the 1333 keV transition for a core and 3.4 keV for the segments. For the Germanium detectors not only the energy signals had to be calibrated, but also

the photo-peak efficiency $\varepsilon_{\mathrm{ph}}$ has to be known. In order to increase the photo-peak efficiency cluster addback is performed. Due to the large probability of a Compton scattering event in one crystal and absorption of the scattered γ-ray in another crystal close by, adding these two energies increases the photo-peak efficiency but worsens the resolution. If two hits within one cluster have occurred within an certain time window the two energies are added and the position of the higher energy hit is assumed to be the first interaction point, which is used for the Doppler correction. Since the timing signal for low-energy γ-rays is slower than for higher energies (see section 4.1.3 and Fig. 4.5) the addback time window is energy dependent.

In order to determine the absolute photo-peak efficiencies, two approaches have been used. With a known source activity and measuring time the absolute photo-peak effi-

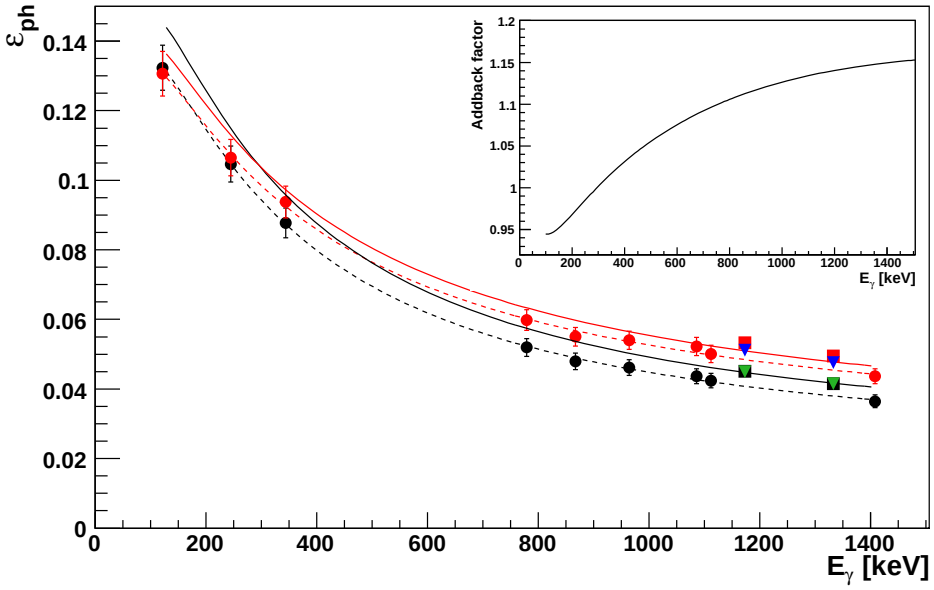

Figure 4.1: Efficiency calibration of the MINIBALL γ-ray spectrometer. The absolute photo-peak efficiency is shown for the total array determined with the ^{152}Eu (black circles) and ^{60}Co (black rectangles) sources. The shape of the efficiency curve has been determined with the ^{152}Eu source (dashed lines). For the ^{60}Co source the sum peak method can also be used (green triangles). The efficiency curve has been scaled to these points (solid line). The red and blue data points and lines show the same with the cluster addback method. The inset shows the addback factor, the ratio of the efficiency with addback versus normal detection as a function of energy.

ciency can be determined. However, due to the special data acquisition with ON- and OFF beam windows, the measuring time at the MINIBALL setup is only approximately known. The second method is the so called sum peak method which is independent of the deadtime of the data acquisition and the source activity. ^{60}Co emits two coincident γ-ray transitions (1173 and 1333 keV). If both γ-rays are detected in the same crystal

the spectrum shows a peak at 2506 keV. The sum of the two γ-ray energies can be used to determine the photo-peak efficiency. This approach is described in [BRI63]. An angular correlation factor $W(\theta \approx 0)$ between the two consecutive γ-rays has to be taken into account. For the E2 cascade of ^{60}Co the correlation factor amounts to 1.1 [KIM03]. Fig. 4.1 shows a comparison of the two approaches. The shape of the efficiency curve (Eq. 4.1) has been determined with the ^{152}Eu source.

$$\varepsilon_{\mathrm{ph}} = \exp\left[a_0 + a_1 \log E_\gamma + a_2(\log E_\gamma)^2 + a_2(\log E_\gamma)^3\right] \tag{4.1}$$

For ^{60}Co both approaches can be used, the results are in excellent agreement (green and black points at 1173 and 1333 keV in Fig. 4.1). The discrepancy in absolute efficiency determined with ^{152}Eu and ^{60}Co sources can be explained by the smaller activity of the Co source which reduces the dead-time (24.4 kBq and 2.1 kBq). Thus the efficiency curve has been scaled to the Co measurement. The efficiency with Cluster addback is shown by the red line in Fig. 4.1. The ratio of the efficiency with addback versus normal detection as a function of energy is the addback factor. It is smaller than 1 for low energies (below 400 keV) due to incorrect summing. For larger energies the efficiency can be increased by up to 15 % using the Cluster addback method.

The recoiling nucleus emits its γ-radiation with the transition energy E_0 in its rest frame. In the laboratory frame the measured energy E_{lab} is Doppler-shifted depending on the angle α between the photon and the trajectory of the emitting nucleus. Since the velocities of the ejectile at REX-ISOLDE can become quite large ($\beta \approx 7$ %) the measured γ-ray energy has to be corrected:

$$E_0 = \gamma E_{\mathrm{lab}}(1 - \beta \cos\alpha). \tag{4.2}$$

This requires a precise knowledge of the angle α. The position of the MINIBALL crystals with respect to the beam axis can be determined with the one neutron transfer reaction d(^{22}Ne,p)^{23}Ne using a stable ^{22}Ne beam at 2.85 MeV/u. This reaction (see also section 5.1) populates the first excited state in ^{23}Ne at 1017 keV. Assuming that the beam is not deflected in the reaction (the maximum scattering angle of ^{23}Ne is 4.7°) the angle ϑ_{lab} of the MINIBALL detector can be determined from the shift of the detected energy in the segment or core and the known velocity of the beam. Due to the limited statistics for this reaction, the angle φ_{lab} of the detectors could not be determined. The effect of the correction on the 1017 keV line in ^{23}Ne using either the crystal angles or the segment angles is shown in Fig. 4.2. However, the φ_{lab} angles of the γ-rays are unknown, and the assumption that the ejectile ^{23}Ne is scattered to 0° is not really valid. Also, even with the segmentation of the MINIBALL crystals the opening angle of a segment is still 7.7°. Another source of uncertainty is the velocity of the beam, which looses energy when going through the target. The resulting velocity spread is about 5 % for the ^{22}Ne test measurement (2 % for ^{30}Mg with 1.83 MeV/u on the Ti/tritium target). The line width (FWHM) of the 1017 keV transition in ^{23}Ne due to the opening angles and the velocity spread can be estimated to be 20.6 keV for crystal based and 14.3 keV for segment based Doppler correction. The measured resolution of the γ-ray transition after Doppler correction is 18.2 keV for segment based

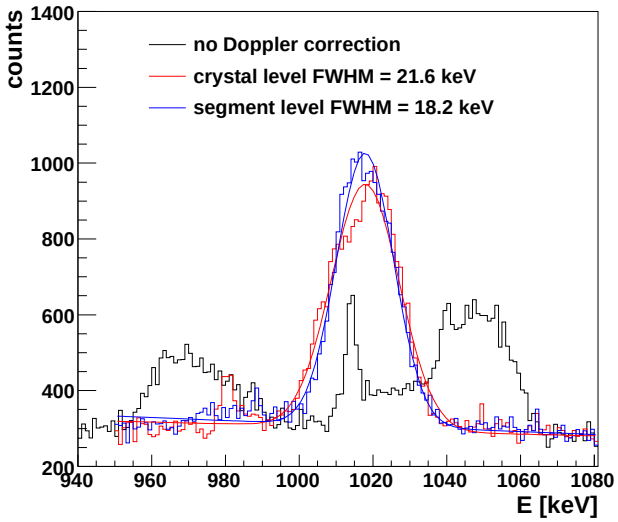

Figure 4.2: Doppler correction of the 1017 keV line in ^{23}Ne. The two broad peaks in the uncorrected spectrum correspond to the forward and backward hemisphere of the MINIBALL detector. The resolution of the line after Doppler correctionis determined by the unknown angle φ_{lab} of the γ-ray as well as the velocity β.

Doppler correction which is larger than the estimate above. The reason may lie in the fact that in the experiment described here some of the segments were broken. As a result the determined first interaction point of the γ-ray in the Germanium crystal can be wrong if a broken segment was hit. For the crystal Doppler correction the estimated and measured values of the resolution agree.

4.1.2 Calibration for the particle detectors

In order to determine the position of a particle hit in the barrel strip detectors, the strip signal has to be calibrated. The position along the strip is proportional to the strip signal divided by the total energy deposited in the detector. However, the energy signal of the backside of the ΔE detector depends itself on the position x along the strip. Since only one side of the strip is read and the other one is coupled to ground, the strip signal is smaller for events further away from the readout side. This is shown in Fig. 4.3 a) for one strip. Here the ADC value (channel) of the backside of the detector is shown versus the uncalibrated position along the strip. It can clearly be seen that the ADC value is larger for positions close to the readout of the strip ($x_{\mathrm{nc}} \approx 0.55$). This value also corresponds to the correct energy for the strip, since in this case the resistive layer on the strip and the capacitive coupling to ground on the other side do not play a role. First of all, the position x_{nc} is calibrated. For convenience x ranges from 0 to 1, this is later changed to real positions ranging from -25 to 25 mm along

the strip. Then the backside energy E can be corrected depending on the position $x \in [0, 1]$ as

$$E_{\text{corr}} = \frac{E(x)}{a(1-x)+1} \text{ with } a = \left(\frac{E(x)}{E(x=1)} - 1\right) \frac{1}{1-x}. \tag{4.3}$$

This corrected but still uncalibrated backside energy is used to recalculate the position. Afterwards the energy can be calibrated as shown below. Fig. 4.3 b) shows the energy and position calibrated spectrum of this strip. All ΔE detectors have been calibrated

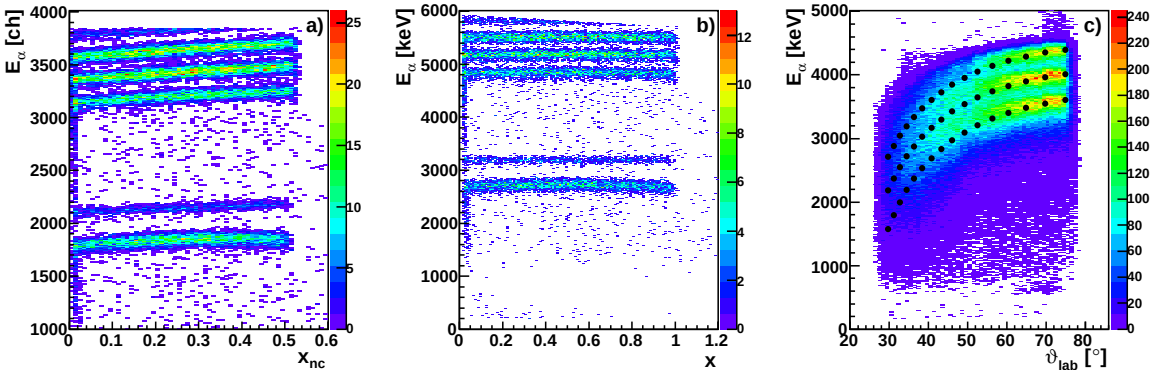

Figure 4.3: a) Energy signal for one strip of the backside of a ΔE detector versus the uncalibrated position along the strip. b) same as a) but calibrated, now the energy does not depend on the position anymore. c) Energy versus ϑ_{lab} for the forward barrel. The dots show the calculated α energy after going through a 12 μm Mylar foil.

with a mixed α source. It consists of four α emitters, ^{148}Gd, ^{239}Pu, ^{241}Am and ^{244}Cm, with α energies at 3.18, 5.16, 5.49 and 5.81 MeV. Since foils are mounted in front of the detectors (see section 3.7) these energies cannot be used for calibration, rather the energy loss of α particles in the foil has to be taken into account. In backward direction the foil is perpendicular to the beam axis and has a hole to let the beam pass. However, the active surface of the α source is bigger than this hole. Therefore some of the particles can hit the detectors without going through the foil. This can be seen in Fig. 4.3 b) for the ^{148}Gd line at 3.18 MeV. The spectrum shows two lines, at 3.18 MeV for particles which miss the foil and at 2.75 MeV corresponding to the energy loss in 2 μm Mylar foil. For the higher lying lines the energy loss in the foil is accidentally the same as the energy difference of the three lines, only the highest α line with full energy can be partially seen in Fig. 4.3. The energy loss is even bigger in forward direction where the foil is parallel to the detectors and 12 μm thick. A calibrated spectrum of the forward direction in comparison with the calculated remaining energy after going through a foil with thickness $(\sin\vartheta_{\text{lab}})^{-1} \cdot 12$ μm is shown in Fig. 4.3 c). The energy resolution of the ΔE detectors has been measured to be $\approx$ 140 keV for backward detectors and $\approx$ 230 keV (FWHM) for forward detectors with an α source and foils mounted in front of the detectors. This is, however, not the resolution to be

expected for reactions, as energy loss in target and foils are different for lighter ions. Also the α particles only penetrate the very first μms of the detector and thus give rise to very different signals than light ions. For the calibration of the CD detectors first the strip or ring number has to be determined from the analog hit information of the multiplexer (see section 3.8). Then each strip or ring can be calibrated individually.

The calibration of the E detectors is not so straight forward, since these are shielded by the ΔE detectors and cannot be hit by α particles. One method used in this work is the analysis of elastic scattered deuterons from the ^{22}Ne(d,p) test experiment. Once position and energy loss in the ΔE detector are known, the remaining energy of a deuteron can be calculated and used for calibration. The second method used here is Compton scattering of γ-rays in the E detector. When gating on coincidences

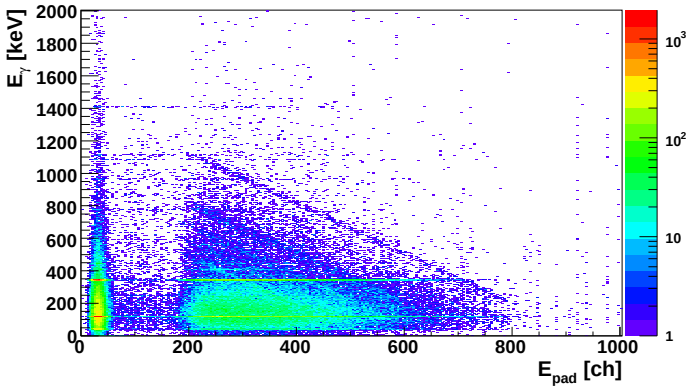

Figure 4.4: Energy detected in MINIBALL versus uncalibrated energy in one of the E detectors.

between events in the MINIBALL detector and the E detector, as shown in Fig. 4.4 the Compton scattering of the 1408 keV γ-ray transition of the ^{152}Eu source can be seen on a line going from the full energy in the Germanium detector and no energy in the E detector down to full energy in the E detector (Compton edge for a 1408 keV γ-ray is 1192 keV). This correlation has been used to calibrate the E detector in the low-energy range ($0-1000$ keV). Both methods have been combined in order to obtain a calibration curve for the full range of the detector ($0-15$ MeV).

4.1.3 Calibration of the timing signals

The time difference of two detector responses belonging to the same event can be obtained by subtracting their time signals given by the DGF time stamp modules. Fig. 4.5 a) shows the γ-ray energy versus the time difference between a γ-ray detected in a Germanium crystal and a proton from the ^{22}Ne(d,p) reaction hitting one of the Silicon detectors. The time signal for low-energy γrays is slower than for higher energies since here the timing of the constant fraction discriminator still depends on the pulse height (uncompensated "walk" effect). Also the two trigger groups for TOP/LEFT and

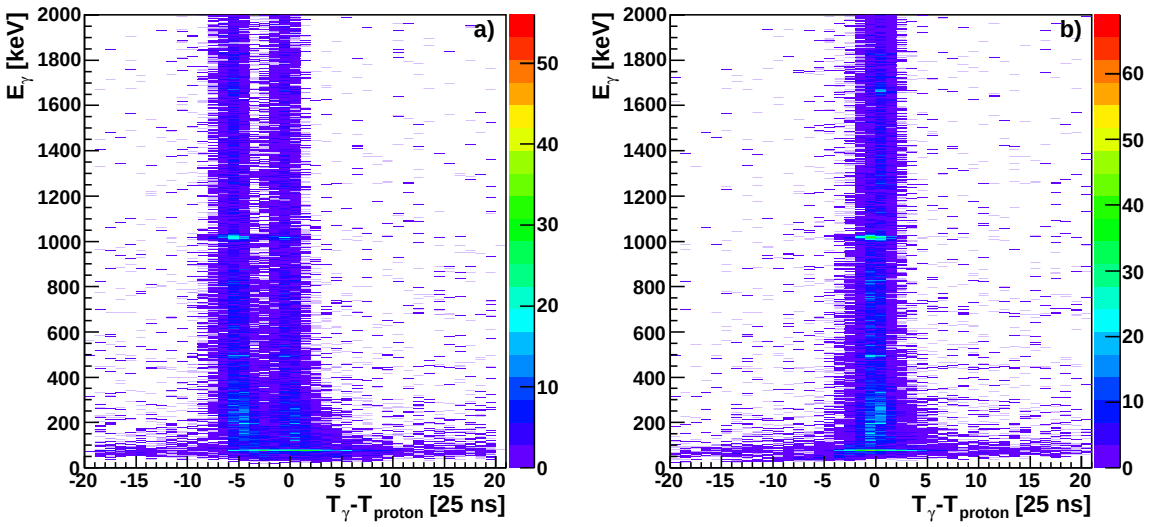

Figure 4.5: a) Uncorrected spectrum of γ-ray energy versus time difference between γ signal and proton signal. b) same as a) but corrected.

BOTTOM/RIGHT have different timing properties. The "walk" effect was corrected in the off-line analysis by fitting an exponential function to the time difference. This was done for each particle trigger group separately. Fig. 4.5 b) shows the corrected spectrum.

4.2 Identification and reconstruction of particles

Once all detectors are calibrated in energy and position measurement, physical particles can be identified and their trajectories are reconstructed. In the forward barrel most of the hits have a characteristic $\Delta E - E$ signature in the Silicon telescope. The identification can be done in two ways. The first method is to apply separate identification cuts for each detector and each strip. A particle is identified as a proton, for example, if it lies in the $\Delta E - E$ plot below the maximum calculated energy loss (i.e. largest effective thickness of the ΔE detector for the respective strip) and above the respective minimum. The positions on the detector strips for minimum and maximum energy loss are also shown in Fig. 4.6 b). Events which are still unidentified, i.e. they lie between the cut of maximum energy loss for protons and minimum for deuterons are still counted as protons if they are not further outside of the cut than the detector resolution.

Due to the limited statistics in one strip for the (t,p) reaction a second method is employed to visualize the identification. Assuming that the energy loss is proportional to the path length in the detector, the energy loss in the ΔE detector can be corrected. From the position of the particle the energy loss for a path perpendicular to the detector surface can be calculated $\Delta E^{\mathrm{cor}} = \cos\alpha \cdot \Delta E$. α is the angle between the normal vector

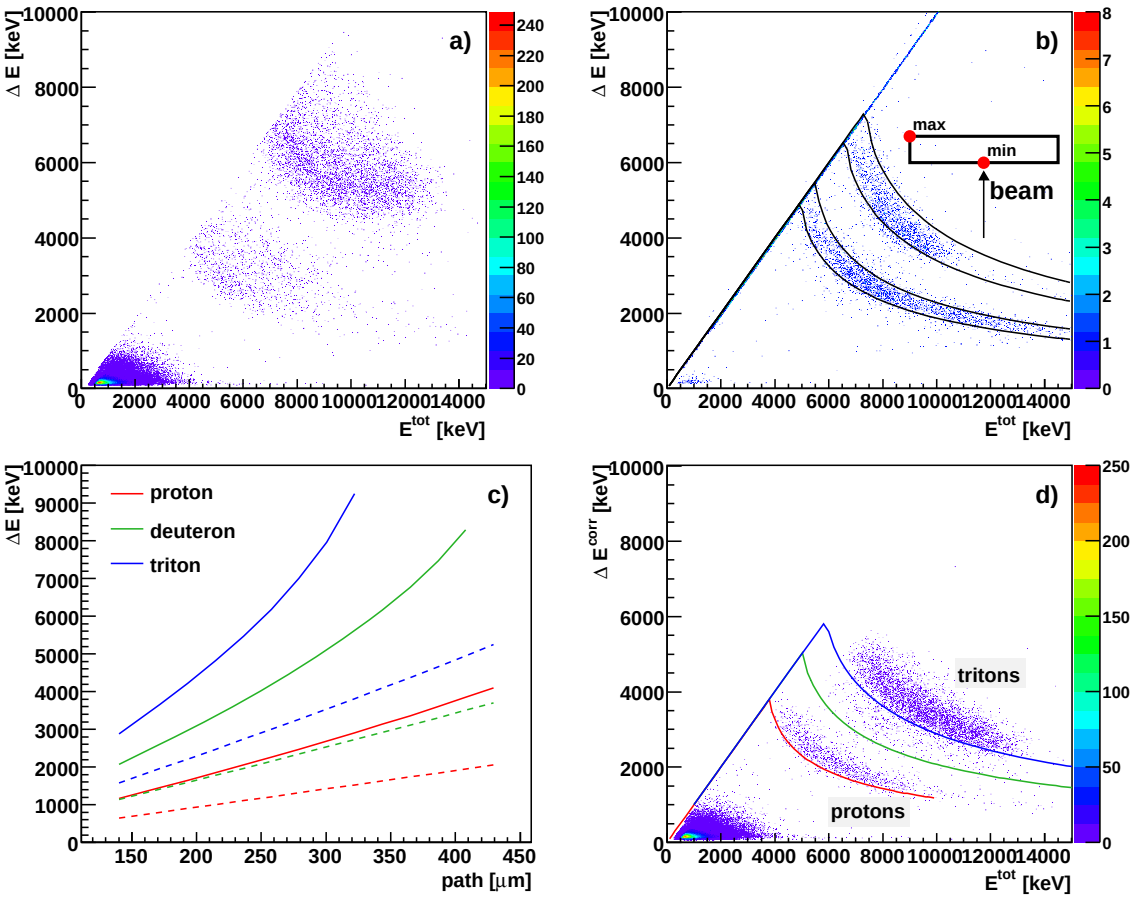

Figure 4.6: a) $\Delta E - E$ spectrum for all particles detected during the ^{30}Mg(t,p) run. b) Particle identification spectrum for the ^{22}Ne data for just one strip together with the identification cut. The inset shown the positions on the detector strips for minimum and maximum energy loss. c) Dependence of the energy loss in Silicon on the path length. The solid lines are calculated for 10 MeV total energy, the dashed for 20 MeV. The assumption of a linear dependence is approximately fulfilled. d) same as a) but corrected $\Delta E - E$ spectrum together with identification lines.

on the detector surface and the particle direction. This is shown in Fig. 4.6 c) and d) for the ^{30}Mg(t,p) reaction. The events lie above the calculated energy loss in 140 μm since the assumption that the energy loss is proportional to the path length is not fulfilled exactly (Fig. 4.6 c)).

Stopped particles are identified by kinematical cuts in the ϑ_{lab} - E plane. The cuts for the t(^{30}Mg,p) reaction are shown in Fig. 4.7 together with all stopped particles in the forward barrel. Here the cuts may overlap. Thus, it is crucial to determine the efficiency and purity of such cuts by a GEANT4 simulation (see section 4.3).

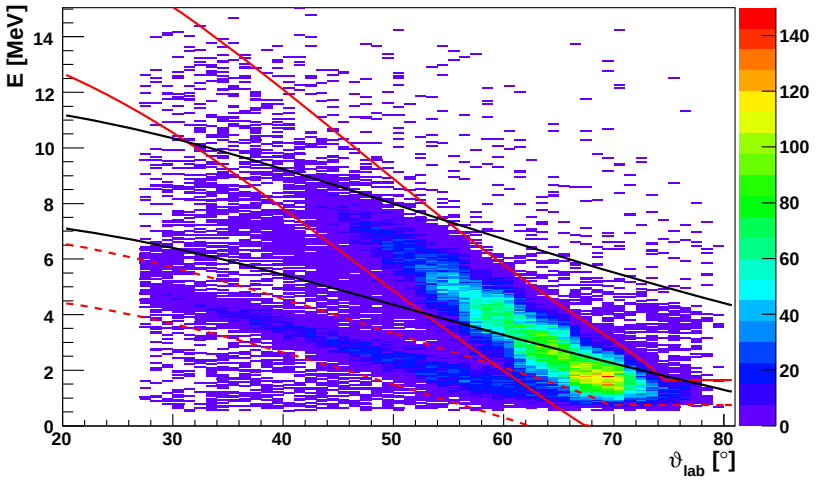

Figure 4.7: Identification cuts for stopped particles. The red lines show the cuts for elastic scattered tritons (solid lines) and protons (dashed), while the black lines mark the identification area for protons from transfer reactions.

Once the particle is identified and its emission angle is known the energy losses in the protection foils of the detector and the target have to be corrected. Knowing the geometry and the particle direction as well as its energy deposition in the Silicon detectors the particle energy at the emission point can be reconstructed. This is done by calculating the range of the particle in Mylar or the target material from the total detected energy with the IRMA code [ERN84]. Afterwards the corresponding position dependent thickness of the material is added, and the energy is recalculated from the obtained range. This resulting energy is then used in the further analysis.

4.2.1 Determination of the target position

As seen from Fig. 3.6 the tritium target is not flat, it shows a kink of about 1 mm, which corresponds to a shift of the target position in beam direction with respect to the center of T-REX. Also with the Polyethylene target used for the d(^{22}Ne,p)^{23}Ne test measurement the position in beam direction was not well determined. However, from the data the target position can be determined more precisely. The energy versus ϑ_{lab} spectrum is compared with calculated kinematics for different shifts in z direction of the target. Thus, the z shift of the target can be obtained. An example of this procedure for the ^{22}Ne(d,d) reaction is shown in Fig. 4.8. The shift z_{shift} amounts to 2.3 mm in beam direction for the deuterated PE target data and 1.1 mm for the tritium target, which is comparable with the visible kink in the target Fig. 3.6. The target ladder used for the tritium target is better guided, thus an additional shift due to misalignment of the ladder is small, in contrast to the ladder used for the PE targets. The correct target shift can easily be verified, since in this case the reconstructed beam energy and excitation energies of the ejectiles do not depend anymore on the laboratory

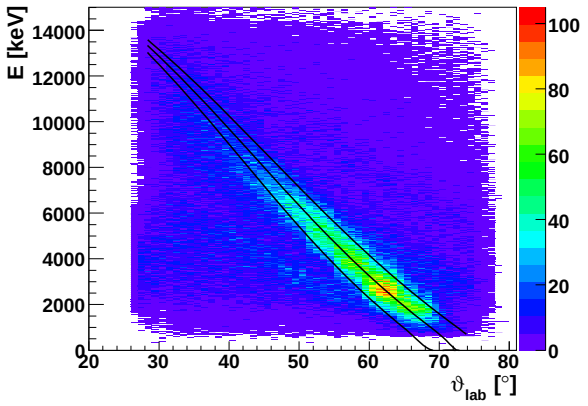

Figure 4.8: In order to determine the target position the energy versus ϑ_{lab} spectrum is compared with calculated kinematics assuming different target positions. The three lines show from top to bottom, no shift in the target position, target shifted by 2.3 mm in beam direction and a shift of 5.0 mm in beam direction.

angle. By comparing the spectra of the four individual quadrants of T-REX the shift perpendicular to the beam axis can be determined. In the experiment described here no shift in x or y direction has been observed. For the experimental campaign in 2009 additional guiding rails for the target ladder have been constructed to fix the z position of the targets.

4.2.2 Excitation energies

Once the light particle emitted in the reaction has been identified, the excitation energy of the heavy ejectile can be reconstructed from the energy and position of the recoil. From the energy and angle of the proton its momentum can be calculated and transformed into the center of mass system (cm), where the momenta of ejectile (e) and recoil (r) are of equal size but opposite direction. The total energy in the center of mass system E^{cm} is the sum of the center of mass energies of recoil and ejectile ($E_{\mathrm{e}}^{\mathrm{cm}}$ and $E_{\mathrm{p}}^{\mathrm{cm}}$). It is determined by the masses of projectile (p) and target (t) nucleus and the beam energy E^{beam}. The excitation energy can then be calculated from the mass of the ejectile M_{e} and the known ground state mass M_{e}^{0}:

$$\begin{aligned} p_{\mathrm{e}}^{\mathrm{cm}} &= -p_{\mathrm{r}}^{\mathrm{cm}} \\ E^{\mathrm{cm}} &= E_{\mathrm{e}}^{\mathrm{cm}} + E_{\mathrm{p}}^{\mathrm{cm}} \\ &= \sqrt{M_{\mathrm{p}}^2 + M_{\mathrm{t}}^2 + 2M_{\mathrm{t}} \cdot (M_{\mathrm{p}} + E^{\mathrm{beam}})} \\ E_{\mathrm{e}}^{\mathrm{exc}} &= M_{\mathrm{e}} - M_{\mathrm{e}}^{0} \\ &= \sqrt{(E_{\mathrm{e}}^{\mathrm{cm}})^2 + (p_{\mathrm{e}}^{\mathrm{cm}})^2} - M_{\mathrm{e}}^{0} \end{aligned} \tag{4.4}$$

The resolution in excitation energy is determined by the angular and energy resolution, as well as the energy and angle straggling in the foils and the target.

4.3 Particle detection efficiency and solid angle correction

In order to determine the angular distribution of protons the particle detection efficiency and the conversion from counts/dϑ_{lab} to dσ/dΩ have to be determined. This is done in the following two steps.

4.3.1 Calculation of the solid angle of T-REX

For the determination of the conversion factor from counts to cross section the solid angle dΩ has to be calculated in Cartesian coordinates for the barrel and in cylindrical coordinates for the annular detector. The result has to be converted back to spherical coordinates to be applied to ϑ_{lab}. For the barrel the solid angle element of a pixel on the detector ranging from $x = x_0$ to x_1 and from $z = z_0$ to z_1 (y is kept constant, this is the distance of the barrel detector to the beam axis, $y = 29$ mm) is:

$$\begin{aligned}\iint_{\mathrm{pixel}} \sin\vartheta \mathrm{d}\vartheta \mathrm{d}\varphi &= \int_{z_0}^{z_1}\int_{x_0}^{x_1} \frac{y}{(x^2+y^2+z^2)^{3/2}} \mathrm{d}x\mathrm{d}z \\ &= \left[\left[\arctan\left(\frac{x\cdot z}{y\sqrt{x^2+y^2+z^2}}\right)\right]_{x_0}^{x_1}\right]_{z_0}^{z_1}\end{aligned}$$

For the annular detector a pixel extending from radius $\rho = \rho_0$ to ρ_1 and from $\varphi = \varphi_0$ to φ_1 the solid angle element is (z is the distance from target to detector $z = 64$ mm $+z_{\mathrm{shift}}$):

$$\begin{aligned}\iint_{\mathrm{pixel}} \sin\vartheta \mathrm{d}\vartheta \mathrm{d}\varphi &= \int_{\rho_0}^{\rho_1}\int_{\varphi_0}^{\varphi_1} \frac{\rho\cdot z}{(\rho^2+z^2)^{3/2}} \mathrm{d}\rho\mathrm{d}\varphi \\ &= \left(\frac{1}{\sqrt{\rho_0^2+z^2}} - \frac{1}{\sqrt{\rho_1^2+z^2}}\right) z(\varphi_1-\varphi_0)\end{aligned}$$

All these integrals are then summed up to give the solid angle as a function of ϑ_{lab}. In this way also broken strips of the detectors and the effect of the shifted target position are taken into account. This is shown in Fig. 4.9. The dips in the solid angle are due to broken strips and around 150° due to the partial overlap of barrel and CD detectors. The angular distributions corrected with the effective solid angle directly give the cross section dσ/dΩ. The normalization to mb/sr is done by analyzing the elastic scattering. This is described in the next chapter.

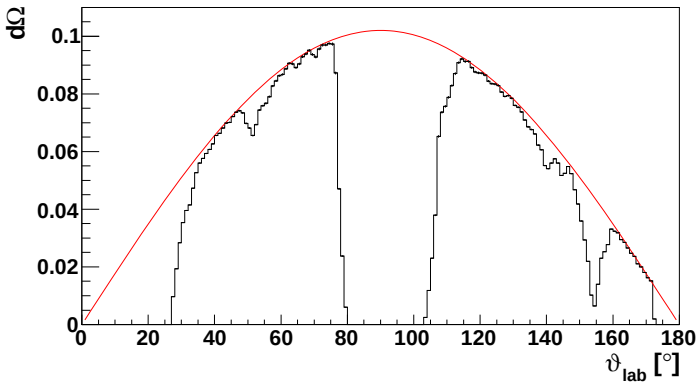

Figure 4.9: Effective solid angle covered by T-REX in comparison with dσ for a 4π coverage. The dips in the solid angle arise from broken strips of the detector.

4.3.2 T-REX particle detection efficiency

The particle detection efficiency is determined with the simulation. The emission of an isotropic distribution in the laboratory system is simulated. Then the ϑ_{lab} distribution of the desired particle species and excitation energy is divided by the ϑ_{lab} distribution of all detected particles. This way the trigger thresholds and the acceptance of the identification cuts are taken into account. In the calculation of the effective solid angle broken strips are already taken into account. The result directly gives the efficiency for detecting the recoil of a specific reaction. Fig. 4.10 shows the particle identification correction factor for the t(^{30}Mg,p)^{32}Mg reaction. The correction factors for tritons

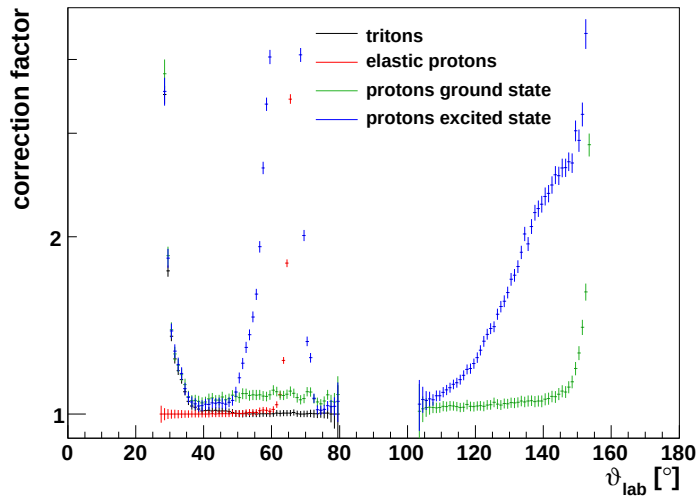

Figure 4.10: Particle identification efficiency for elastic scattered and reaction ejectiles.

and protons from transfer reactions rise for ϑ_{lab} angles below 40° as here the particles can go through the ΔE detector, but miss the E detector. Elastic scattered protons

are stopped in the ΔE detector over the whole angular range leading to a constant efficiency. The rise around 60° for both elastic scattered and transfer protons is due to the overlapping identification cuts (see also Fig. 4.7). For backward laboratory angles the efficiency depends on the kinematics of the reaction and on the detection threshold as the energy of protons gets very small. In the last step the angular distributions are transformed into the center of mass system.

With the analysis steps described in this chapter the angular distributions for transfer reactions as well as elastic scattering can be determined, which are discussed in the next chapter.

5 Experimental results and discussion

In the following chapter the results of the t(^{30}Mg,p)^{32}Mg two neutron transfer reaction experiment are presented. The main goal of the experiment was to find and characterize the excited 0^+ state in ^{32}Mg. The first section summarizes the results from a test measurement with a stable ^{22}Ne beam. In the following section the results for the excitation energies and angular distributions of states in ^{32}Mg are presented which lead to the discovery of the 0^+_2 state in ^{32}Mg. In the last section of this chapter the results for both 0^+ states are compared to theoretical calculations and an interpretation of the measured cross sections is presented.

5.1 Results from the test measurement d(^{22}Ne,p)^{23}Ne

In order to test the T-REX/MINIBALL setup and the analysis described in the previous chapter the d(^{22}Ne,p)^{23}Ne reaction with a stable ^{22}Ne beam at 2.85 MeV/u has been measured. ^{22}Ne is used as a buffer gas in the EBIS and therefore easily available as a beam at REX-ISOLDE. As target a 0.9 mg/cm^2 deuterated polyethylene foil was used. Fig. 5.1 shows a level scheme of ^{23}Ne in comparison with a shell model calculation using the USD interaction [WIL84] and the shell model code OXBASH [BRO04]. The active

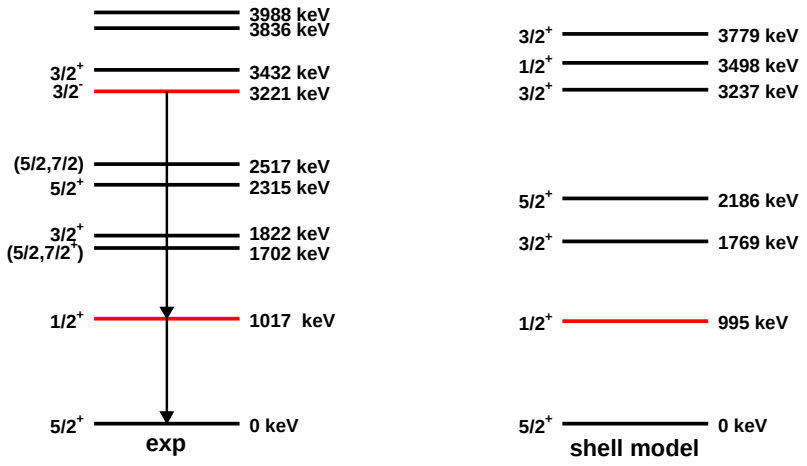

Figure 5.1: Level scheme of ^{23}Ne in comparison with a shell model calculation. Highlighted are those states and transitions relevant for the d(^{22}Ne,p)^{23}Ne reaction.

model space contains only the proton and neutron $d_{3/2}$, $d_{5/2}$ and $s_{1/2}$ orbits, thus only positive parity states can be calculated. The agreement for the excitation energies of low-spin positive parity states and also the level ordering is very good.

5.1.1 Excitation energy

The d(^{22}Ne,p) reaction populates mainly a $1/2^+$ state at 1017 keV state and several states around 3.3 MeV in ^{23}Ne. The $3/2^-$ state a 3221 keV decays via a 2204 keV γ-ray to the 1017 keV state. Fig. 5.2 shows the γ-ray energy spectrum in coincidence with protons from the transfer reaction. The green and red areas mark the γ-ray energy

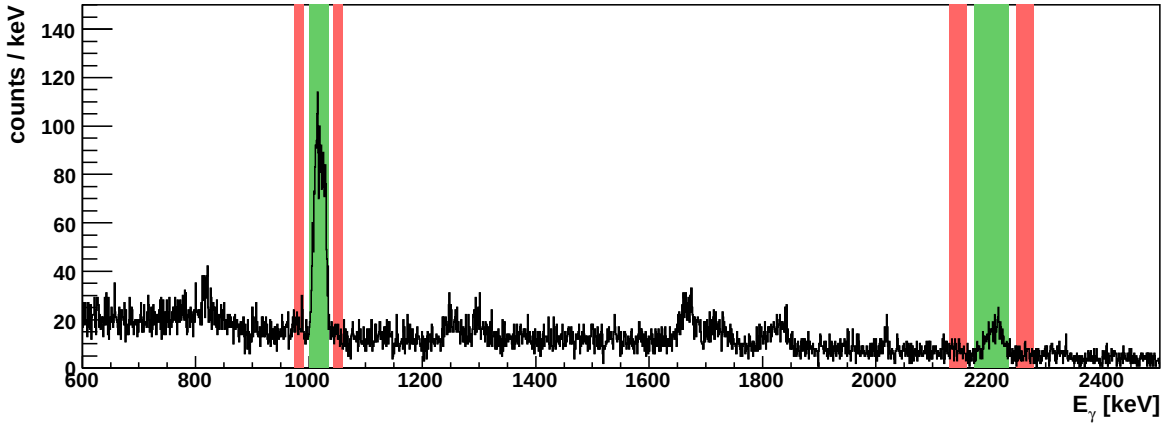

Figure 5.2: γ-ray energy spectrum of the d(^{22}Ne,p) reaction in coincidence with protons. This reaction populates mainly states at 1017 and around 3300 keV. The 3221 keV state decays via a 2204 keV γ-ray to the 1017 keV state. The green areas indicate the cut on the γ-ray transitions, while the red areas mark the background cut.

cut and the background cut, respectively. The γ-ray transitions from the 3221 keV state to the 1017 keV state and from this level to the ground state can clearly be seen. Other weaker transitions such as the direct ground state decay of the 3221 keV state are also observed, however, the statistics is not sufficient to cut on these lines. Fig. 5.3 shows the energy versus ϑ_{lab} spectrum for the d(^{22}Ne,p) reaction. In panel a), where all protons are plotted, the ground state and a band around 3.3 MeV excitation energy can be seen. When a cut on the γ-ray energy is applied, the spectrum is much cleaner and only two bands are visible (Panel b)). Fig. 5.4 a) shows the excitation energy spectrum of ^{23}Ne. For comparison also the calculated background from fusion reactions is shown. The proton spectra from fusion reactions of ^{22}Ne on ^{12}C and ^{2}H have been calculated using the PACE code [GAV80]. The contribution from reactions on ^{12}C (blue) has been fitted to the measured spectrum at "negative" excitation energies, where no contribution from the transfer reaction is expected. The fusion of ^{22}Ne with ^{2}H produces the same final nucleus ^{23}Ne, however the cross section predicted by the

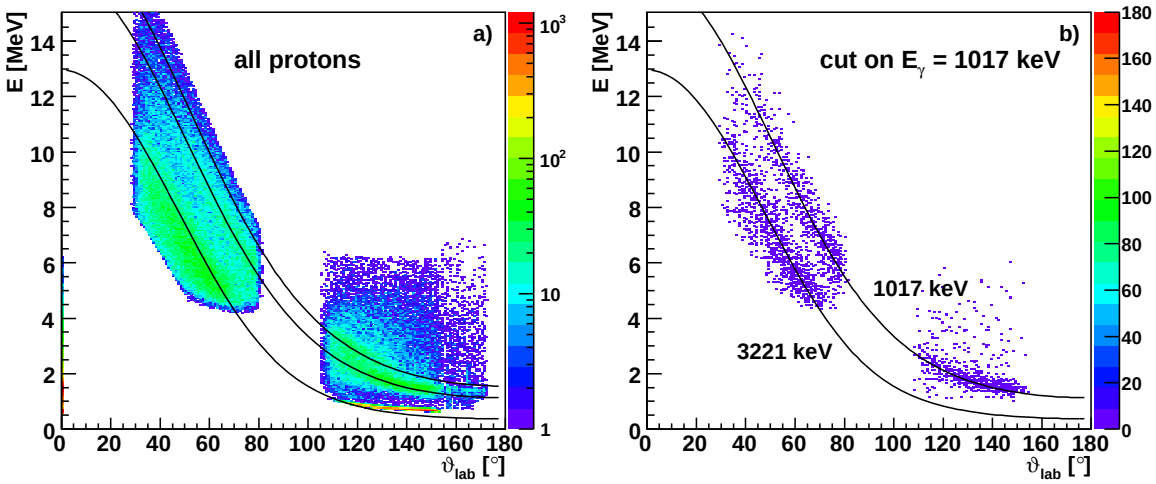

Figure 5.3: a) Energy versus ϑ_{lab} spectrum for the d(^{22}Ne,p) reaction for all proton candidates. For comparison kinematic curves for the reaction populating the ground state, the 1017 keV, and the 3221 keV state are also shown. b) Same with a cut on the 1017 keV γ-ray transition.

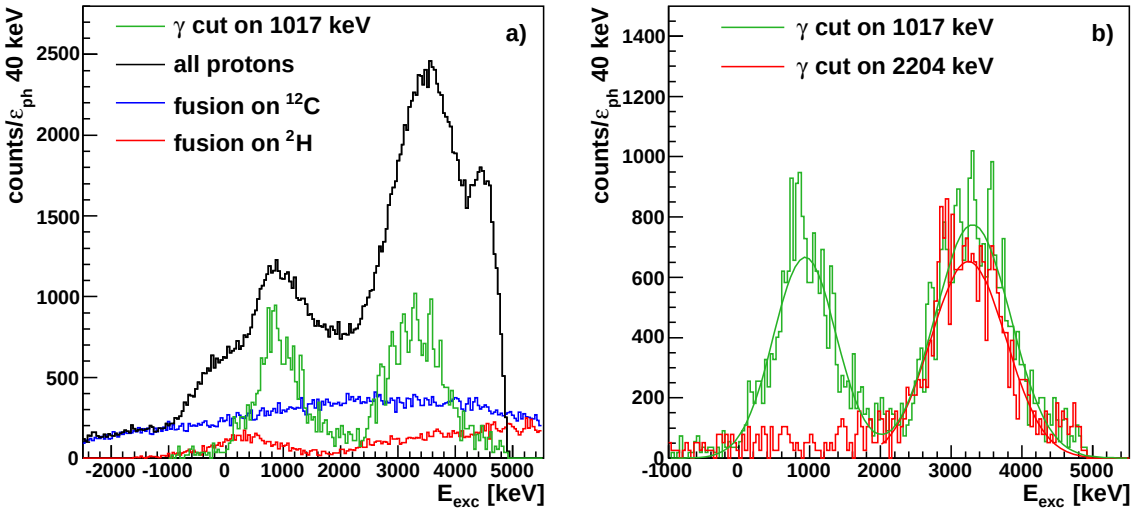

Figure 5.4: Excitation energy spectrum for the d(^{22}Ne,p)^{23}Ne reaction. a) Black: all identified protons, green: γ-efficiency corrected excitation energy spectrum with a cut on the 1017 keV γ-ray transition in ^{23}Ne. The blue and red spectra show a simulation of protons from the fusion reaction on ^{12}C and ^{2}H, respectively. b) γ-ray efficiency corrected excitation energy spectra with a cut on the two most intense lines at 1017 keV and 2204 keV in ^{23}Ne.

PACE [GAV80] or CASCADE [PÜH77] code are an order of magnitude smaller than the proton production cross section in the fusion reaction with ^{12}C and most of the

strength goes to highly excited states (red in Fig. 5.4 a)), and thus does not populated the 1017 keV state directly. Panel b) shows the excitation energy with a cut on the two prominent γ transitions at 1017 and 2204 keV. The counts have been scaled with the respective photo-peak efficiency $\varepsilon_{\mathrm{ph}}$. The 1017 keV transition appears in the decay cascades of several levels above 3 MeV, while the 2204 keV transition is only visible in the depopulation of the 3221 keV state. The areas under the peaks at 3 MeV yield the ratio of the 1017 keV γ-transitions that originate from the decay of the 3221 keV level to those that originate from the decays of other levels around 3 MeV. This population factor amounts to 0.83(4) which is in good agreement with the result from a normal kinematics experiment at similar beam energies of 0.77 [CHR74]. It can be seen that the centroid of the green curve is slightly shifted to higher energies as all the levels, other than the 3221 keV state, feeding the 1017 keV state are higher in excitation energy.

5.1.2 Fitting optical potentials

As shown in section 2.5, an optical potential for both the incoming as well as the outgoing channel is needed for the calculation of transfer reactions. A number of collections of optical model parameters exist for stable beam experiments [PER76, DAE80, BEC69]. From this global scaling relations have been determined. However, these are valid only for incident light projectile energies of $10 - 20$ MeV whereas the REX-ISOLDE beam energies correspond to a deuteron beam energy of 5.6 MeV in normal kinematics for the d(^{22}Ne,p) reaction. Also the scaling relations for some parameter exhibit a very strong dependence on the proton-neutron asymmetry $(N - Z)/A$, which becomes larger for neutron rich nuclei. Although there is a discussion going on in the literature whether to use global parameters or parameters fitted from elastic scattering data [THO09, SCH67] in this analysis we determined a new set of parameters from the elastic scattering of ^{22}Ne on d and p as well as for ^{30}Mg on t and p. The fitting procedure is described in the following.

First of all, the absolute cross section has to be determined. In order to do so, a FRESCO calculation with the initial parameter set taken from [PER76] is performed. The experimental cross section cannot be scaled to the Rutherford cross section, since due to the absorptive part of the potential the cross section can be very different from the pure point-Coulomb scattering. This is shown in Fig. 5.5 a). Here the ratio of elastic scattering to pure point-Coulomb scattering for the starting parameter sets is drawn. The average in the experimental range is then used to normalize the data. Fig. 5.5 b) shows the cross section for elastic scattering in absolute units together with the Rutherford cross section (dashed lines). The optical potential parameters are then adjusted to fit the experimental angular distributions using the SFRESCO code [THO06]. The fitted potentials are given in Table 5.1. Two sets of fitted parameters have been determined. For the first set, all parameters were adjusted, for the second set only the radii and diffuseness of the imaginary parts were fitted, while all other parameter are kept. Both sets fit the elastic scattering equally well. The result

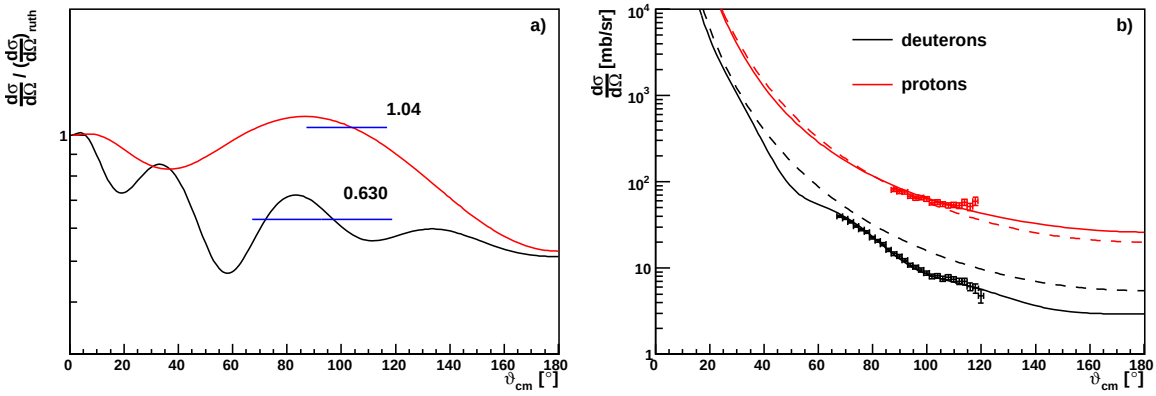

Figure 5.5: Fitting of optical potentials for the d(^{22}Ne,p) reaction. a) Ratio of elastic scattering to pure point-Coulomb scattering for the starting parameter sets [PER76]. The average in the experimental range (indicated by the blue lines) is determined to normalize the data. b) Cross section for elastic scattering of ^{22}Ne on d and p. The solid lines are obtained from fitted optical model parameters, while the dashed lines are classical Rutherford scattering.

is shown in Fig. 5.5 b) by the solid lines. Although the potential for scattering on protons was determined with the ^{22}Ne beam, this potential is taken for the p+^{23}Ne outgoing channel, as the difference of one neutron is expected to have only negligible effects on the parameters. The spin-orbit potential cannot be determined with the elastic scattering, since this would require the use of a polarized beam or target.

	V [MeV]	r_V [fm]	a_V [fm]	W_s [MeV]	r_W [fm]	a_W [fm]
d+^{22}Ne I	99.2	1.12	0.87	24.16	1.43	0.79
p+^{23}Ne I	64.5	1.2	0.72	13.4	1.32	0.68
d+^{22}Ne II	98.8	1.05	0.86	26.9	1.31	0.82
p+^{23}Ne II	56.70	1.2	0.71	12.72	1.38	0.67
d+^{22}Ne III [PER76]	98.8	1.05	0.86	26.9	1.43	0.60
p+^{23}Ne III [PER76]	56.70	1.2	0.71	11.93	1.32	0.60
n binding	-	1.3	0.66			

Table 5.1: Optical model parameter obtained from fitting the elastic scattering of ^{22}Ne on deuterons and protons (first and second set). Although the proton potential was obtained with a ^{22}Ne beam, it is used for the p+^{23}Ne outgoing channel. Third set extrapolated global parameters [PER76]. The depth of the neutron binding potential is adjusted to reproduce the binding energy.

5.1.3 Angular distribution

Fig. 5.6 shows the angular distribution for the d(^{22}Ne,p) reaction populating the 1017 keV and the 3221 keV state in ^{23}Ne. Since the shapes of the angular distribution obtained with the three different potential parameter sets differ only very slightly (see Fig. 5.6 b)), for the 3221 keV state only the curves obtained with set II are shown. By scaling the calculated angular distribution to the measured one the cross section scaling factors S can be obtained. Due to the low beam energy spectroscopic factors depend on the potential parameters chosen and should not be extracted (see section 2.5.4). Thus in this thesis S refers to the cross section scaling factor and is compared with results obtained at similar beam energies. The scaling factors for the d(^{22}Ne,p) reaction are given in Table 5.2. The results obtained with the two fitted potential parameter sets

	S $\Delta L = 0$	S $\Delta L = 1$	S^{rel}
potential	1017 keV	3221 keV cut on $E_\gamma = 2204$ keV	3221 keV relative
set I	0.69(3)	0.44(2)	0.64(3)
set II	0.75(4)	0.45(2)	0.60(4)
set III	0.59(3)	0.39(2)	0.66(5)

Table 5.2: Cross section scaling factors for the d(^{22}Ne,p) reaction for the $J^\pi = 1/2^+$ state at 1017 keV and the $J^\pi = 3/2^-$ state at 3221 keV obtained with the three different optical model parameter sets. In the last column the scaling factors for the 3221 keV state relative to those of the 1017 keV state are given.

agree within their errors, while for the global parameter set the scaling factors are 20% lower. For the 3221 keV state the scaling factor can be evaluated relative to the one obtained for the 1017 keV state. These relative scaling factors agree within their error bars for all three optical potential parameter sets. In the same way the cross section scaling factor for the 3221 keV state can be obtained from the angular distribution with a cut on the 1017 keV γ-ray transition (see Fig. 5.6 d)). However, in contrast to the 2204 keV γ-ray transition this line is not unique for the 3221 keV state (see section 5.1.1). The scaling factors for $\Delta L = 1$ obtained this way are 20% larger than the ones derived for coincidences with the 2204 keV γ-ray transition. This agrees with the population factor of 0.83(4) determined in Section 5.1.1. The angle integrated cross sections for the two states are shown in table 5.3. The values obtained with the three different optical model parameter set agree within their errors.

5.1.4 Discussion

Table 5.4 shows the results for the scaling factors obtained in this work in comparison with previous experiments. For this experiment the beam energy has been converted to the beam energy for a deuteron beam at the same center of mass energy. In general the agreement with previous experiments is good, with the exception of the experiment

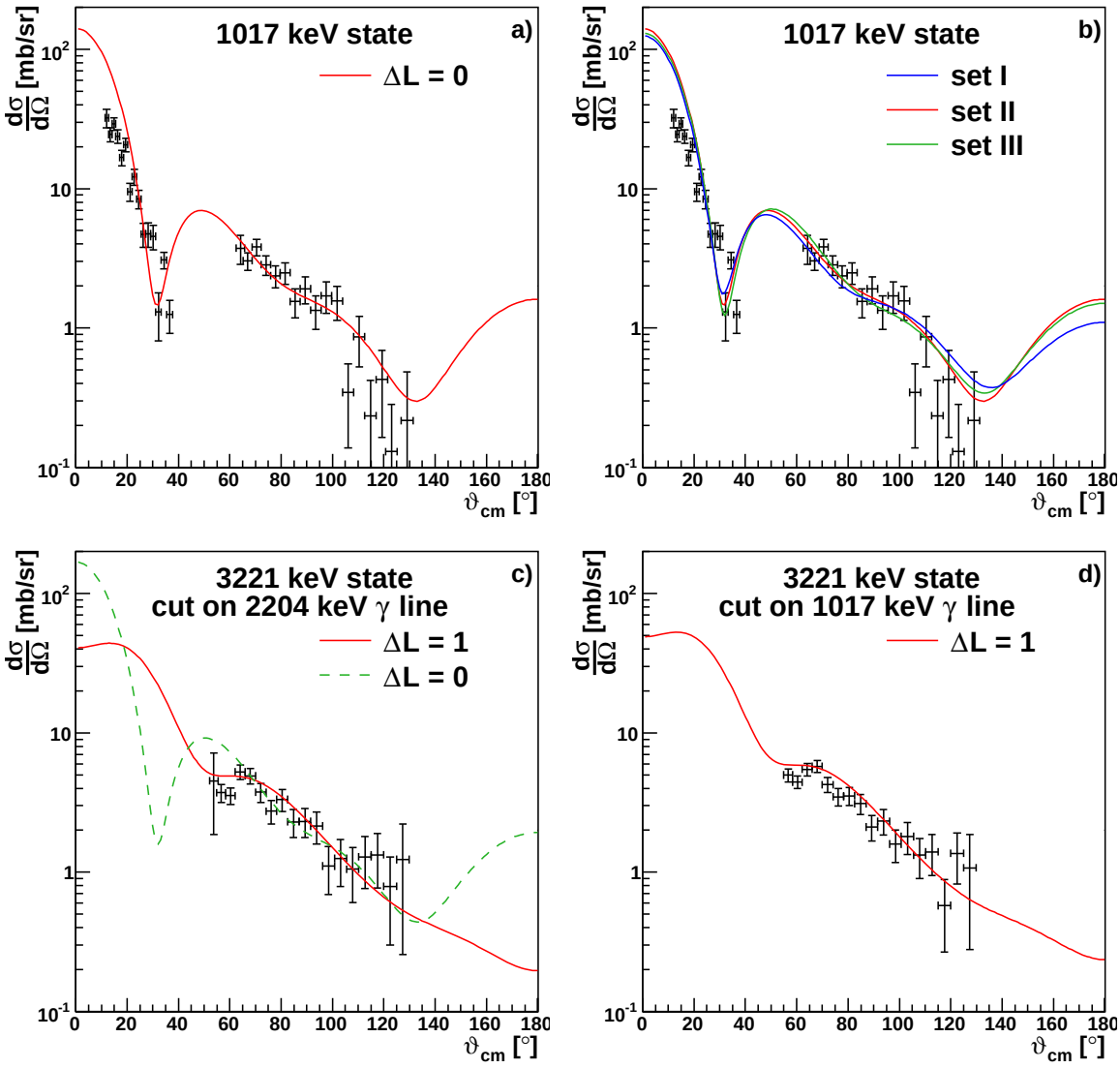

Figure 5.6: Results from the d(^{22}Ne,p)^{23}Ne reaction. a) Angular distribution for the reaction populating the 1017 keV state. This shows the characteristic pattern of a $\Delta L = 0$ transfer reaction. b) comparison of the three different potential parameter sets. c) shows the angular distribution of protons determined from coincidences with the 2204 keV γ-ray transition, which ist characteristic for the 3221 keV state. The is compared to the theoretical angular distribution for $\Delta L = 1$ (red) and 0 (green) transfer. d) same as c) but for coincidences with the 1017 keV transition. This distribution includes contribution from other states around 3 MeV as indicated in Fig. 5.1.

with a deuteron beam energy $E_\mathrm{d} = 12.1$ MeV by Lutz *et al.* [LUT67]. For the 1017 keV state they deduced a spectroscopic factor of $S = 0.40(2)$, however here the DWBA calculation was fitted to the data points at extreme forward angles while at larger

potential	1017 keV state	3221 state
set I	52.2(22)	56.4(25)
set II	56.4(30)	57.7(26)
set III	56.0(28)	61.0(31)

Table 5.3: Angle integrated cross section for the d(^{22}Ne,p) reaction. The result obtained with the three different optical model parameter set agree within their errors.

$E_{\mathrm{d}}[MeV]$	1017 keV state	3221 state	Ref.
5.74	0.75(4)	0.45(2)	this work set II
5.82	0.55		[NAN69]
4.81	0.60		[NAN69]
12.1		0.34	[CHA69]
12.1	0.4(2)	0.81(11)	[LUT67]
16.4	0.7	0.4	[HOW70]
theory	0.658		USD

Table 5.4: Comparison of the results for the d(^{22}Ne,p) reaction with previous experiments. With the exception of the work by Lutz *et al.* [LUT67] the agreement for the cross section scaling factors is good.

angles the calculation underestimates the observed cross section (Fig. 4 in [LUT67]). For the 3221 keV state a spectroscopic factor $S = 0.81(11)$ was obtained at a beam energy of 12.1 MeV [LUT67]. However, the authors assumed $J^\pi = 1/2^+$ and $\Delta L = 0$ for this state. If the $\Delta L = 0$ angular distribution is fitted to the data in the present analysis (dashed green line in Fig. 5.6 b)) a cross section scaling factor $S = 0.78(5)$ is obtained for the parameter set I, however, the quality of the fit is worse compared to the $\Delta L = 1$ fit. For the $1/2^+$ state the spectroscopic factor can also be obtained from the shell model USD calculation. Here the spectroscopic amplitude is $A(1/2^+, 995\ \mathrm{keV}) = 0.881$ which gives rise to a spectroscopic factor $S = A^2 = 0.658$ which is of the same order as the extracted cross section scaling factor.

In summary, the d(^{22}Ne,p)^{23}Ne reaction has been used to test the setup and the analysis methods. The results obtained from this test measurement are in good agreement with previous experiments and shell model calculations which shows that the analysis method and the fitting of optical model parameters is valid and can be applied to the t(^{30}Mg,p)^{32}Mg reaction.

5.2 The t(^{30}Mg,p) reaction

In this section the results from the main experiment, the t(^{30}Mg,p) reaction, are presented. Here the beam energy was lowered compared to the normal energy to

1.8 MeV/u in order to avoid fusion reactions on the Ti carrier material of the target. The beam intensity has been determined from the elastic scattered tritons (see section 5.2.3) and amounts to $\approx 4 \cdot 10^4$ part/s. Fig. 5.7 a) shows the energy versus ϑ_{lab} spectrum for all detected particles. For comparison also the kinematic curves for

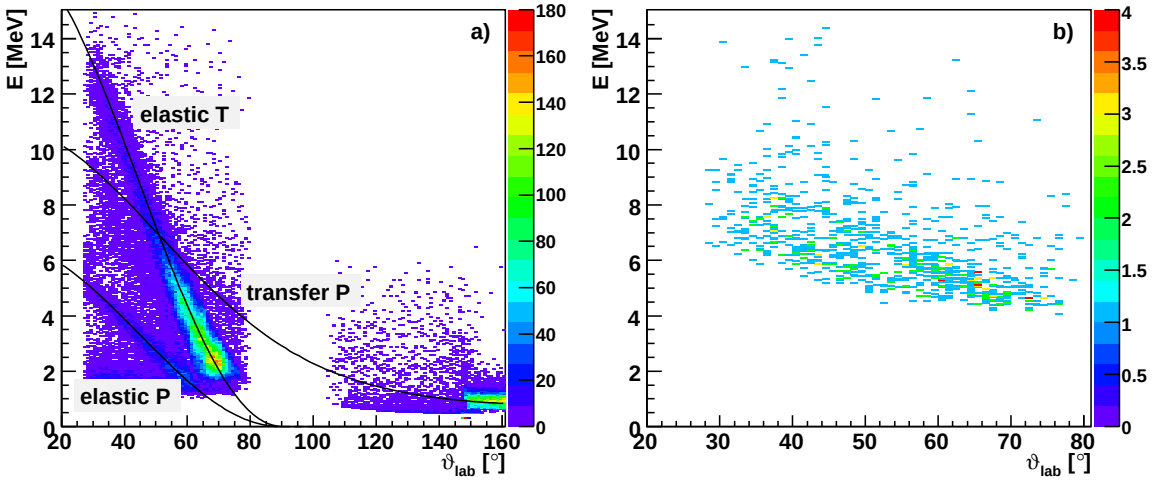

Figure 5.7: a) Energy versus ϑ_{lab} spectrum for ^{30}Mg on the tritium target for all particles. Elastic scattered tritons and protons can clearly be seen. b) Same for identified protons, the two states can be observed.

elastic scattering and transfer reactions are drawn. Fig. 5.8 shows the $\Delta E - E$ particle identification plot. Here the energy loss in the ΔE layer has been corrected in order to show the statistics of all strips together. No deuterons have been observed during this experiment. Due to the large negative Q-value (-3.9 MeV) the t(^{30}Mg,d)^{31}Mg

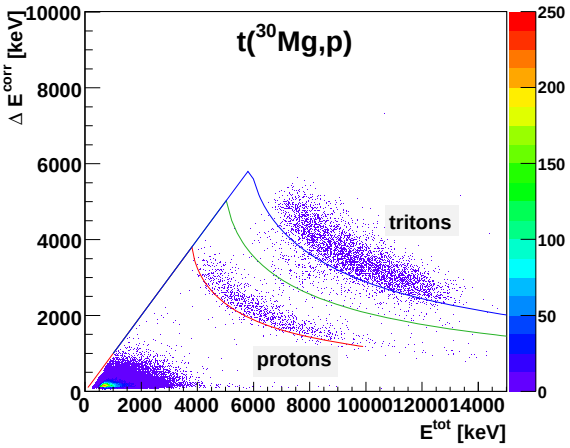

Figure 5.8: Particle identification for the t(^{30}Mg,p) reaction. The energy loss of particles in the ΔE detector has been corrected for their emission angles as described in section 4.2.

reaction is energetically forbidden (see Fig. 2.7). Also, no elastic scattered deuterons are observed, indicating a very low deuteron content of the target.

All elastic scattered protons are stopped in the ΔE layer of the detector. Thus, the identification cut for protons only contains reaction events. This is shown in Fig. 5.7 b) where the two states in ^{32}Mg can already be seen. For laboratory backward angles no identification is possible. Here events which have deposited energy in the E detector or a strip multiplicity larger than two for not neighboring strips are counted as electrons. As shown in section 3.7 these cuts have nearly no effect on protons, while electrons are significantly suppressed.

5.2.1 Excitation energy of the 0_2^+ state in ^{32}Mg

After identifying protons with the $\Delta E - E$ telescopes, for each event the excitation energy of the ejectile nucleus ^{32}Mg can be determined from the energy and emission angle of the proton (see section 4.2.2). Fig. 5.9 shows the excitation energy spectrum for the identified protons. Two states have been observed, the ground state of ^{32}Mg

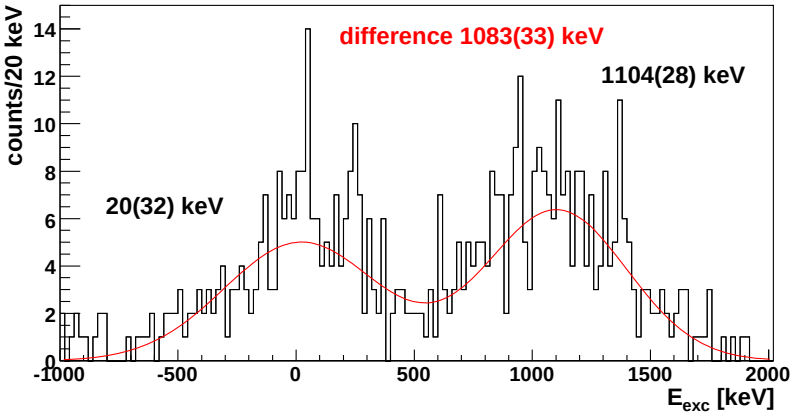

Figure 5.9: Excitation energy spectrum of the ejectile nucleus ^{32}Mg reconstructed from the measured energy of unambiguously identified protons in T-REX. The excitation energy of the observed state amounts to 1083(33) keV.

and an excited state at 1083(33) keV. The systematic shift of the excitation energy by $\approx$ 20 keV is also observed for elastic scattered tritons and protons and is thus due to limited accuracy of the calibration and/or target thickness. Also uncertainties in the masses of the involved nuclei or the Q-value of the reaction lead to systematic shifts in the derived excitation energy. Most recent mass measurements of ^{30,32}Mg have uncertainties of $10 - 20$ keV [AUD03, LUN06].

5.2.2 γ decay and lifetime of the 0_2^+ state in ^{32}Mg

The γ-ray energy spectrum recorded in coincidence with protons from the two neutron transfer reaction to the excited state is shown in Fig. 5.10. The two peaks at 172 keV

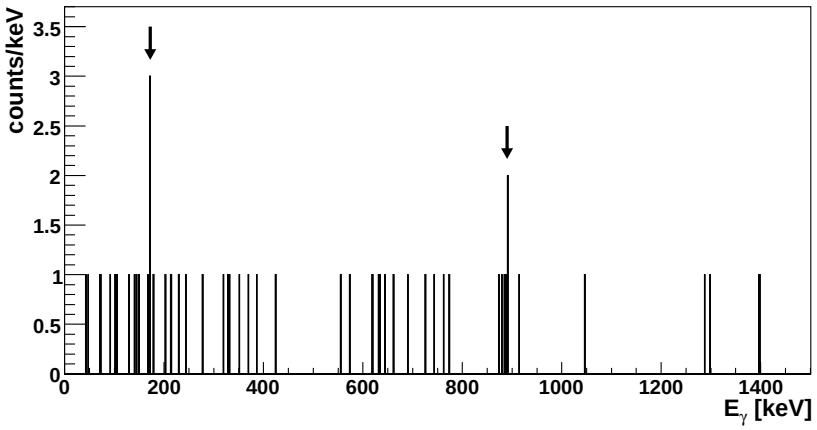

Figure 5.10: γ-ray energy spectrum in coincidence with protons from transfer to the excited states. Two transitions with very low intensity are visible.

(6(3) counts) and 886 keV (4(2) counts) suggest a cascade from a 1058(2) keV level through the well known 2^+ level at 886 keV. This low count rate further confirms that the 2^+ state has not been populated directly in the (t,p) reaction. This value of 1058 keV for the excitation energy of the initial state is consistent with the observed excitation energy kinematically reconstructed from the proton energies. From the counts in the proton spectrum ($\approx$ 300 counts for the excited state) it is possible to estimate the expectation for the number of observed γ-proton coincidences for a prompt decay of this excited state. With a γ-ray detection efficiency of $\varepsilon_{\mathrm{ph}}(886\mathrm{keV}) = 5.9$ % one would expect 18(2) counts in the 886 keV γ-ray transition line. The low rate of observed γ-proton coincidences, compared to this expectation, points to a rather long lived excited state as one may expect for a 0^+ state. Assuming a 0^+ state at 1058 keV and no contribution from E0 decay, its lifetime can be estimated from the reduced γ-ray detection efficiency due to the emission in flight and not at target position. If the excited state decays in flight, the efficiency for the detection of a γ-ray is reduced. The relative efficiency of emission at the target position to any other point along the beam axis depends on the path length and thus on the lifetime of the state. The result is shown in Fig. 5.11. Taking into account only a geometrical reduction of the detection efficiency this estimate amounts to $\approx$ 13 ns. This is shown by the green points, where point-like Germanium detectors and no absorption was assumed. A more realistic estimate was obtained using the GEANT4 simulation. Here the position of the individual MINIBALL clusters was adjusted to the position in the actual experiment. Furthermore, absorbing material such as beam-pipes was included. The results for the efficiency depending on the lifetime of the excited state are shown by the red points in Fig. 5.11. The observed 4(2) counts for the 886 keV transition indicate a long lifetime

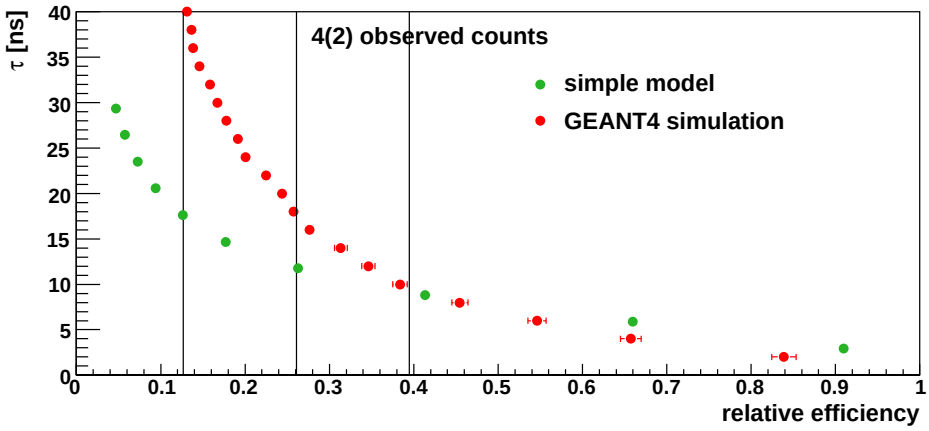

Figure 5.11: Estimate of the lifetime of the excited 0^+ state. The green points show the simple assumption of point-like Germanium detectors and ignoring absorption in material, like the target chamber. The red point show a realistic simulation using GEANT4. The observed 4(2) counts for the 886 keV transition indicate a long lifetime of at least 10 ns.

of at least 10 ns. Also the fact that most counts for the $2_1^+ \rightarrow 0_1^+$ transition lie slightly below the known transition energy of 886 keV points to the fact, that these are wrongly Doppler corrected due to the emission after the target.

Fig. 5.12 shows the dependence of the lifetime τ of the 0_2^+ state on the $B(\mathrm{E2}; 0_2^+ \rightarrow 2_1^+)$ value for different assumptions for the electric monopole strength $\rho^2(\mathrm{E0})$. The partial

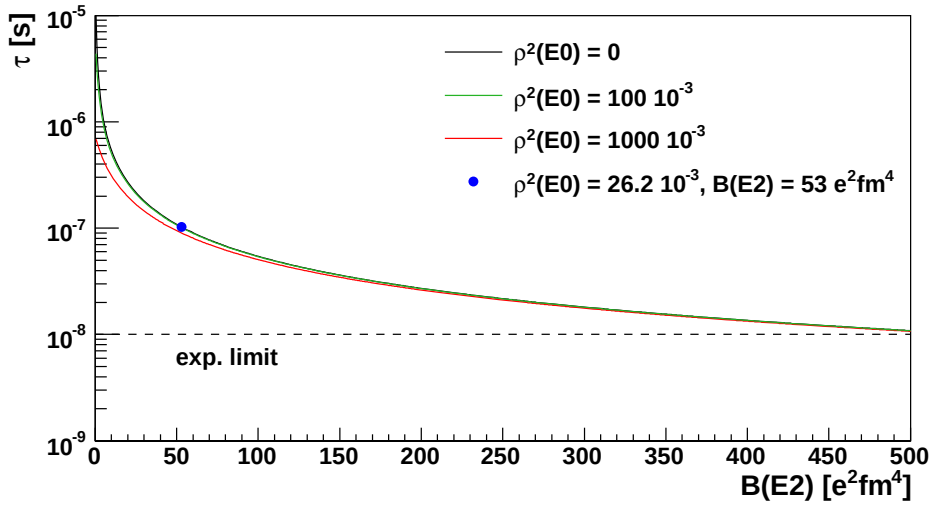

Figure 5.12: Dependence of lifetime of the excited 0^+ state on the $B(\mathrm{E2}; 0_2^+ \rightarrow 2_1^+)$ value. The E0 decay branch is negligible, only very large unrealistic values of $\rho^2(\mathrm{E0}) \gtrsim 1$ have an effect on the lifetime (red curve). The blue point shows the estimate using the matrix elements from ^{30}Mg.

lifetime of the E0 transition to the ground state $\tau(\mathrm{E0}) = (\rho^2(\mathrm{E0}) \cdot \Omega_{\mathrm{tot}})^{-1}$ depends on the non-nuclear electric factor $\Omega_{\mathrm{tot}} = \Omega_{\mathrm{K}} + \Omega_{\mathrm{L}} + \cdots + \Omega_{\mathrm{IP}}$. Due to the low energy of the $0_2^+ \rightarrow 0_{\mathrm{gs}}^+$ transition, the internal pair production process is forbidden, resulting in $\Omega_{\mathrm{tot}} = 1.361 \cdot 10^6$, which is almost two orders of magnitude lower than for the ^{30}Mg case ($\Omega_{\mathrm{tot}} = 9.642 \cdot 10^7$) [KIB08]. Thus, the E0 decay branch has to be weak compared to the E2 γ decay, as otherwise the electric monopole strength ρ^2(E0) would be extremely large. This is shown by the red curve in Fig. 5.12, only very large unrealistic values of $\rho^2(\mathrm{E0}) \gtrsim 1$ have an effect on the lifetime. For a partial lifetime of $\tau(\mathrm{E0}) = 10$ ns the electric monopole strength would have to be $\rho^2(\mathrm{E0}; 0_2^+ \rightarrow 0_{\mathrm{gs}}^+) = 78$ compared to $\rho^2(\mathrm{E0}) = 26.2(75) \cdot 10^{-3}$ in ^{30}Mg [SCH09]. The lifetime of the 0_2^+ can also be estimated using the E0 matrix element $\rho^2(\mathrm{E0}; 0_2^+ \rightarrow 0_{\mathrm{gs}}^+)$ and the relevant value $B(\mathrm{E2}; 0_2^+ \rightarrow 2_1^+)$ [MAC05, SCH09] from ^{30}Mg which amounts to 102 ns (blue point in Fig. 5.12). Such a value would indicate a small mixing of the two shapes. However, large collective B(E2) values for the $0_2^+ \rightarrow 2_1^+$ transition cannot be excluded by the lifetime estimate $\tau > 10$ ns. In case of strong mixing of the two configurations a large $B(\mathrm{E2}; 0_2^+ \rightarrow 2_1^+)$ value would be expected.

5.2.3 Angular distributions

From the elastic scattering of ^{30}Mg on tritium the beam intensity can be determined. It amounts to $4.6(5) \cdot 10^4$ part/s. The biggest source of uncertainty is the tritium content of the target. During the production of the target the flow of tritium was monitored, so the amount absorbed in the production container is known with good accuracy. However, tritium might also be absorbed on the target holder during the production process. The uncertainty in the tritium content amounts to 10 %. However, for the determination of the cross section only the knowledge of the product of beam current and target thickness is required and this quantity can be determined with good prescission. As shown in Fig. 5.7 the target also contains protons. The amount of protons can be determined from the elastic scattering. The ratio of protons to tritons in the target is 2.6(8) %. Deuterons have not been observed (see Fig. 5.8) thus the deuteron content of the target is negligible.

As in the analysis of the d(^{22}Ne,p) reaction the absolute cross section scale has to be determined from the elastic scattering. Here contributions from the beam contamination have to be carefully considered. It was assumed that for elastic scattering of ^{30}Al on protons and tritons the same optical model parameters as for ^{30}Mg can be used. The experimental cross section has been corrected for the ^{30}Al content of the beam (see section 3.3). However, Al does not contribute to the proton angular distributions. The Q-value for the t(^{30}Al,p) reaction is $Q = 2.85$ MeV, this would lead to larger proton energies (or equivalently to "negative" excitation energies) than for the t(^{30}Mg,p) reaction, which have not been observed (see Fig. 5.7 b)). By fittings the optical model to the elastic scattering of tritons and protons the parameters for the DWBA calculation can be determined. The obtained parameters are shown in Table 5.5 together with the global parameter set [PER76]. As in the case of the d(^{22}Ne,p) reaction two sets

	V	r_V	a_V	W	W_s	r_W	a_W
t+^{30}Mg I	172.71	1.13	0.6	16.17		1.36	0.93
p+^{32}Mg I	64.5	1.2	0.72		13.4	1.32	0.68
t+^{30}Mg II	177.67	1.14	0.62	17.14		1.34	0.97
p+^{32}Mg II	64.5	1.2	0.66		13.4	1.32	0.68
t+^{30}Mg III [PER76]	162.78	1.17	0.75	22.17		1.40	0.84
p+^{32}Mg III [PER76]	59.74	1.2	0.71		13.42	1.43	0.63
n binding	-	1.3	0.66				

Table 5.5: Optical model parameter obtain from fitting the elastic scattering of ^{30}Mg on tritons and protons (first set). Although the proton potential was obtained with a ^{30}Mg, it is used for the p+^{32}Mg outgoing channel. Third set global parameters extrapolated from stable nuclei [PER76]. The depth of the neutron binding potential is adjusted to reproduce the binding energy.

of fitted potential parameters have been determined. Both potentials fit the shape of the elastic scattering very well. For the p+^{32}Mg potential the fit result for p+^{30}Mg is taken. The fitted potential does not differ a lot from the global model parameters, this scattering is essentially described by the Rutherford cross section. The resulting angular distributions of elastic scattering are shown in Fig. 5.13.

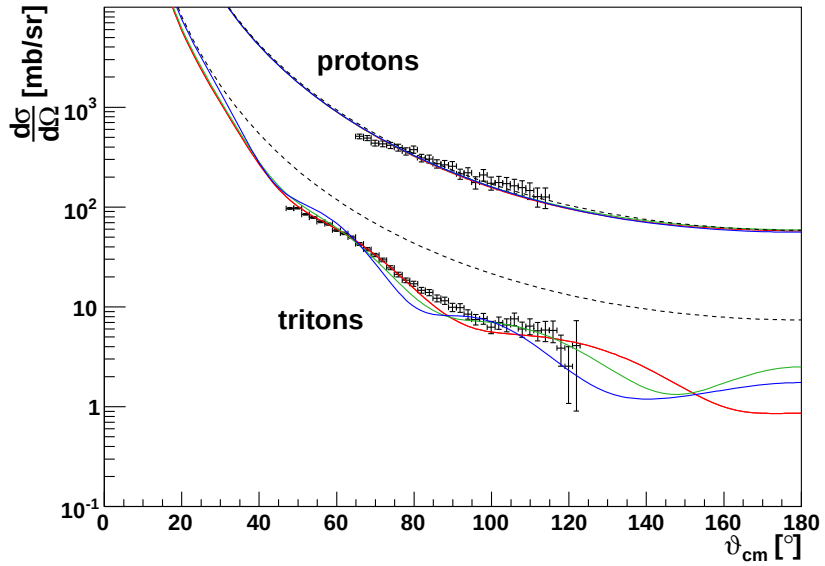

Figure 5.13: Angular distribution of elastic scattering of ^{30}Mg on tritons and protons. Dashed lines show the point Coulomb scattering cross section. The solid colored lines show the result obtained with the three different parameters sets, in red, green, and blue for set I, II and III, respectively.

These optical model parameter sets are then applied to the calculation of the two neutron transfer cross section. Fig. 5.14 shows the angular distribution for the reaction to the ground state in ^{32}Mg. The data clearly show a $\Delta L = 0$ angular distribution for this state. The shape obtained with the three parameter sets differ slightly, the best fit is obtained with parameter set II. The angle integrated cross section for the ground state amounts to 10.5(7) mb.

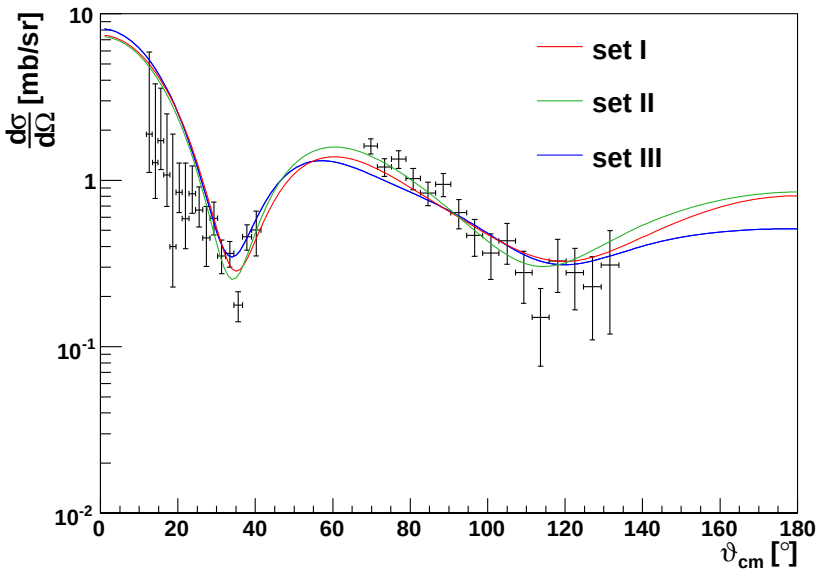

Figure 5.14: Angular distribution of protons from the reaction populating the ground state of ^{32}Mg. The distributions calculated with the three different potential parameter sets differ only slightly. The best fit is obtained for parameter set II (green).

Fig. 5.15 a) shows the angular distribution for the reaction to the excited state in ^{32}Mg. The choice of the optical model parameters has little influence on the shape of the angular distribution (see Fig. 5.15 a)). In Fig. 5.15 b) the experimental angular distribution is compared with predictions for $\Delta L = 0$, $\Delta L = 1$, and $\Delta L = 2$. The best fit result is clearly obtained for $\Delta L = 0$. Angular momentum transfer of $\Delta L = 1$ and 2 can be excluded as $\Delta L = 1$ has its first maximum at $\vartheta_{\mathrm{cm}} = 30°$ and $\Delta L = 2$ at $\vartheta_{\mathrm{cm}} = 40°$. The second maximum for $\Delta L = 2$ transfer is at $\vartheta_{\mathrm{cm}} = 120°$, where we observe a minimum. Also in both cases unrealistic, large spectroscopic amplitudes $A > 2$ are needed in order to fit the experimental cross section.

Thus, we have clearly observed a new excited 0^+ state at 1058(2) keV in ^{32}Mg which is long-lived with a lifetime of $\tau > 10$ ns. The angle integrated cross section for this excited 0^+ state amounts to 6.5(5) mb.

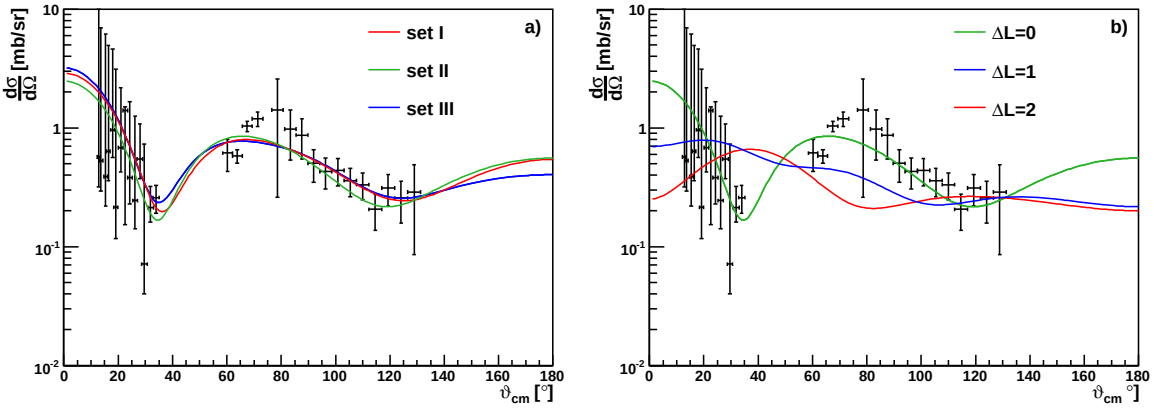

Figure 5.15: Angular distribution for the reaction to the 1058 keV excited state of ^{32}Mg. Panel a) shows the distributions calculated with the three different potential parameter sets. Panel b) shows the angular distribution for $\Delta L = 0$ (green), $\Delta L = 1$ (blue) and $\Delta L = 2$ (red). The best fit result is obtained with $\Delta L = 0$.

5.3 Discussion

The observed excitation energy of the 0_2^+ state at 1058 keV in ^{32}Mg is much lower than predicted by theory. This is shown in Fig. 5.16. The shell model calculation by Caurier *et al.* [CAU01] predicts a low-lying excited 0^+ state at 1.4 MeV. The agreement for the $B(\mathrm{E2}; 2_1^+ \rightarrow 0_{\mathrm{gs}}^+)$ values in ^{30}Mg and ^{32}Mg is very good. However, this calculation also overestimates the energy of the 0_2^+ state at 1789 keV in ^{30}Mg. With Monte Carlo shell-model [OTS01b] calculations using the SDPF-M effective interaction it is possible to include large model spaces and unrestricted mixing of $np-nh$ configurations. The excitation energy of the 0_2^+ state obtained in this calculation is much larger (3.1 MeV) than the experimental value [OTS04]. Also this model fails to predict the correct ground state spin $J^\pi = 1/2^+$ for ^{31}Mg [NEY05]. Calculations going beyond the mean field by incorporating configuration mixing and projection on the particle number and angular momentum [ROD07] using the finite range density dependent Gogny force with the D1S parametrization [BER84] have reasonably reproduced the excitation energy of 2.11 MeV for the 0_2^+ state in ^{30}Mg and only weak mixing between the two 0^+ states [SCH09]. Earlier calculations by the same group predict the 0_2^+ state in ^{32}Mg at 1.7 MeV [ROD02b]. The most recent calculation of the shape mixing properties of neutron rich Mg isotopes by Hinohara *et al.* [HIN10a] predicts a low-lying 0_2^+ state in ^{32}Mg at 1125 keV. This model, based on constrained Hartree-Fock-Bogoliubov (CHFB) and local quasi-particle random-phase approximation (LQRPA), was first applied to proton-rich ^{68,70,72}Se where an excellent agreement for the yrast states was obtained [HIN10b]. For ^{30}Mg this model predicts a 0_2^+ state below the 2_1^+ state at 1060 keV and a strong transition from the 2_1^+ state to this excited 0^+ state. The authors interpret this as a shape change in the ground state band and find shape mixing

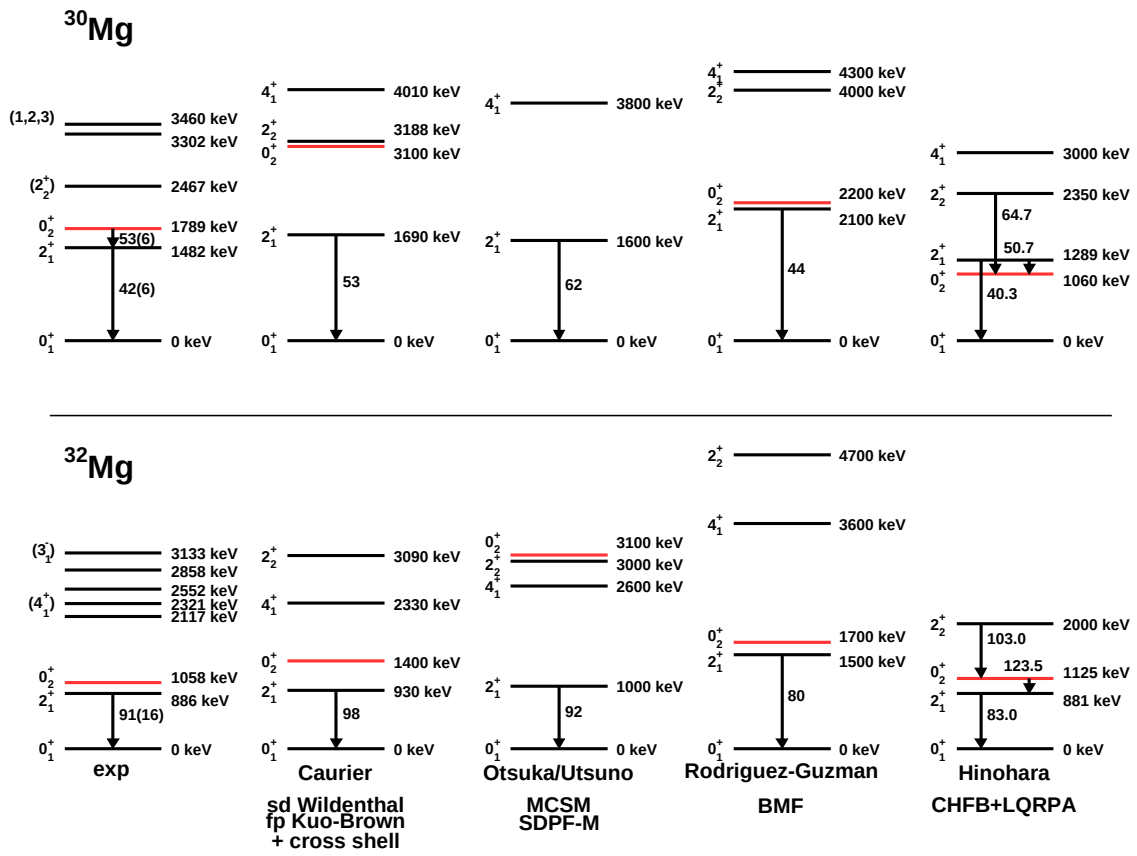

Figure 5.16: Level scheme of ^{30,32}Mg in comparison with predictions from various theoretical calculations. Arrows indicate E2 transitions with their respective B(E2) values in e^2fm^4. The experimental values are taken from [MAC05, SCH09, ENS07], while theoretical values are taken from [CAU01, OTS04, UTS99, ROD02b, HIN10a].

in the 0^+ and 2^+ states. However the matrix element for the $0_2^+ \rightarrow 2_1^+$ is much larger than the experimentally observed $B(\mathrm{E2}; 0_2^+ \rightarrow 2_1^+) = 53(6)\ e^2\mathrm{fm}^4$. Thus, none of the models is able to correctly describe the excitation energies of the 2_1^+ and 0_2^+ states as well as the B(E2) values in both ^{30}Mg and ^{32}Mg.

Nevertheless, it is interesting to estimate if the observed cross-sections for the population of the ground state and the excited 0^+ state are consistent with expectations based on their underlying single-particle structure.

5.3.1 The ground state of ^{32}Mg

Fig. 5.17 shows the ground state neutron occupation numbers calculated within the Monte Carlo shell-model (MCSM) using the SDPF-M effective interaction [OTS01b] as well as OXBASH [BRO04] calculations using the USD interaction [WIL84]. While

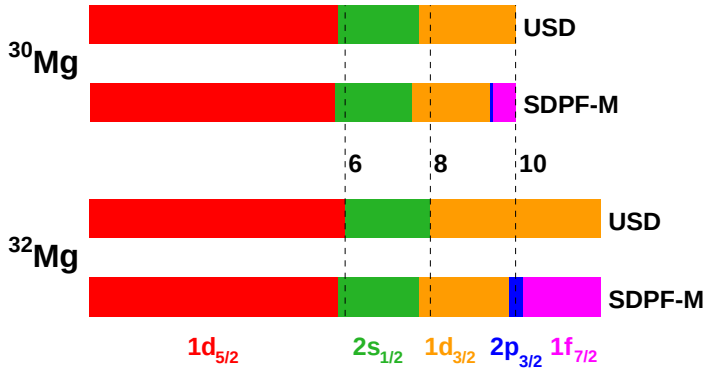

Figure 5.17: Ground state neutron occupation numbers outside the ^{16}O core calculated with the Monte Carlo shell-model using the SDPF-M effective interaction and OXBASH calculations using the USD interaction. (Adopted from [TER08])

the USD model space contains only the $1d_{5/2}$, $2s_{1/2}$, and $1d_{3/2}$ orbits and thus can only give rise to $0p-0h$ configurations, the MCSM calculation predicts a significant contribution of $fp\ 2p-2h$ configurations already for the ground state of ^{30}Mg. For the ground state of ^{32}Mg the MCSM predicts an almost pure $2p-2h$ configuration with a neutron occupation number $\langle n\rangle$ of 0.32 for the $p_{3/2}$ and 1.83 for the $f_{7/2}$ orbital [TER08]. This suggests that the two neutrons are predominately added to the $f_{7/2}$ orbital in the transfer reaction to the ground state.

The experimental cross section, however, cannot be described by a simple $(\nu f_{7/2})^2$ configuration. This is shown by the purple lines in Fig. 5.18. The $(\nu f_{7/2})^2$ configuration has a very low two neutron transfer cross section due to the radial mismatch [HER84]. This can be explained by looking at the wave functions in a Wood-Saxon potential. Fig. 5.19 shows the single particle energies and the radial wave functions for the relevant orbits. For a peripheral transfer reaction only the wave function at the nuclear surface is relevant. Due to the larger principal quantum number and the additional oscillation in the radial wave function, the $2s_{1/2}$ and $2p_{3/2}$ orbits have a larger value of the wave function at the surface. This enhances the transfer cross section for these orbitals.

In order to reproduce the (t,p) data a coherent sum $a(\nu p_{3/2})^2 + b(\nu f_{7/2})^2$ is needed. Since contribution to the cross section for the $(\nu f_{7/2})^2$ configuration is small a lower limit for a has been determined by setting $b = \sqrt{1-a^2}$ in order to fulfill the sum rule in Eq. 2.38. This assumes that no other orbital plays a role. One obtains $a \geq 0.71$ for parameter set I and $a \geq 0.84$ for set II. The square $a^2 \geq 0.51$ (set I) then gives the weight of the $(\nu p_{3/2})^2$ two particle configuration within the final state in ^{32}Mg. This is in agreement with the results of a recent one neutron knockout reaction experiment to ^{31}Mg, where a large spectroscopic strength for the $3/2^-$ state is observed [TER08]. The deduced spectroscopic factor for the knockout reaction to the final $(3/2)^-$ state at 221 keV in ^{31}Mg is $S_{\mathrm{exp}} = 0.59(11)$. This is almost a factor of 2 larger than the upper

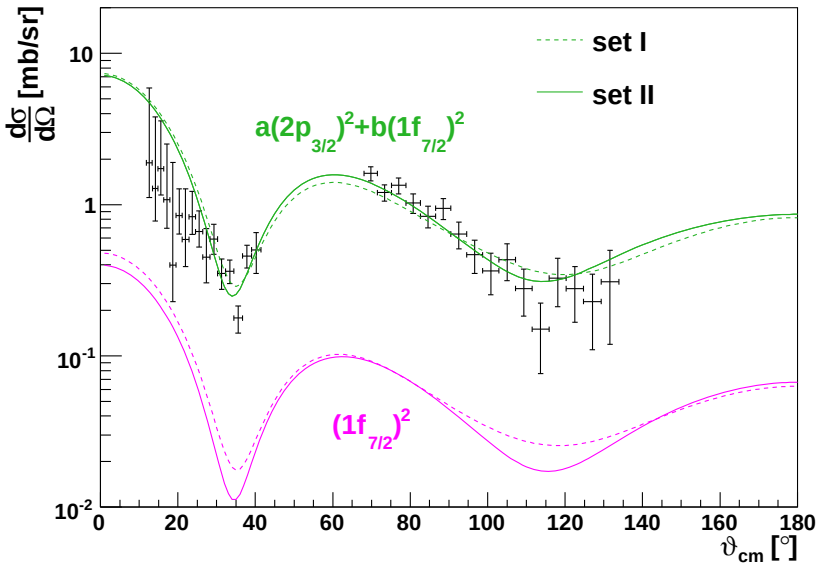

Figure 5.18: Transfer amplitudes for the ground state in ^{32}Mg. The simple assumption of a $(\nu f_{7/2})^2$ configuration (purple) does not reproduce the experimental cross section. In order to fit the data a coherent sum of $(p_{3/2})^2$ and $(f_{7/2})^2$ is needed. The green curves show the result for $a(\nu p_{3/2})^2 + b(\nu f_{7/2})^2$ for parameter sets I (solid) and II (dashed lines).

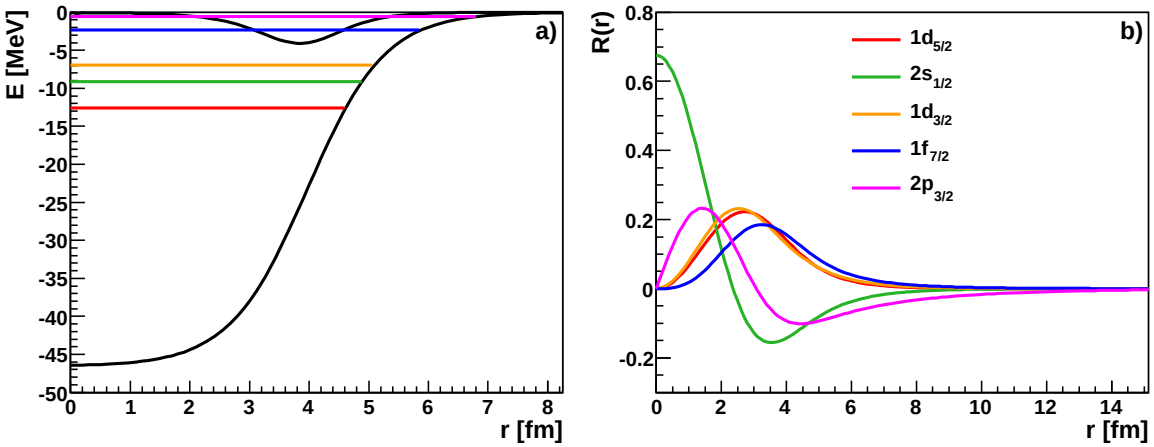

Figure 5.19: a) Neutron binding potential for the transfer reaction calculation. The black lines show the Wood-Saxon central potential and the spin-orbit potential. The colored lines indicate the single particle energies. b) Radial wave functions for the relevant orbits. Because of the higher principal quantum number n the $2s_{1/2}$ and $2p_{3/2}$ orbits extend further out. For a peripheral reaction the overlap is thus larger for these orbits.

limit given by occupation number $\langle n \rangle = 0.32$ calculated in the MCSM. Both results indicate that the MCSM underestimates the $\nu p_{3/2}$ contribution to the ground state wave-function in ^{32}Mg. In the one neutron knockout reaction from ^{33}Mg an even larger occupancy of the $\nu p_{3/2}$ orbital was observed [KAN10]. For ^{33}Mg the spectroscopic factor for $p_{3/2}$ ($S = 1.1$) is even larger than for $f_{7/2}$ ($S = 0.5$). This suggests that the $\nu p_{3/2}$ orbit is lowered in energy.

5.3.2 The excited 0^+ state in ^{32}Mg

The excited 0^+ state in ^{32}Mg should have a rather pure *sd* configuration and can therefore be described with the USD effective interaction [WIL84]. The wave-function obtained for the ground state of ^{32}Mg in shell model calculations with the USD interaction has a pure *sd* configuration and thus should resemble the expected wave-function of the excited 0^+ state relatively well. Two neutron spectroscopic amplitudes A for the transition of pure *sd* wave-functions for the 0^+ states in ^{30}Mg and ^{32}Mg have been calculated using the OXBASH [BRO04] code. They amount to -0.209, -0.184, and -0.808 for the $(1d_{5/2})^2$, $(2s_{1/2})^2$, and $(1d_{3/2})^2$ configurations, respectively. Fig. 5.20 shows the two neutron transfer cross section for the amplitudes calculated with the USD interaction (red lines). The transfer cross section calculated with these amplitudes is a factor

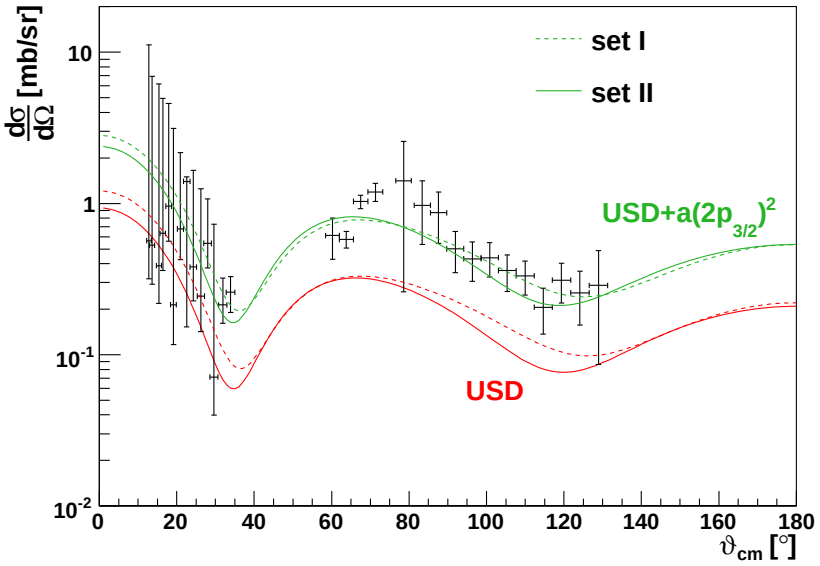

Figure 5.20: Transfer cross section for the excited state in ^{32}Mg. The transfer cross section calculated with the USD amplitudes (red lines) is a factor of two lower than the experimental result. By adding a small $(p_{3/2})^2$ contribution ($a = 0.3$) to the overlap function, the experimental data can be reproduced (green lines).

of two lower than the experimental result, however, if a small contribution of $(p_{3/2})^2$ is

added to the overlap function, the experimental data can be reproduced. The amount of $(p_{3/2})^2$ depends on the optical model parameter set chosen. However, the uncertainty is quite large (see Table. 5.6). Such a small additional $(p_{3/2})^2$ contribution is predicted

nl_j	$A_{\rm gs}$ set I	$A_{\rm gs}$ set II	$A_{\rm ex}$ set I	$A_{\rm ex}$ set II
$1d_{5/2}$			-0.209	-0.209
$2s_{1/2}$			-0.184	-0.184
$1d_{3/2}$			-0.808	-0.808
$2p_{3/2}$	$\geq 0.713(18)(27)$	$\geq 0.845(23)(32)$	0.287(11)(11)	0.323(17)(12)
$1f_{7/2}$	$\leq 0.701(18)(27)$	$\leq 0.534(36)(51)$	0.0	0.0

Table 5.6: Two neutron spectroscopic amplitudes A for the configurations of ^{32}Mg. For the ground state (gs) the $(1f_{7/2})^2$ amplitude was fixed to 1.0, while the $(2p_{3/2})^2$ was varied in order to fit the data. The excited state (ex) was fitted with the amplitudes for the *sd* shell calculated with the USD interaction and a small $(2p_{3/2})^2$ contribution. The errors include statistical errors as well as the uncertainty of the absolute cross section due to the beam contamination.

for the ^{30}Mg ground state (see Fig. 5.17) and thus this finding may not be surprising. Overall, the measured cross section for the excited 0^+ state can be described by DWBA calculations using spectroscopic amplitudes based on almost pure *sd* configurations with a small addition of $(p_{3/2})^2$ contributions. The current data also confirm previous evidence that MCSM calculations with the SDPF-M effective interaction underestimate the $\nu p_{3/2}$ component in the ^{32}Mg ground state.

6 Studies for future T-REX experiments

In this chapter studies for future T-REX experiments which have been performed in the framework of this thesis are presented. The first section demonstrates the advantages of using a modified T-REX setup for Coulomb excitation experiments at REX-ISOLDE instead of a simple annular Silicon strip detector. In the second section the feasibility of an experiment to measure the E0 decay of the excited 0^+ state in ^{32}Mg is investigated. In the last section of this chapter the proposal for a new (t,p) two neutron transfer experiment is presented. The aim of this experiment is to study the deformation and shape coexistence in ^{46}Ar.

6.1 T-REX for Coulomb excitation

In the future the T-REX setup should be used for Coulomb excitation experiments as well. One disadvantage of Coulomb excitation experiments at MINIBALL up to now, is the limited angular coverage of just one CD detector covering fixed laboratory angles ($\vartheta_{\mathrm{lab}} = 16^\circ - 54^\circ$). With an increased solid angle of the T-REX setup and the flexibility to vary distances between CD detector and target, the efficiency for detecting ejectile or recoil, or both particles at the same time, can be significantly increased. In order to quantify the advantages of the new detection system extensive simulation studies have been performed in the framework of this thesis. The implementation of the setup into the simulation is shown in Fig. 6.1. The full T-REX Coulomb excitation setup

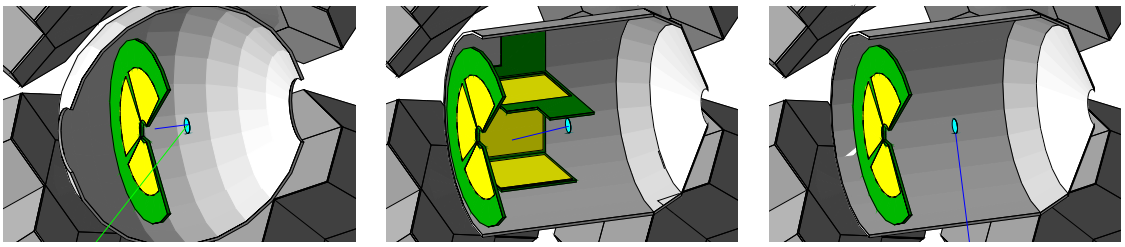

(a) (b) (c)

Figure 6.1: a) normal Coulomb excitation setup used until 2010. b) T-REX barrel setup for Coulomb excitation. c) Only CD detector with variable distance to the target.

consist of a forward barrel with 500μm thick position sensitive Silicon strip detectors and the standard forward CD detector. It covers angles from ϑ_{lab}= 7° to 78°. The other option is to remove the barrel detectors in the top an bottom position and move the CD detector closer to the target. Depending on the kinematics the high rates from elastic scattering may overload the detectors. In that case the barrel detectors have to be removed completely.

Depending on the aim of the experiment, different optimal geometries have to be chosen. For experiments with high rates, the angular coverage of the detectors can be shifted to the minimum in cross section of both elastic scattered ejectiles and recoils. However, if the rate of incoming beam particles is low, the amount of detected Coulomb excitation events should be maximized with the full coverage of the barrel and CD detector. In the framework of this thesis a program was developed in order to find the optimized setup for each reaction. For each detector geometry setting the detection rate of Coulomb excitation and elastic scattering events is calculated. This allows to find the setup geometry where the ratio of detected Coulomb excitation to elastic scattering events is maximized. Fig. 6.2 shows the result for the reaction of ^{30}Na on a ^{104}Pd target. A rate optimized setup for this reaction would be to position the CD

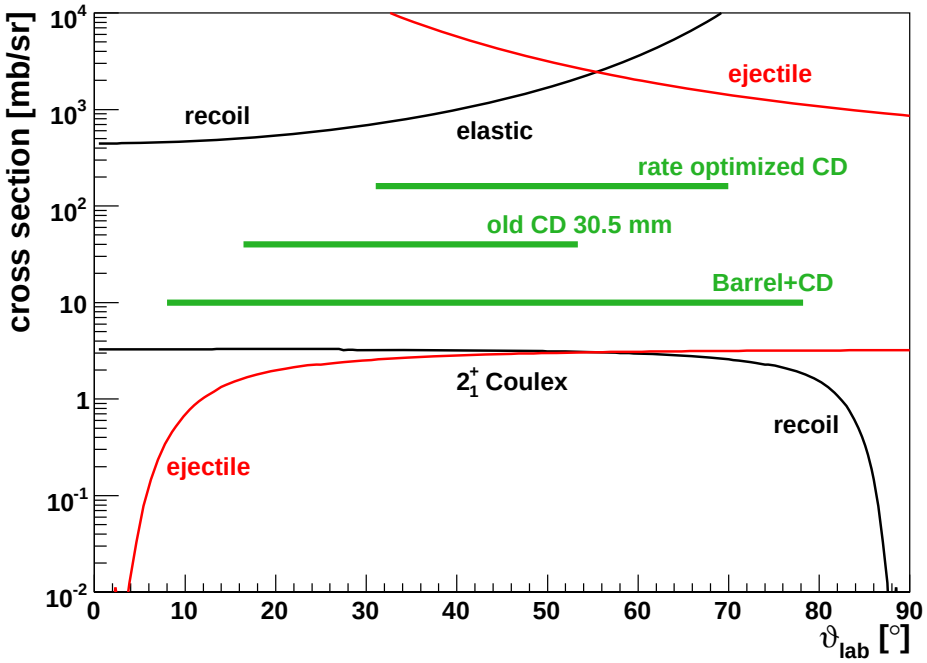

Figure 6.2: Cross sections for elastic scattering and Coulomb excitation for the ^{30}Na on ^{104}Pd reaction. The black (red) lines show the angular distribution of Rutherford scattering and Coulomb excitation for the recoil (ejectile) in the laboratory frame. The green bars show the angular coverage of T-REX and CD detector for this reaction.

detector at 20 mm distance from the target or using just the barrel detectors at 30 mm. In this setting the amount of elastic scattering events detected is minimized.

In order to measure the quadrupole moment of an excited state, large center of mass angles have to measured. This again highlights an advantage of the T-REX setup as it covers a larger ϑ_{lab} range. Also if both particles are detected in coincidence ambiguities in the particle identification can be reduced. By analyzing ejectile and recoil detection separately systematic errors can be eliminated.

A GEANT4 [AGO03] simulation has been developed to study the different variations of the setup and find the optimized geometry for each experiment. The event generator for Coulomb excitation generates projectile and ejectile of the reaction and, in case an excited state is populated, a γ-ray. The input needed is a CLX [BOE66] calculation of the differential cross section for each excited state. The analysis is based on the analysis for transfer reactions developed in this thesis. The same methods as described in chapter 4 are used to gate on γ - particle coincidences and to get the angular distributions of ejectiles and recoils. Although the γ-ray detection efficiency is slightly lower with the new setup ($\varepsilon_{\mathrm{ph}}$ is reduced by ca. 15 % due to the thicker walls of the target chamber and the larger distance of the MINIBALL detector to the target) the detection efficiency for particle - γ coincidences can be significantly increased. The advantages of using the T-REX setup instead of the CD detector with a fixed target distance has been demonstrated in three examples.

With the future HIE-ISOLDE facility beam energies up to 10 MeV/u are available for experiments. With higher beam energies it becomes possible to excite off-yrast states by using for example a ^{12}C target [COQ09]. In these inverse kinematics reactions only the recoil is detected since the scattering angles of the ejectile is below 7°. For the example reaction of ^{88}Kr 50 % more γ - particle coincidences than with the old setup can be expected by using the T-REX setup.

The ^{30}Na on ^{104}Pd reaction was already shown in Fig. 6.2. In this experiment the beam intensity was only 600 ^{30}Na/s. With such a low rate the full T-REX can be used. Comparing both setups, the gain in particle - γ coincidences is about 30 %.

For the last example a stable ^{84}Kr beam on a ^{120}Sn target was chosen. This is planned as a test experiment at the end of the 2010 experimental campaign. The reaction kinematics is very similar to experiments with Zn isotopes [WAL06]. With this simulation study the sensitivity to the quadrupole moment of the 2^+ state is investigated. The sign of the quadrupole moment indicates whether a nucleus is oblate ($Q < 0$) or prolate ($Q > 0$) deformed. Such studies of the deformation are important for the investigation of shape coexistence for example in the proton rich Kr isotopes [NAR07]. Therefore CLX calculations for a deformation $\beta = 0.3$ and different signs for the quadrupole moment Q of the 2^+ state in ^{84}Kr have been performed. The result of the simulation and analysis is shown in Fig. 6.3. The error bars for the T-REX setup are about a factor of 2 smaller and thus the setup has a significantly higher sensitivity for the measurement of the intrinsic quadrupole moment.

The new setup for Coulomb excitation is much more flexible and it can be optimized for the requirements of each experiment. As a consequence the MINIBALL steering

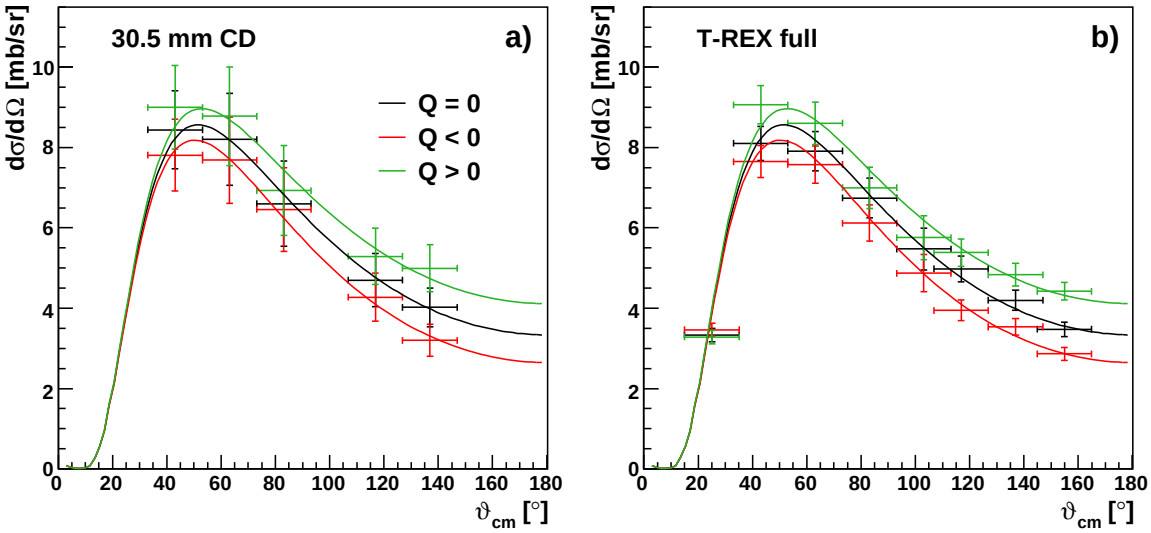

Figure 6.3: Dependance of the cross section with the quadrupole moment. a) old Coulomb excitation setup. b) T-REX setup. The cross section has been determined by a combination of the analysis of detected recoils and ejectiles.

committee has decided that, after a stable beam test in fall 2010, T-REX will be the standard Coulomb excitation setup for the experimental campaign in 2011.

6.2 Measuring the E0 decay in ^{32}Mg

In this section the possibilities to measure the E0 decay of the excited 0^+ state in ^{32}Mg are investigated. A measurement of the electric monopole strength ρ^2(E0) would allow to extract the mixing amplitude between the excited 0^+ state and the ground state. The excited 0^+ state in ^{32}Mg is apparently not populated in β decay, thus an experiment similar to the measurement of the E0 decay in ^{30}Mg [SCH09] is not possible. The method investigated here is to populate the 0^+_2 state by the two neutron transfer reaction and then stop the ^{32}Mg residues to measure the conversion electron decay with a Miniorange spectrometer. Fig. 6.4 shows a sketch of the setup combining the T-REX setup with a Miniorange spectrometer.

Two problems arise. First of all, during the IS470 experiment only about 900 protons have been identified in forward direction. However, protons from the reaction populating the excited 0^+ state in ^{32}Mg could only be identified between 27° and 55° in the laboratory frame. At larger angles the energy of the protons is not sufficient to punch trough the ΔE detector. With higher beam energy the proton energy also increases and with the maximum beam energy available at REX-ISOLDE the protons can be identified over the whole range in forward direction. By increasing the beam energy the number of identified protons can be doubled compared to the IS470 experiment and it also allows to detect more protons in backward direction. All together more

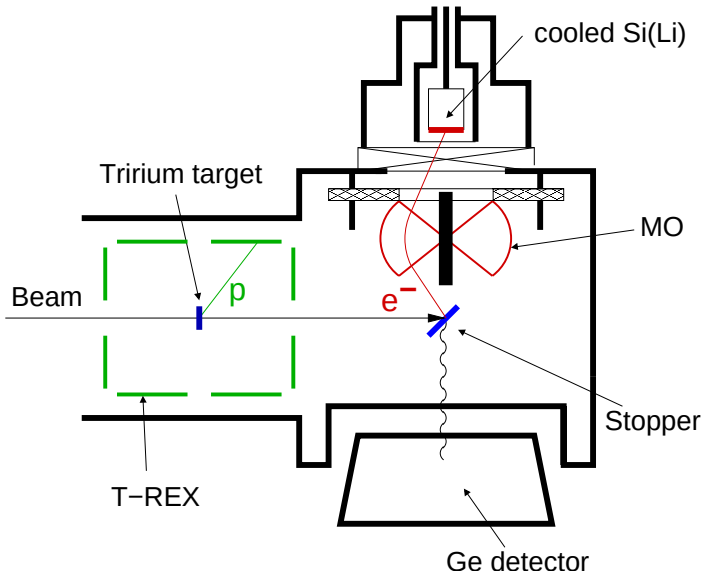

Figure 6.4: Sketch of the setup for a conversion electron measurement in ^{32}Mg. ^{32}Mg is populated by the two neutron transfer reaction, the protons from the (t,p) reaction are identified with the T-REX setup (green). Then the beam is stopped and the decay of the 0_2^+ state is measured with a Miniorange spectrometer (red) and a highly efficient γ detector such as a MINIBALL cluster.

than 10 protons/h from the excited 0^+ state can be expected assuming the same beam current as during the IS470 experiment ($\approx 4 \cdot 10^4$ pps, 150 h of beam = 19 shifts). With higher beam energies the fusion reaction channel opens (see section 3.6) and evaporation protons increase the background. The total fusion cross section for this reaction is 1 b (Fig. 3.7) and on average 0.4 protons are emitted per fusion reaction. Fig. 6.5 shows the laboratory distributions of protons from the fusion reaction. The total rate of fusion protons is 1000/h, which is about 100 fusion protons per transfer proton. However, when a cut on the excitation energy reconstructed from the proton energy is applied, as indicated in Fig. 6.5, only 7% of the fusion protons remain. Especially in backward direction the background from fusion is small, since only 0.5% of the fusion protons have energies below 2 MeV. Within this cut we expect 70 counts/h from fusion reactions and about 10 counts/h from transfer.

Another challenge arises when the beam is stopped in front of the Miniorange spectrometer. The β decay rate is on average $1 \cdot 10^5$ /s for the ^{30}Mg decay and the same for the daughter decay. Unlike in the case of ^{30}Mg where a coincidence with a β decay was required in order to clean the electron spectra, here this is not possible. Folding the β decay spectrum with the transmission function of the Miniorange spectrometer we expect a β electron rate in the Si(Li) detector of 2/ms. Assuming that all ^{32}Mg in the excited 0^+ state decay by E0 transition, we can expect 100 counts in 150h of beam time. The background from β decay will be about 20 counts/keV in the energy range

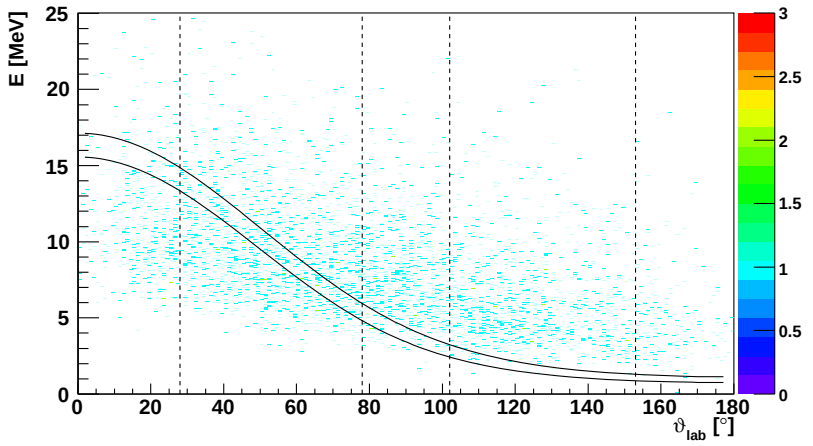

Figure 6.5: Distribution of protons emitted in the ^{30}Mg on ^{48}Ti fusion reaction at 2.85 MeV/u. Dashed lines indicate the solid angle covered by the barrel detector. The solid lines show kinematics calculation for the ^{30}Mg(t,p)^{32}Mg reaction with excitation energies of 500 and 1500 keV.

around the E0 peak if a coincidence window of a ms is applied between a proton from the transfer reaction and an electron detected in the Si(Li) detector. The resulting electron spectrum is shown in Fig. 6.6. Depending on the halflife of the 0^+ state the coincidence window can be smaller and the background further reduced. If in contrast

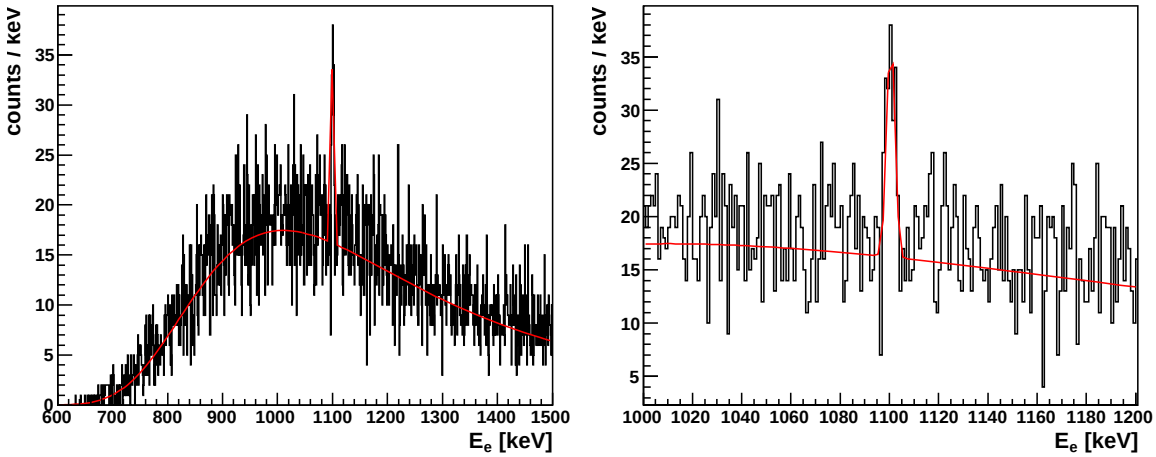

Figure 6.6: Simulated electron energy spectrum detected with the Miniorange. 100 counts in the E0 peak and a background rate of 2/ms is assumed.

the excited 0^+ state decays mostly by γ-ray emission to the 2^+ state at 886 keV, we expect about 40 counts in the γ-ray energy spectrum with a similar peak/background ratio ($\varepsilon_{\mathrm{ph}} \approx 2.5$ % at 100-200 keV with one MINIBALL triple cluster in very close

geometry). A very similar method has been successfully applied to measure the decay of the 13.3 μs isomeric state in ^{67}Ni populated in the ^{66}Ni(d,p) reaction [PAT08].

The success of such an experiment depends crucially on the lifetime of the excited 0^+ state. In order to extract the electric monopole strength ρ^2(E0), in addition to the ratio of E0 decays to E2 transitions, the lifetime has to be known. It is still under debate whether the lifetime of the 0_2^+ state can be measured in the same experiment by using fast γ-ray detectors or if a separate experiment has to be planned.

6.3 The onset of deformation and shape coexistence in ^{46}Ar

The successful t(^{30}Mg,p)^{32}Mg experiment reported on in this thesis opens the possibility for further (t,p) experiments at REX-ISOLDE using the T-REX setup. At the moment these studies are limited to lighter systems ($A \lesssim 50$ see section 2.5.2). The next (t,p) experiment planned at REX-ISOLDE is IS499 the t(^{44}Ar,p) two-neutron transfer reactions in inverse kinematics [WIM09]. The aim of this experiment is to identify and characterize excited states and to gain insights into the onset of deformation and the possible occurrence of shape-coexistence in this region where the $N = 28$ shell closure may be weakening.

The evolution of the $N = 28$ shell gap below ^{48}Ca has been the subject of a large number of theoretical and experimental studies (see Ref. [SOR08] for a recent review). Only four protons below $^{48}_{20}$Ca the $N = 28$ nucleus $^{44}_{16}$S exhibits a 2^+ energy and B(E2) value consistent with a configuration intermediate between spherical and deformed. This has been interpreted as a possible sign for the mixing of spherical and deformed shapes in $^{44}_{16}$S and preliminary evidence has been reported for a long lived 0^+ state in Ref. [GRÉ05]. For ^{42}Si some available experimental information indicates that this nucleus is well deformed.

The development of deformation in the $N = 28$ isotones has been attributed mostly to the disappearance of the spacing of the proton $d_{3/2}$ and $s_{1/2}$ single-particle levels as the neutron $f_{7/2}$ level is filled. Collectivity can easily arise from the long range quadrupole interaction between these orbitals. At the same time there are indications of a slight reduction of the $N = 28$ shell gap which would provide additional incentives for deformation.

In the neutron-rich Ar isotopes the single-particle structure of ^{45}Ar was investigated at GANIL using the ^{44}Ar(d,p) reaction [GAU08]. A significant fragmentation of spectroscopic strength was observed for the low-lying states which are attributed to core excitations of $1p-2h$ nature, as compared to the $0p-1h$ structure of the closed shell configuration. Excited states in ^{46}Ar were observed in intermediate energy Coulomb excitation [SCH96], secondary fragmentation [DOM03], and inelastic proton scattering [RIL05] but only the first excited 2^+ state has been firmly established. The most neutron-rich Ar isotopes for which excited states have been observed are ^{47}Ar and ^{48}Ar, which were populated in deep inelastic collisions [BHA08]. While all spin as-

signments in ^{47,48}Ar are tentative, the comparison to shell model calculations suggests that particle-hole excitations across the $N = 28$ shell gap play a significant role for the excited states in all Ar isotopes near $N = 28$.

A recent lifetime measurement in ^{44,46}Ar using the RDDS plunger method [MEN08] came to the conclusion that there are indications of a $N = 28$ weakening. In addition, a most recent study of excited states in ^{44}Ar via low-energy Coulomb excitation at SPIRAL (GANIL) [ZIE09] found a negative value for the quadrupole moment of the first excited 2^+ state in this nucleus, thus suggesting a prolate deformation. The results were compared to shell-model and relativistic mean-field calculations and to both axial and triaxial configuration mixing calculations using the generator coordinate method with the Gogny D1S interaction. None of the models is able to fully reproduce energies as well as B(E2) values. More experimental information is clearly needed to understand the onset of deformation and the possible occurrence of shape coexistence in this region.

Therefore, it is important to help clarify the picture of the evolution of the $N = 28$ shell closure in neutron-rich nuclei. ^{46}Ar lies right between the doubly magic ^{48}Ca ($Z = 20$,$N = 28$) and ^{44}S with its deformed ground state. Thus the structure of ^{46}Ar holds important information on the evolution of the $N = 28$ shell gap and the competition between spherical (neutron $0p - 0h$) and deformed (interpreted as $2p - 2h$) structures leading to shape coexistence and possibly shape mixing [ROD02a, LAL99, CAU02]. However, the current experimental knowledge of ^{46}Ar is not sufficient to obtain a clear picture.

From the proposed experiment one hopes to gain a significant extension of the knowledge of energies and quantum numbers of excited states in ^{46}Ar as well as the nature of the excited 0^+ state. The information will be gained from the energies and angular distributions of the protons from the (t,p) reaction. The relative cross-sections for the population of states in ^{46}Ar will provide important insights into the structure of these states.

In previous experiments different excited states in ^{46}Ar were observed via gamma-ray spectroscopy using intermediate energy Coulomb excitation [SCH96], inelastic scattering [RIL05] and fragmentation [DOM03]. Spin assignments for most observed states are tentative and many assignments have been proposed on the basis of comparison to theoretical predictions. The level schemes (shown in Fig. 6.7) derived from the two experiments are very different. While in the fragmentation reaction [DOM03] two states between the 4^+ state at 3890 keV and the 2_1^+ state are observed, in the proton inelastic scattering experiment [RIL05] additional states are observed only above the 4^+ state, including a 3^- state.

Thus, the available information on the excited levels is still sparse and no consistent picture has emerged. The proposed transfer experiment will add important additional information on excited states in ^{46}Ar. The proposed (t,p) experiment on the one hand will establish if the observed state at 2.7 MeV has 0^+ character or if another state in this energy range is the expected second 0^+ state. The cross section for populating this state and the ground state will be compared to DWBA calculations with the code FRESCO using spectroscopic amplitudes predicted by shell model calculations. Thus

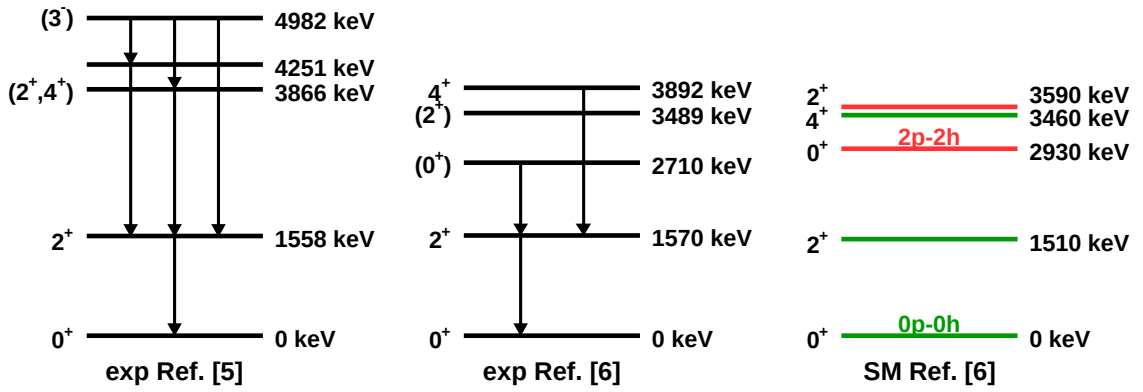

Figure 6.7: Level scheme of ^{46}Ar derived from inelastic proton scattering [RIL05] and fragmentation [DOM03] experiments in comparison with shell model calculations.

it will be possible to test if the excited 0^+ state has indeed a dominant neutron $2p-2h$ configuration, as suggested by the shell model calculations [DOM03] and the beyond mean-field calculations [ROD02a, LAL99].

In a simplified picture the ground state of ^{46}Ar is predicted to have a dominant $0p-0h$ configuration and thus can be approximately described by ^{44}Ar ground state plus 2 neutrons in the $f_{7/2}$ shell. A pure $2p-2h$ character of the 0^+ excited state means that this state can be approximately described by the ^{44}Ar ground state and 2 neutrons in the fp-shell above $N = 28$. Thus, the relative population of both states will be sensitive to the underlying structure of the 0^+ states and their possible mixing.

The highest production yields for ^{44}Ar are reported for a UC_x/graphite target coupled via a cold transfer line to a MK7 hot plasma ion source, with production yields of $\approx 3 \cdot 10^6$ atoms/μC. However, with the new VADIS ion source [PEN09, STO09] the yields for noble gases are by a factor of 3 higher. Due to the cooled transfer line the only atomic contaminations are higher charged nobles gases, $^{88}Kr^{++}$ and $^{132}Xe^{+++}$ which will be cleaned up in the REX-TRAP. There will however be a considerable amount of CO_2 from the ion source in the beam, which can overload the REX-TRAP. Depending on the actual yields for ^{44}Ar the beam could be continuously injected to the EBIS without cooling in the REX-TRAP. This would lower the total transmission efficiency to $\approx 2-3\%$ compared to the normal configuration with $\approx 5\%$ total efficiency. Alternatively the VADIS ion source could be operated at a lower temperature which significantly reduces the CO_2 content of the beam. The CO_2 molecule will be broken in the EBIS and does not contaminate the beam at MINIBALL. ^{22}Ne with the same A/q from the buffer gas can be avoided by using isotopically enriched ^{20}Ne as it was used for the ^{11}Be beam in IS430. Despite these disadvantages, a minimum beam intensity of 10^5 part/s at the T-REX setup can be expected.

For beam focusing a segmented diamond detector on the target ladder which can be moved to the target position and an active collimator with four PIN diodes in front of the chamber have been included.

In order to avoid fusion with the target carrier material Ti the beam energy has to be lowered to 2.16 MeV/u from the maximum REX-ISOLDE beam energy of 2.85 MeV/u.

DWBA calculations have been performed using the code FRESCO [THO88] using global optical model parameters extrapolated from stable nuclei [PER76], scaled to the lower beam energy. Due to the large positive Q-value for the (t,p) reaction to the ground state of ^{46}Ar of 4.7 MeV [AUD03], states at higher excitation energy are somewhat favored in the reaction and our experience from the t(^{40} Ar,p)^{42}Ar reaction shows that many states can be populated. For ^{46}Ar the energies of the known levels have been used as well as the suggested spin assignments (the level scheme is shown in Fig. 5 of Reference [DOM03]) to calculate the angular distributions of the emitted protons shown in Fig 6.8 a). Spectroscopic factors of one have been assumed for all transitions. This is a reasonable assumption (at least for the 0^+ states) from the experimental results of the t(^{30}Mg,p) and t(^{40}Ar,p) reactions. These distributions

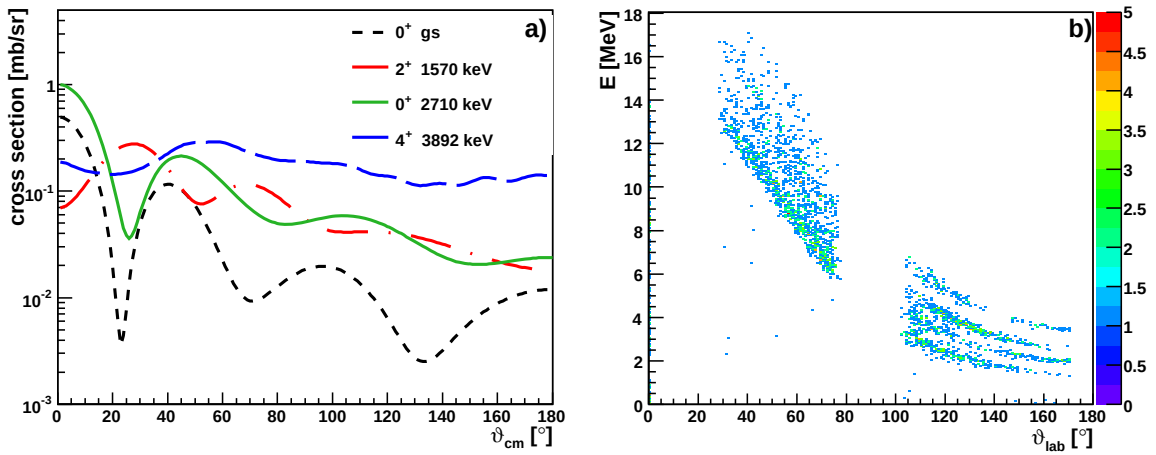

Figure 6.8: a) Angular distributions of protons emitted in the t(^{44}Ar,p)^{46}Ar reaction. b) Proton energy as a function of laboratory angle. The number of simulated events corresponds to the expected number of counts.

were used as input for GEANT4 [AGO03] simulations of the expected light charged particle emissions and the expected detector response of the T-REX set-up. Figure 6.8 b) shows the proton energies as a function of laboratory angle for the t(^{44}Ar,p)^{46}Ar reaction indicating that a clear separation of the known states is possible on the basis of the proton energies alone.

Protons from this reaction can be easily detected due to their high energy, which also enables their identification by $\Delta E - E$ separation in the Si-Telescopes of the T-REX set-up. The competing (t,d) reaction channel has a Q-value of -1.1 MeV and because of the negative Q-value and mass transfer from the target nuclei the deuterons will only

be observed in forward direction in the laboratory system. They can be distinguished from the protons by using the $\Delta E - E$ separation.

With the high Q-value of 4.7 MeV for the (t,p) reaction, the proton energy in backward direction is sufficient to punch through the ΔE-detector up to $\approx 130^\circ$ for low lying states. This allows for an additional suppression of the β electrons. Because of their high energy the protons in backward direction can be easily detected as compared to the IS470 experiment where part of the protons are below the detection threshold.

With the anticipated yields for the experiment (see below) it should be possible to uniquely identify the spins of the different states from their angular distributions.

The DWBA calculations for the t(^{44}Ar,p)^{46}Ar indicate comparable cross sections to the ones predicted for the t(^{30}Mg,p)^{32}Mg reaction, which were rather close to the observed ones.

Assuming a beam intensity on target of 10^5/s for ^{44}Ar and using the cross-section estimate from our DWBA calculations (using spectroscopic amplitudes of 1) together with the known efficiencies of the detection system one arrives at the rate estimates tabulated in Table 6.1. In addition, one can measure the (t,d) reaction products at the

Reaction	E_{state} [keV]	J^π	σ [mb]	counts/h
t(^{44}Ar,p)^{46}Ar	0	0^+	0.6	2.2
	1570	2^+	1.0	3.6
	2710	0^+	1.1	4.0
	3892	4^+	2.3	8.3
	total		5	18
t(^{44}Ar,d)^{45}Ar	0	$(7/2^-)$	72	260
	550	$(3/2^-)$	30	108
	1420	$(3/2^-)$	21	75
	total		123	443

Table 6.1: Expected count rates for the t(^{44}Ar,p)^{46}Ar and t(^{44}Ar,d)^{45}Ar reactions

same time and get additional information on the intermediate nucleus ^{45}Ar. The cross sections for this reaction are about 20-70 mb. So about 70 - 260 deuterons/h can be expected from the t(^{44}Ar,d)^{45}Ar reaction. This will allow to gate on γ-rays detected by the MINIBALL detector and further reduce the background. Due to the negative Q-value the deuterons will only be observed in forward direction in the laboratory frame and thus do not disturb the proton identification in backward direction.

The angular distributions for the (t,p) reaction were simulated with the statistics to be expected and compared to the ideal theoretical angular distributions. Fig. 6.9 shows the efficiency and solid angle corrected angular distribution as a function of laboratory angle for the t(^{44}Ar,p)^{46}Ar reaction corresponding to 10 days of beam time. For the analysis of the simulation shown in Fig. 6.8 the same method as for the t(^{30}Mg,p)^{32}Mg reaction has been applied. It can be seen that the different angular momentum transfer ΔL can be clearly identified by their shape.

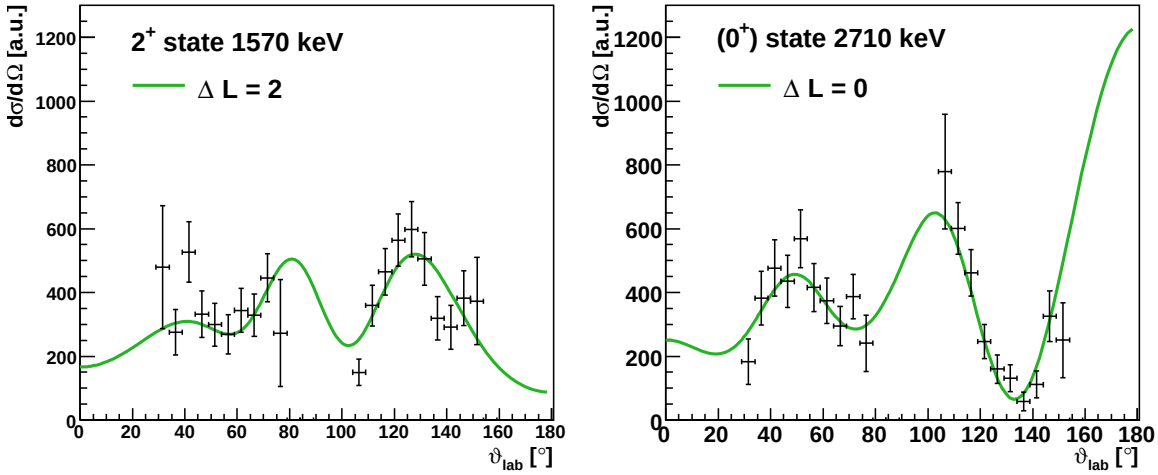

Figure 6.9: Efficiency and solid angle corrected angular distribution for the simulation shown in Fig. 6.8. The same analysis as for the t(^{30}Mg,p)^{32}Mg reaction reaction described in Chapter 4 has been performed.

The experimental proposal has been accepted by the ISOLDE and Neutron Time-of-Flight Experiments Committee meeting in March 2010, and will be performed in October 2010.

7 Summary and Outlook

In this thesis the "Island of Inversion" nucleus ^{32}Mg was studied by a two neutron transfer reaction at REX-ISOLDE. This inverse kinematics (t,p) experiment involved for the first time the use of a radioactive tritium target in combination with a radioactive heavy ion beam. The light recoil ions of the reaction were detected and identified with the T-REX charged particle detector array. γ-rays from excited states were detected in coincidence with protons with the MINIBALL Germanium detector array. Two states were observed in ^{32}Mg, the ground state and an excited state at 1058 keV. The measured angular distributions clearly identify the observed states as 0^+ and the low γ-ray yield observed from the excited state suggests a long lifetime of more than 10 ns. This is the first observation of the spherical shape coexisting excited 0^+ state in ^{32}Mg at 1058 keV. The measured cross section for the excited 0^+ state can be described by DWBA calculations using spectroscopic amplitudes based on almost pure *sd* configurations with a small addition of $(p_{3/2})^2$ contributions. The current data also confirm previous evidence that MCSM calculations with the SDPF-M effective interaction underestimate the $\nu p_{3/2}$ component in the ^{32}Mg ground state.

It would be very interesting to measure the lifetime of the excited 0^+ state as well as the electric monopole strength ρ^2(E0) in order to determine the shape mixing properties. Within the framework of this thesis the possibility to study the decay of the excited 0^+ state after population by the two neutron transfer reaction has been investigated. However, due to the low expected count rate, such an experiment is only feasible with a significant increase in beam intensity.

In the future a modified T-REX setup will be used for Coulomb excitation experiments at REX-ISOLDE. This setup is much more flexible than the previously used CD detector and it can be optimized for the requirements of each experiment. With the increased particle detection efficiency the T-REX setup has a significantly higher sensitivity for the measurement of the intrinsic quadrupole moment.

The successful demonstration of the feasibility to perform two neutron transfer reactions at REX-ISOLDE opens a broad range of future physics experiments. Shape coexistence is present in many parts of the nuclear chart. The triple coexistence of 0^+ states with different deformations in the proton rich Pb isotopes is not yet fully understood. Beams of Pb, Po and Hg have already been produced at REX-ISOLDE, and transfer reaction can be a complementary tool to decay spectroscopy and Coulomb excitation. In the region below ^{48}Ca the $N = 28$ shell closure may be weakening and deformation and shape coexistence arise. The aim of the next two neutron transfer experiment at REX-ISOLDE is to study the structure of ^{46}Ar by the t(^{44}Ar,p) reaction.

Furthermore, two nucleon transfer reactions are a valuable tool to probe features like pairing. The pairing interaction in heavy nuclei induces a phase transition to a superfluid state for nucleons in open shells and an enhanced pair transfer is expected [OER01]. The experimental observable is the enhancement factor EF. This measures the ratio of the two neutron transfer cross section to the expectation from a pure independent sequential transfer process. Two nucleon transfer reactions can thus probe shell closures as well as changes in the pairing correlations which are expected for very neutron rich nuclei.

As it was shown in section 2.5.2 transfer reactions will profit from higher beam energies which will be available with the upgrade of the REX-ISOLDE accelerator within the HIE-ISOLDE project or at other facilities like SPIRAL2 at GANIL or the reaccelerator project ReA at MSU.

Bibliography

[AGO03] S. Agostinelli, J. Allison, K. Amako et al., *Nucl. Inst. and Meth. A* **506** (2003) 250.

[AME05] F. Ames, J. Cederkäll, T. Sieber and F. Wenander, *The REX-ISOLDE Facility: Design and Commissioning Report* (CERN, Geneva, 2005).

[AUD03] G. Audi, A. H. Wapstra and C. Thibault, **729** (2003) 337.

[BEC69] F. D. Becchetti and G. W. Greenlees, *Phys. Rev.* **182** (1969) 1190.

[BER84] J. Berger, M. Girod and D. Gogny, *Nucl. Phys. A* **428** (1984) 23c.

[BHA08] S. Bhattacharyya, M. Rejmund, A. Navin et al., *Phys. Rev. Lett.* **101** (2008) 032501.

[BIL07] V. Bildstein, R. Gernhäuser, T. Kröll, R. Krücken, R. Raabe, P. V. Duppen and REX-ISOLDE and MINIBALL Collaborations, *Prog. Part. Nucl. Phys.* **59** (2007) 386.

[BIL10] V. Bildstein, Dissertation, Technische Universität München (expected 2010).

[BOE66] J. de Boer, In: *Coulomb excitation* (K. Alder and A. Winther, eds.) (Academic Press, 1966).

[BOI09] H. Boie, Dissertation, Universität Heidelberg (2009).

[BOY70] J. Boyno, T. Elze and J. Huizenga, *Nucl. Phys. A* **157** (1970) 263.

[BRI63] G. A. Brinkman, A. H. W. Aten and J. T. Veenboer, *International Journal of Applied Radiation and Isotopes* **14** (1963) 153.

[BRO04] B. A. Brown, A. Etchegoyen, N. S. Godwin, W. D. M. Rae et al., *MSU-NSCL report* **1289** (2004).

[CAU01] E. Caurier, F. Nowacki and A. Poves, *Nucl. Phys. A* **693** (2001) 374.

[CAU02] E. Caurier, F. Nowacki and A. Poves, *Eur. Phys. J. A* **15** (2002) 145.

[CHA69] B. Chambon, D. Drain, M. Yaker et al., *Nucl. Phys. A* **136** (1969) 311.

[CHR74] J. E. Christiansson, J. Dubois, H. Odelius and H. Roth, *Phys. Scr.* **10** (1974) 65.

[COQ09] L. Coquard, N. Pietralla, T. Ahn et al., *Phys. Rev. C* **80** (2009) 061304.

[DAE80] W. W. Daehnick, J. D. Childs and Z. Vrcelj, *Phys. Rev. C* **21** (1980) 2253.

[DÉT79] C. Détraz, D. Guillemaud, G. Huber et al., *Phys. Rev. C* **19** (1979) 164.

[DOB94] J. Dobaczewski, I. Hamamoto, W. Nazarewicz and J. A. Sheikh, *Phys. Rev. Lett.* **72** (1994) 981.

[DOM03] Z. Dombrádi, D. Sohler, O. Sorlin et al., *Nucl. Phys. A* **727** (2003) 195.

[EBE01] J. Eberth, G. Pascovici, H. G. Thomas, N. Warr et al., *Prog. Part. Nucl. Phys.* **46** (2001) 389.

[ENS07] ENSDF, *Evaluated Nuclear Structure Data File* (2007). `http://www.nndc.bnl.gov/ensdf/`.

[ERN84] H. Ernst and K. Lesko, *IRMA code* (1984).

[FED00] V. Fedoseyev, G. Huber, U. Köster et al., *Hyperfine Interactions* **127** (2000) 409.

[GAU08] L. Gaudefroy, O. Sorlin, F. Nowacki and D. Beaumel, *Phys. Rev. C* **78** (2008) 034307.

[GAV80] A. Gavron, *Phys. Rev. C* **21** (1980) 230.

[GRÉ05] S. Grévy et al., *Eur. Phys. J. A* **25** (2005) 111.

[GUI84] D. Guillemaud-Mueller, C. Détraz, M. Langevin, F. Naulin, M. de Saint-Simon, C. Thibault and F. Touchard, *Nucl. Phys. A* **426** (1984) 37.

[HAB00] D. Habs, O. Kester, T. Sieber et al., *Hyperfine Interactions* **129** (2000) 43.

[HER84] M. W. Herzog and R. J. Liotta, *Physica Scipta* **30** (1984) 52.

[HEY91] K. Heyde and J. L. Wood, *Journal of Physics G: Nucl. Part. Phys.* **17** (1991) 135.

[HIN10a] N. Hinohara, private communication (2010).

[HIN10b] N. Hinohara, K. Sato, T. Nakatsukasa et al., submitted to Phys. Rev. C (2010).

[HOF08] C. R. Hoffman, T. Baumann, D. Bazin et al., *Phys. Rev. Lett.* **100** (2008) 152502.

[HOW70] A. J. Howard, J. G. Pronko and C. A. Whitten, *Nucl. Phys. A* **152** (1970) 317.

[KAN09] R. Kanungo, C. Nociforo, A. Prochazka et al., *Phys. Rev. Lett.* **102** (2009) 152501.

[KAN10] R. Kanungo, C. Nociforo, A. Prochazka et al., *Phys. Lett. B* **685** (2010) 253.

[KIB08] T. Kibédi, T. Burrows, M. Trzhaskovskaya, P. Davidson and C. N. Jr., *Nucl. Inst. and Meth. A* **589** (2008) 202.

[KIM03] I. J. Kim, C. S. Park and H. D. Choi, *Applied Radiation and Isotopes* **58** (2003) 227.

[KÖS00] U. Köster, V. N. Fedoseyevc, V. I. Mishinc, L. Weissman et al., *Nucl. Inst. and Meth. B* **160** (2000) 528.

[KÖS03] U. Köster, V. Fedoseyev, A. Andreyev, U. Bergmann et al., *Nucl. Inst. and Meth. B* **204** (2003) 347.

[KRÖ08] T. Kröll, K. Wimmer, R. Krücken, V. Bildstein et al., *Proposal to the INTC Committee: Shape coexistence in the "island of inversion": Search for the* 0_2^+ *state in* ^{32}*Mg applying a two-neutron transfer reaction* (2008).

[LAL99] G. Lalasissis, D. Vretenar, P. Ring, M. Stoitsov and L. Robledo, *Phys. Rev. C* **60** (1999) 014310.

[LET97] J. Lettry, R. Catherall, P. Drumm, P. V. Duppen et al., *Nucl. Inst. and Meth. B* **126** (1997) 130.

[LUN06] D. Lunney, G. Audi, C. Gaulard et al., *Eur. Phys. J. A* **28** (2006) 129.

[LUT67] H. F. Lutz, J. J. Wesolowski, L. F. Hansen and S. F. Eccles, *Nucl. Phys. A* **9** (1967) 591.

[LUT03] R. Lutter, O. Schaile et al., *MARaBOU Data Acquisition* (2003). `http://www.bl.physik.uni-muenchen.de/marabou/html/`.

[LUT05] R. Lutter, *MED data structure.* `http://www.bl.physik.uni-muenchen.de/marabou/html/doc/MedStructure.pdf` (2005).

[MAC05] H. Mach, L. M. Fraile, O. Tengblad et al., *Eur. Phys. J. A* **25** (2005) s01 105.

[MAH08] M. Mahgoub, Dissertation, Technische Universität München (2008).

[MAR05] F. Maréchal, D. L. Balabanski, D. Borremans, J.-M. Daugas et al., *Phys. Rev. C* **72** (2005) 044314.

[MAT07] C. M. Mattoon, F. Sarazin, G. Hackman et al., *Phys. Rev. C* **75** (2007) 017302.

[MEN08] D. Mengoni, J. J. Valiente-Dobón, A. Gadea et al., *Acta. Phys. Pol. B* **40** (2008) 485.

[MIL09] D. Miller, P. Adrich, B. A. Brown, V. Moeller et al., *Phys. Rev. C* **79** (2009) 054306.

[MIS93] V. Mishin, V. Fedoseyev, H.-J. Kluge, V. Letokhov et al., *Nucl. Inst. and Meth. B* **73** (1993) 550.

[MOT95] T. Motobayashi, Y. Ikeda, K. Ieki, M. Inoue, N. Iwasa et al., *Phys. Lett. B* **346** (1995) 9.

[NAN69] H. Nann, R. Bass, K. O. Groeneveld and F. Saleh-Bass, *Z. Physik* **218** (1969) 190.

[NAR07] B. S. Nara Singh, D. G. Jenkins, C. J. Barton et al., *Proposal to the INTC Committee: Shape determination in Coulomb excitation of* ^{72}Kr (2007).

[NEY05] G. Neyens, M. Kowalska, D. Yordanow, K. Blaum et al., *Phys. Rev. Lett.* **94** (2005) 022501.

[NIE05a] O. Niedermaier, Dissertation, Universität Heidelberg (2005).

[NIE05b] O. Niedermaier, H. Scheit, V. Bildstein, H. Boie et al., *Phys. Rev. Lett.* **94** (2005) 172501.

[OER01] W. von Oertzen and A. Vitturi, *Rep. Prog. Phys.* **64** (2001) 1247.

[OTS01a] T. Otsuka, R. Fujimoto, Y. Utsuno, B. A. Brown, M. Honma and T. Mizusaki, *Phys. Rev. Lett.* **87** (2001) 082502.

[OTS01b] T. Otsuka, M. Honma, T. Mizusaki, N. Shimizu and Y. Utsuno, *Prog. Part. Nucl. Phys.* **47** (2001) 319.

[OTS02] T. Otsuka, *Prog. Theo. Phys. Suppl.* **146** (2002) 6.

[OTS04] T. Otsuka, *Eur. Phys. J. A* **20** (2004) 69.

[OTS05] T. Otsuka, T. Suzuki, R. Fujimoto, H. Grawe and Y. Akaishi, *Phys. Rev. Lett.* **95** (2005) 232502.

[OTS10] T. Otsuka, T. Suzuki, M. Honma, Y. Utsuno et al., *Phys. Rev. Lett.* **104** (2010) 012501.

[OTT07] T. Otto, CERN Specification N° 4229RP20070405-GD-001, Official Memorandum to ISOLDE Physics Coordinator (2007).

[PAT08] N. Patronis, R. Raabe, N. Bree et al., *Proposal to the INTC Committee: One nucleon transfer reactions around* ^{68}Ni *at REX-ISOLDE* (2008).

[PEN09] L. Penescu et al., *International Conference on Ion Sources, Gatlinburg, Tennessee* (2009).

[PER76] C. M. Perey and F. G. Perey, *Atomic data and nuclear data tables* **17** (1976) 1.

[PRI99] B. V. Pritychenko, T. Glasmacher, P. D. Cottle et al., *Phys. Lett. B* **461** (1999) 322.

[PÜH77] F. Pühlhofer, *Nucl. Phys. A* **280** (1977) 267.

[RIL05] L. A. Riley, M. A. Abdelqader, D. Bazin et al., *Phys. Rev. C* **72** (2005) 024311.

[ROD02a] R. Rodríguez-Guzmán, J. Egido and L. Robledo, *Phys. Rev. C* **65** (2002) 024304.

[ROD02b] R. Rodríguez-Guzmán, J. L. Egido and L. M. Robledo, *Nucl. Phys. A* **709** (2002) 201.

[ROD07] T. Rodriguez and J. L. Egido, *Phys. Rev. Lett.* **99** (2007) 062501.

[ROD08] T. Rodriguez and J. L. Egido, private communication (2008).

[ROO07] ROOT, *An Object-Oriented Data Analysis Framework* (2007). `http://root.cern.ch/`.

[SCH67] J. P. Schiffer, G. C. Morrison, R. H. Siemssen and B. Zeidman, *Phys. Rev.* **164** (1967) 1274.

[SCH96] H. Scheit, T. Glasmacher, B. A. Brown et al., *Phys. Rev. Lett.* **77** (1996) 3967.

[SCH09] W. Schwerdtfeger, P. G. Thirolf, K. Wimmer et al., *Phys. Rev. Lett.* **103** (2009) 012501.

[SOR08] O. Sorlin and M. Porquet, *Prog. Part. Nucl. Phys.* **61** (2008) 602.

[STO09] T. Stora, private communication (2009).

[TER08] J. R. Terry, B. Brown, C. M. Campbell et al., *Phys. Rev. C* **77** (2008) 014316.

[THI75] C. Thibault, R. Klapisch, C. Rigaud, A. M. Poskanzer, R. Prieels, L. Lessard and W. Reisdorf, *Phys. Rev. C* **12** (1975) 644.

[THO88] I. J. Thompson, *Comp. Phys. Rep.* **7** (1988) 167.

[THO06] I. Thompson, *Fresco, Coupled Reaction Channels Calculations* (2006). `http://www.fresco.org.uk`.

[THO09] I. J. Thompson and F. M. Nunes, *Nuclear Reactions for Astrophysics* (Cambridge University Press, 2009).

[UDA73] T. Udagawa, H. H. Wolter and W. R. Coker, *Phys. Rev. Lett.* **31** (1973) 1507.

[UTS99] Y. Utsuno, T. Otsuka, T. Mizusaki and M. Honma, *Phys. Rev. C* **60** (1999) 054315.

[WAL06] J. van de Walle, Dissertation, Katholieke Universiteit Leuven (2006).

[WAL09] J. van de Walle, V. Bildstein, N. Bree et al., *Eur. Phys. J. A* **42** (2009) 401.

[WAR90] E. K. Warburton, J. A. Becker and B. A. Brown, *Phys. Rev. C* **41** (1990) 1147.

[WAR08] N. Warr, Miniball electronics May 2008 (2008). `http://www.ikp.uni-koeln.de/~warr/doc/electronics_May2008.pdf`.

[WEI06] W. Weinzierl, Diploma thesis, Technische Universität München (2006).

[WIL84] B. H. Wildenthal, *Prog. Part. Nucl. Phys.* **11** (1984) 5.

[WIM09] K. Wimmer, R. Krücken, V. Bildstein et al., *Proposal to the INTC Committee: Study of the onset of deformation and shape coexistence in ^{46}Ar via the inverse kinematics (t,p) reaction* (2009).

[ZIE09] M. Zielińska, A. Görgen, E. Clément et al., *Phys. Rev. C* **80** (2009) 014317.

Acknowledgement

It is a pleasure to thank all those people who helped and contributed in the completion of this thesis.

- First of all, I express my sincerest gratitude to Prof. Reiner Krücken for giving me the opportunity to work on this interesting project. I am very grateful for his enormous support and help throughout the work on this thesis.
- I want to thank Thorsten Kröll for his support in all stages of this work and for the encouraging discussions on and beyond physics.
- I am greatly indebted to Vinzenz Bildstein for the help with so many things during the experiment and the analysis.
- I would like to thank Roman "das muss so sein" Gernhäuser for his help with the setup and the understanding of detectors, electronics and data acquisition.
- This project would not have been possible without the extensive help of the (REX-)ISOLDE team, in particular I want to thank Thierry Stora, Didier Voulot and Fredrik Wenander for preparing the beam and for fruitful discussion about the feasibility of ^{44}Ar beams. The use of a radioactive tritium target was a challenge, I want to thank Alexandre Dorsival (CERN radiation protection) for his support and Daniel Carminati (ISOLDE mechanical workshop) for opening the target container.
- I want to thank Rudi Lutter for his huge support with the data acquisition. If he was not at CERN himself, Rudi provided telephone or email support even late in the evening or on the weekend.
- I want to give thanks to all members of the T-REX/IS470 collaboration for their help during the experiment and good discussions on the interpretation of the results.
- I wish to thank Antonio Moro and Filomena Nunes for fruitful discussions about the reaction theory and their help with numerous FRESCO problems.
- Many thanks go to my office mates Vinzenz Bildstein, Clemens Herlitzius, Anuj Parikh, Konrad Steiger and Katrin Straub for moral support, countless coffee breaks and for having a beer or two.
- Finally, I want to thank my family and friends for their support, encouragement and friendship.